The University Of Sheffield.

Mechanistic studies of bacterial chromosome segregation using single-molecule microscopy

Adam Cyrus Brooks

A thesis submitted in partial fulfilment of the requirements for the degree of Doctor of Philosophy

The University of Sheffield

Faculty of Science

Department of Molecular Biology and Biotechnology

September 2020

Abstract

In all forms of life, DNA must be properly segregated to each daughter cell prior to cell division to ensure genetic material is inherited. Prokaryotes encode their own systems which facilitate the process of segregation of low-copy number plasmids and chromosomes, including active partitioning (Par) systems. Recent studies have used fluorescence microscopy to reveal the highly organised structure of bacterial chromosomes and their distinct localisation patterns which occur within the cell.

The aim of this project was to gain new insight into the molecular mechanisms of chromosome partition systems. A bespoke TIRF microscope was used to study the interplay between the partition proteins of *V. cholerae* Chromosome II. The non-specific interaction between ParA and DNA was characterised, furthering our understanding of the role of the nucleoid during the segregation process. The partitioning system of *V. cholerae* Chromosome II was reconstituted *in vitro* and revealed the formation of chromosomal ParA depletion zones, akin to those seen during the reconstitutions of plasmid partition systems. The TIRF microscope was also adapted to allow the detection of freely diffusing single molecules using a sCMOS detector to multiplex detection channels.

Acknowledgements

I would like to thank the Biotechnology and Biological Sciences Research Council (BBSRC) for funding this project.

Thank you to Prof. Mark Leake and Dr Tim Craggs for agreeing to examine this thesis. A special thanks is also extended to Prof. Jeff Green for agreeing to moderate the examination.

The completion of this thesis was made possible with the support of my supervisor, Dr Stéphane Mesnage, who went above and beyond in helping me during a challenging time. If it were not for his advice and encouragement over the past year, I would not have the closure I needed from this chapter of my life, so I am deeply grateful to him.

I would also like to thank my advisor, Dr Egbert Hoiczyk, for his enjoyable conversation throughout my PhD, in addition to the feedback he provided on my project and thesis. Thank you to Prof. Jeff Green and his lab for the weekly meetings. I enjoyed partaking in the scientific discussions (and baking) which arose from them. Thank you to Dr Ling Chin Hwang for their reading and advice on my thesis. Thank you to Dr Ash Cadby for their advice.

Thank you to my fellow lab members, Sat and Alex. Working with both of you over the past few years was a real pleasure and a privilege. I also extend my thanks to the project students: Ruth, Matt, and Jack. They helped me discover the value of mentoring others and made for some of the best days of my PhD.

A special thanks goes to my friends: Rob, Laurence, Luz, Joe, Sophie, and everyone else who made lunchtime at Firth Court my favourite part of the day. Working on my own in a dark microscopy lab could get quite lonely, so their company and conversation went a long way in keeping my sanity.

To my family, thank you for all the love and support you have provided me. It has been 8 years since I arrived at Sheffield University, and they have showed unwavering support throughout.

Lastly, to my girlfriend Sophie: Thank you for everything you have done to support me over the last 4 years and for bringing me back from the brink all too often. You have shown more patience and understanding than anyone over this PhD, and I have only made it this far because of your support.

Table of Contents

List of Figures

List of Abbreviations

aa	Amino acid
ADP	Adenosine diphosphate
ATP	Adenosine triphosphate
BME	2-Mercaptoethanol
bp	Base pair
BSA	Bovine serum albumin
cAMP	Cyclic adenosine monophosphate
CFE	Cell free extract
ChIP	Chromatin immunoprecipitation
Chr1	Chromosome I
Chr2	Chromosome II
crtS	Chr2 replication triggering site
CT	Cholera toxin
CTP	Cytidine triphosphate
dCTP	Deoxycytidine triphosphate
DNA	Deoxyribonucleic acid
DOPC	1,2-dioleoyl-sn-glycero-3-phosphocholine
DTT	Dithiothreitol
EDTA	Ethylenediaminetetraacetic acid
EMCCD	Electron-multiplying charge-coupled device
GFP	Green fluorescent protein
GTP	Guanosine-5'-triphosphate
HDRs	High density regions
HTH	Helix-turn-helix
kb	Kilobase
MFM	Multifocus microscopy
NA	Numerical aperture
nsDNA	Non-specific DNA
Pad	Phenolic acid decarboxylase
PALM	Photo-activated localization microscopy
Par	Partitioning
PCR	Polymerase chain reaction
Pop	Polar organising protein
sCMOS	Scientific complementary metal–oxide–semiconductor
Scp	Segregation and condensation protein
SIM	Structured illumination microscopy
SMC	Structural maintenance of chromosomes
smFRET	Single molecule fluorescence resonance energy transfer
SBR	Signal-to-noise ratio
Sop	Stability of plasmid
SUVs	Small unilamellar vesicles
TCP	Toxin-coregulated pilus
TdT	Terminal deoxynucleotidyl transferase
TIRFM	Total internal reflection fluorescence microscopy
Tris	Tris(hydroxymethyl)aminomethane

Chapter 1

Introduction

1.1 Random vs non-random segregation

The ability to pass genetic information to the next generation is key in all forms of life. The stable inheritance of DNA is governed by precise mechanisms which occur within cells. In eukaryotes, chromosomes replicates line up along a central axis and are pulled apart by spindle fibres. Upon cell division, each newly formed daughter cell possesses a full set of chromosomes, identical to the genome of its parent. In bacteria, the many mechanisms which guarantee maintenance of the genome are not fully understood. High-copy-number plasmids can rely on random distribution and segregation within the cell and still be faithfully inherited by both daughter cells upon division (**Figure 1**). DNA molecules with fewer copies, including low-copy number plasmids and chromosomes, however, require correct positioning throughout the volume of the cell prior to division to ensure stability (**Figure 2**).

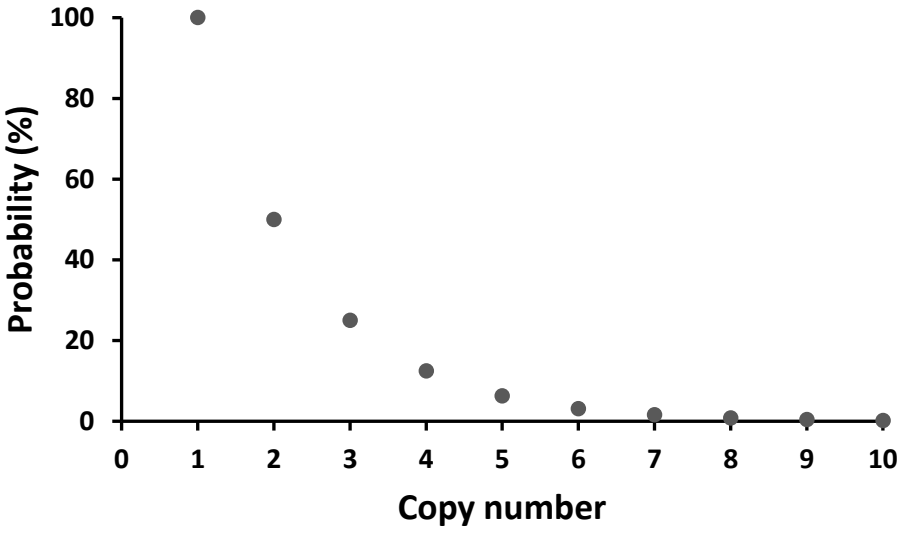

Figure 1. High copy number molecules are inherited through random segregation. *Probability that one of two daughter cells not receiving a replicate of a molecule based on totally random distribution and the copy number of a molecule. Probability of a daughter cell not inheriting a single molecule is less than 1% for molecules with copy numbers < 8.*

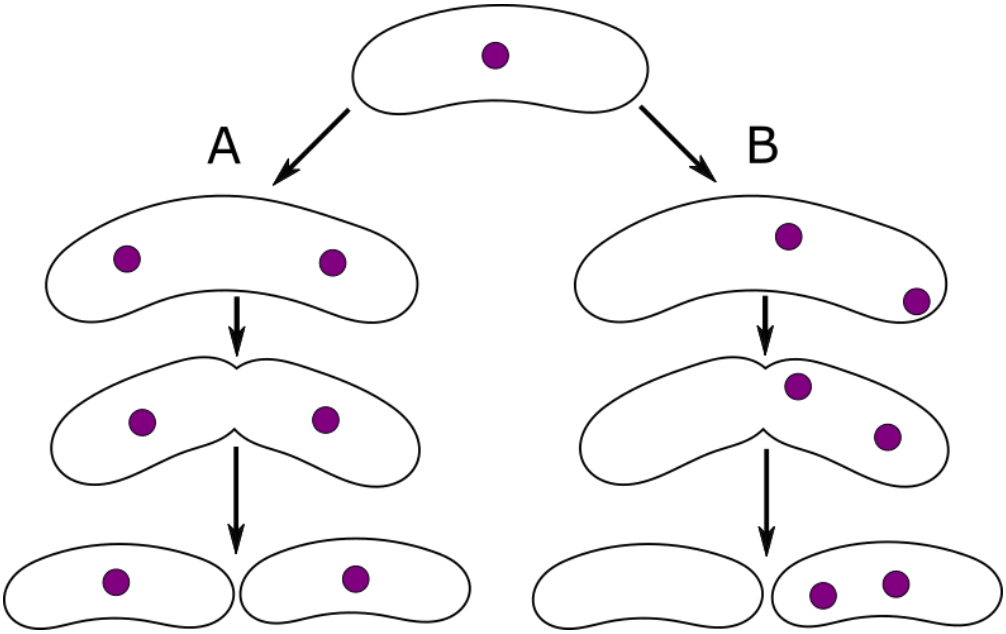

Figure 2. Difference between random and non-random segregation of low-copy number DNA molecules within bacteria. *(A) Proper distribution of DNA molecules through a non-random segregation mechanism means both daughter cells inherit a copy of the DNA molecule upon cell division. (B) Random movement of DNA molecules can cause an unequal split of copies across daughter cells.*

In this chapter, I introduce the general principles of how bacteria segregate and organise their chromosomes. I describe the partition (*par*) systems encoded on DNA molecules that help them self-organise within the cell volume and detail some of the studies which have revealed the different mechanisms through which they operate. Fluorescence imaging has been crucial to performing *in vitro* reconstitutions that have advanced our understanding of partition systems from low-copy number plasmids. For this reason, the latter part of this chapter focusses on some of the bioimaging and Fluorescence spectroscopy techniques that are routinely applied to better understand these systems.

1.2 Chromosome organisation in bacteria

Bacterial chromosomes were originally thought of as disorganised masses of DNA that fitted randomly into the cell, showing little to no meaningful localisation of genes. This has been disproven in recent years through numerous studies which describe the presence of systems which provide spatial organisation to the nucleoid and actively segregate chromosome sister copies from one another (Glaser et al. 1997; Gordon et al. 1997; Teleman et al. 1998). Most bacterial cells have a single circular chromosome which measures several mega bases long, which if stretched out would measure roughly 2 mm in length. Without any mechanisms to condense and organise this amount of DNA, it would be impossible for it to fit inside the tight confines of a typical 2 µm long bacterial cell (Trun and Marko 1998; Holmes and Cozzarelli 2000). What is more, imaging of live cells using fluorescence microscopy has revealed that the dynamics of chromosomes within bacterial cells are

orchestrated by multiple active mechanisms and result in the precise localisation of the origin and termination regions of the chromosome.

1.2.1 General dynamics of chromosome segregation in bacteria

For chromosomes in eukaryotic cells, the replication and segregation processes are part of distinct phases, separated by a temporary pause (Viollier et al. 2004). In bacteria, these processes occur simultaneously. Duplicated regions on sister chromosomes therefore segregate in the same order in which they are replicated, with the origin regions segregating first, followed by the bulk of the chromosome and ending with the duplicated terminus regions (Viollier et al. 2004; Nielsen et al. 2006; Lesterlin et al. 2012).

The exact spatial organisation of the chromosome determines the localisation of the replication origin and therefore where in the cell DNA replication and segregation initiates. In *E. coli* for example, the chromosome origin is positioned at mid cell prior to replication. Once replicated, the origin regions on the partially replicated chromosome pair proceed to increase the distance between themselves and translocate to the quarter cell positions (Nielsen et al. 2006). Upon cell division, both newly formed daughter cells inherit a single copy of the chromosome (**Figure 3a**). Conversely, chromosome dynamics in *Caulobacter crescentus* exhibit a very different segregation pattern. Here, the replication origin is positioned not at the midpoint of the cell but at one of the cell poles prior to replication. The segregation of the replicated origin regions on sister chromosomes occurs through transportation of one the origins to the opposite cell pole whilst the other remains stationary. Upon completing replication, the cell divides forming two daughter cells, each with their own chromosome (Viollier et al. 2004; Shebelut et al. 2010). The position of the chromosome within the new cell is the same as in the old cell, with the origin and terminus regions localised at the cell poles (**Figure 3b**).

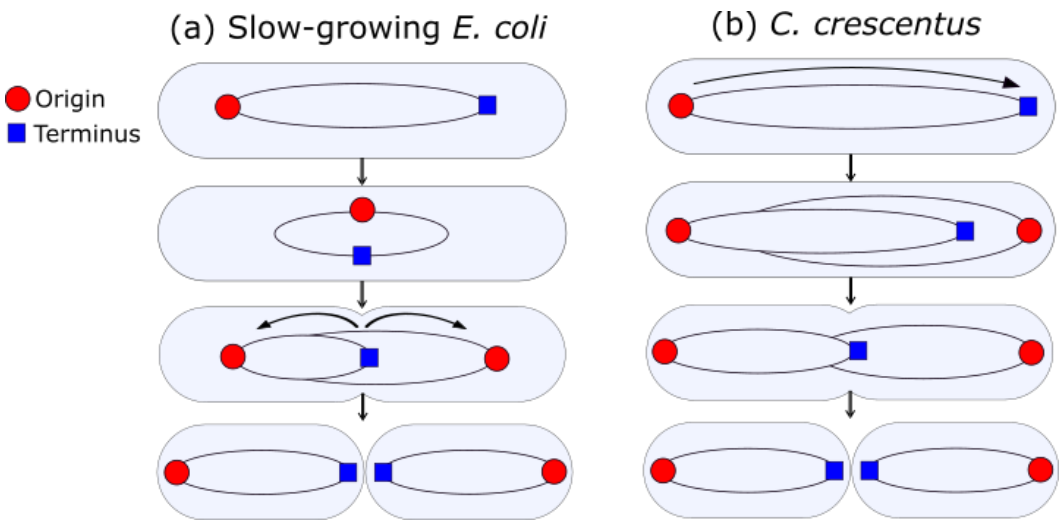

Figure 3. Differences in chromosome dynamics between different bacteria. (a) *In E. coli, the origin moves to the mid-cell position, at which point replication is initiated. The replicated origin regions move towards opposite cell poles, coming to rest at the quarter cell positions. Upon cell division, both new-born cells contain a copy of the chromosome.* ***(b)*** *In C. crescentus, replication is initiated whilst the origin is at the cell pole. The newly replicated origin then actively segregates towards the opposite cell pole. Replication of the chromosome proceeds and ends at cell division, resulting in two cells each with its own copy of the chromosome* (Gitai et al. 2005).

The segregation of the chromosome origin regions is of interest as it is a powerful determinant of the final spatial configuration of the chromosome. How bacteria segregate newly replicated origins of their chromosomes has been the subject of numerous investigations over the years. One of the first models which sought to explain the dynamics of chromosome origin segregation was the surface attachment model. This simple model assumes that chromosome replication initiates at the mid-cell position. The origin pair are attached to the membrane and are segregated by the cell growth that occurs between them (Jacob et al. 1963). It has since been discovered that cell growth is not limited to the mid-cell but occurs along the cell's entire length in many Gram-negative bacteria like *E. coli*. Origin segregation for many species has also been found to occur at a significantly faster rate than cell growth (Glaser et al. 1997; Webb et al. 1998; Gordon et al. 2004; Viollier et al. 2004). For these reasons, surface attachment to the cell envelope could not account for origin segregation. Low-copy number plasmids rely on a dedicated partitioning locus (*parABS)* to drive their spatial organisation within the cell. Therefore, the identification of *parABS* genes on chromosomes, closely related to those found on plasmids, is a good candidate for understanding how chromosomes actively segregate their origin regions.

1.3 Plasmid partition systems

Plasmid partition systems, also known as ParABS, were first discovered on low-copy number plasmids, and were revealed to be essential for the proper inheritance of plasmids (Austin and Abeles 1983a; Austin and Abeles 1983b; Abeles et al. 1985; Mori et al. 1986). ParABS systems consist

of three components: a *cis*-acting partitioning site (*parS*), a *trans*-acting partitioning site binding protein (ParB) and an ATPase (ParA). During DNA replication, ParB loads onto and around the *parS* site located near the origin of replication, forming a partition complex (Funnell 2016). This partition complex is actively segregated from a partition complex formed on the other sister DNA molecule (Erdmann et al. 1999). ParA ATPase proteins provide the driving force for the translocation of the partition complexes through the hydrolysis of bound adenosine triphosphate (ATP) molecules (Bouet and Funnell 1999).

ParABS systems are found on both bacterial chromosome and plasmid DNA. ParABS was originally identified on P1 plasmid from *Escherichia coli* (Austin et al. 1985). They have since been shown to be essential for the stability of numerous low-copy number plasmids and bacterial chromosomes. Indeed, introduction of *par* loci onto unstable plasmids has been shown to improve their maintenance within their host cell (Yamaichi and Niki 2000; Godfrin-Estevenon et al. 2002; Ebersbach et al. 2006). ParABS systems have also been found on over 65% of bacterial chromosomes, indicating that they may be key to chromosome segregation and prevention of the formation of anucleate cells in those species (Livny et al. 2007). Just as in plasmid homolog systems, chromosomes contain centromere-like *parS* DNA sequences (Mohl and Gober 1997; Lin and Grossman 1998; Kim et al. 2000; Mohl et al. 2001; Godfrin-Estevenon et al. 2002; Bartosik et al. 2004; Dubarry et al. 2006; Lee et al. 2006; Yamaichi, Fogel, McLeod, et al. 2007) and encode for ParA and ParB proteins. Using the site-specific binding protein Spo0J, a member of the ParB family of proteins, the location of a 16-bp site termed *spo0J* determined on the chromosome of *B. subtilis* (Lin and Grossman 1998). The presence of the *spo0J* site stabilised otherwise unstable plasmids, demonstrating that the *spo0J* site acts as an effective *parS* site. These *parS* sequences were subsequently found close to the origin of other bacterial chromosomes, including those of Burkholderia cenocepacia, Vibrio cholerae and Pseudomonas putida. The relative similarity between chromosomal *parS* sites allowed them to be identified by searching for inverted repeats which resemble the *parS* sequences found in *B. subtilis* (Godfrin-Estevenon et al. 2002; Dubarry et al. 2006; Saint-Dic et al. 2006). The location of *parS* near the chromosome origin makes them one of the first DNA regions to undergo replication. The proximity of *parS* to the origin suggests that their role is to drive or assist with the proper localisation and segregation of this region of the chromosome. Just as ParABS systems are essential to the maintenance of plasmids, their widespread conservation in chromosomes hints at their evolutionary importance in the inheritance of bacterial genomes in many bacteria.

1.3.1 Classes of plasmid partition systems

ParABS systems are broadly conserved across prokaryotes, and serve the important role of driving and optimising the segregation of their host molecules. However, how this is achieved and the mechanics involved can vary significantly. For this reason, ParABS systems have been subdivided into three distinct types, based primarily on the structure of the ATPase for which they encode. Identification of these subgroups was conceived largely from findings in plasmid segregation studies and so this section largely focusses on the mechanism of partition systems encoded on plasmids. Here, each subgroup is described along with how observations through microscopy and reconstitution have helped establish a mechanism for their involvement in segregation.

1.3.1.1 Type I

Partition systems which encode for an ATPase containing a Walker A motif (Walker P-loop) are classified as type I systems. Alongside the ATPase (ParA), these systems encode for a partition site binding protein (ParB) and a centromere-like partition site (*parS*). A significant feature of ParA proteins of Type I is their ability to bind to non-specific DNA, enabled by their Walker-box domains. However, ParA only binds DNA when in the presence of ATP, which allows it to enter the appropriate conformational state for DNA binding. In the absence of any nucleotide, ParA proteins are monomeric. ParA must bind to ATP to allow it to oligomerise into a dimer (Davey and Funnell 1994). Two ParA molecules flank an ATP molecule to create a dimer, termed a nucleotide sandwich. The ParA-ATP dimer then undergoes a conformational change to a ParA-ATP* state, which allows it to bind DNA (Vecchiarelli et al. 2010). Although previous investigations had revealed ParA to be essential for the successful segregation of low-copy number plasmids *in vivo*, little was known about the mechanism that allows it to drive segregation of large DNA molecules. Studies had confirmed that ParB and DNA is able to stimulate the ATPase activity of ParA, but how this generated the force for plasmid segregation was still not understood (Davis et al. 1992; Watanabe et al. 1992). Type I systems have previously been hypothesised to encode for a filament-based mechanism of segregation (Barillà et al. 2005; Lim et al. 2005; Ebersbach et al. 2006; Bouet et al. 2007; Pratto et al. 2008; Batt et al. 2009). The presence of ParM polymers in type II partition systems had already shown that insertional polymerisation of the ATPase component is able to drive the segregation of plasmid pairs through a pushing force. This idea was extended to the type I system found in *E. coli* plasmid pB171. Here, observations of what appeared to be oscillating helical ParA polymers were made using epifluorescence microscopy (Ebersbach and Gerdes 2004). Many ParA ATPases had also shown to polymerise *in vitro* into long structures (Barillà et al. 2005; Leonard et al. 2005; Lim et al. 2005; Ebersbach et al. 2006; Bouet et al. 2007; Pratto et al. 2008; Batt et al. 2009). Further *in vivo* observations made using epifluorescence showed what appeared to be cloud-like ParA structures retracting towards the cell pole and “pulling” partition complexes through the cell (Fogel and Waldor

2006; Ringgaard et al. 2009; Ptacin et al. 2010). These combined observations supported a filament-based model of segregation of type I systems, like that used by eukaryotic chromosomes. These mechanisms however did not account for the affinity for non-specific DNA shown by Walker type ATPases.

Some of the most well studied type I partition systems are that of the P1 and F plasmid of *E. coli*. Both systems encode for the two proteins (ParA and ParB) and a centromere-like site (*parS)* (although termed SopA, SopB, sopC in F plasmid, where Sop stands for stability of plasmid). The partition systems for both of these plasmids was reconstituted *in vivo* and visualised using TIRF microscopy, revealing directed motion of partition complexes in the absence of ParA filaments (Hwang et al. 2013; Vecchiarelli et al. 2013; Vecchiarelli, Seol, et al. 2014). A subsequent model was proposed for the segregation of plasmid pairs following these reconstitutions known as the "diffusion-ratchet model". Within this model, partition complexes at the plasmid origin interact with ParA dimers throughout the volume of the cell to facilitate their segregation (**Figure 4**). To form the partition complex, ParB dimers bind specifically to the *parS* sites, located near the plasmid origin. Multiple ParB molecules are recruited to the site forming the large nucleoprotein complex at its location. ParB within the partitioning complex then binds to ParA-ATP* which is bound non-specifically to the DNA of the cell nucleoid. This binding anchors the origin region of the plasmid to the nucleoid whilst simultaneously triggering the hydrolysis of ParA-ATP* to ParA-ADP. Since ParA-ADP does not support DNA-binding, it is released from the nucleoid. ParB within the partitioning complex subsequently binds to nearby areas of the nucleoid that are rich in ParA-ATP*, and the process repeats itself. The continuous cycle of bind, hydrolysis, and release results in the movement of the partitioning complex along the length of the nucleoid, leaving a low concentration of bound ParA in its wake. The time delay between the conformational changes from ParA-ATP to ParA-ATP* is important to this mechanism as it allows sufficient depletion of ParA from the nucleoid to encourage the partition complex to move along. Unlike the filament-based mechanism of type II, the diffusion-ratchet model suggests that the nucleoid plays a key role as the structure to which the partition complex anchors itself intermittently throughout segregation. Understanding of the underlying mechanism of type I partition systems is significant due to it being the most abundant subset of partition systems found in bacterial DNA, with almost all ParABS systems encoded on bacterial chromosome bearing closest resemblance to this group (Gerdes et al. 2000). These models have therefore proved invaluable for beginning to unravel the secrets of bacterial chromosome partitioning. Walker-box ParA proteins have more recently been identified in the segregation systems of archaeal plasmids and chromosomes (Gerdes et al. 2000; Kalliomaa-Sanford et al. 2012; Schumacher et al. 2015; Barillà 2016). The widespread conservation of Type I systems means

understanding their mechanisms of action will deepen our knowledge of not just chromosome segregation in bacteria, but across multiple domains of life.

Type I systems vary between different organisms greatly, prompting them to be further subclassified into type Ia and Ib. The proteins encoded for by type Ia, ParA (251-420 aa) and ParB (182-336 aa), are significantly larger than the homolog proteins found in Ib systems, ParA (208-277) and ParB (46-113 aa). Type Ia ATPase proteins include the well-studied ParA protein from the ParABS system of *Escherichia coli* P1 plasmid and are typified by an extra N-terminus not found in type Ib ParA homologues. A DNA-binding motif in this N-terminus allows these ATPases to autoregulate their own transcription by binding to DNA sites within the *par* promotor which blocks *parAB* transcription. (Ebersbach and Gerdes 2005). This switch in roles for partitioning protein to transcription regulator occurs when ParA proteins are bound to ADP (Davey and Funnell 1994), using their long N-terminal helix-turn-helix (HTH) domains to bind specifically to the operator sites (Bouet and Funnell 1999; Dunham et al. 2009).

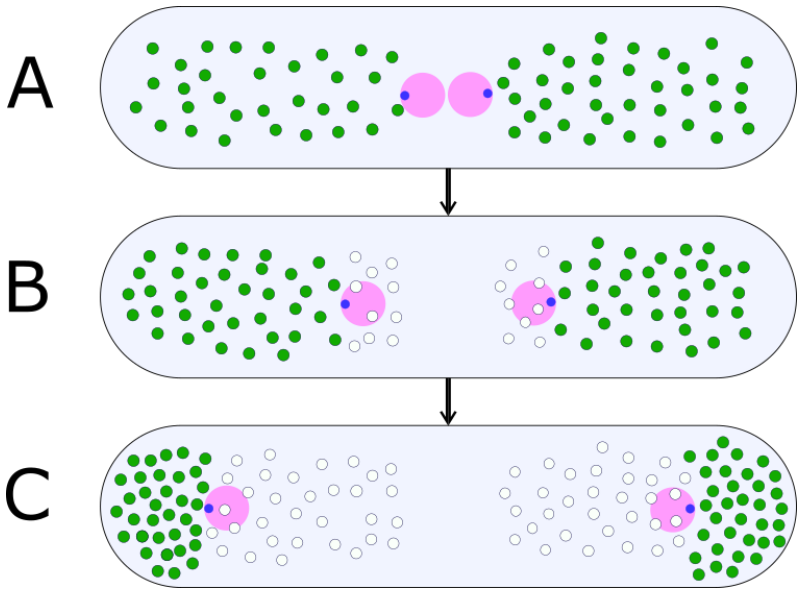

Figure 4. Model for plasmid segregation by diffusion ratchet mechanism in type I partition system. *(A) ParB binds to parS to form partition complex (blue) on plasmid (pink). (B) Partition complex binds to ParA dense regions (green) of the nucleoid, triggering their ATPase activity. This clears the nucleoid of ParA, leaving a depletion zone (white). (C) The partition complex continues to bind to ParA-enriched regions, gradually moving towards the cell pole.*

1.3.1.2 Type II

The most well studied subgroup of partition systems is type II. These are comprised of an actin-like ATPase (ParM), a partition site binding protein (ParR) and a partition site (*parC).* The structure of ParM is similar to that of actin, forming filaments composed of two chains of molecules entwined with one another (Van den Ent et al. 2002; Graceffa and Dominguez 2003). Studies of the ParMRC system which facilitates the segregation of R1 plasmid copies in *E. coli* showed that ParM filaments formed between sister plasmids during segregation. ParM filaments were observed to bridge

between plasmids and elongate, physically pushing the plasmids apart (Møller-Jensen et al. 2002). Through the use of TIRF microscopy, a fluorescent variant of ParM was seen to form dynamically unstable filaments in the presence of ParR (Garner et al. 2004). This was the first time that dynamic instability had been observed for any biological polymer outside of eukaryotic microtubules. It was hypothesized that this dynamic instability of ParM filaments provided the force which powers segregation in type II *par* systems. The ParMRC system from R1 plasmid was reconstituted to better understand the mechanics of type II segregation (Garner et al. 2007). ParM filaments up to 3 μm in length were observed to emanate from *parC*-coated beads in the presence of ParR and ATP. These filaments were seen to grow and shrink from the surface of the beads dynamically, searching out the surrounding space for other *parC*-beads. When the unattached end of a ParM filament interacted with ParRC complexes on another bead, the filament stabilised and elongated, pushing the beads further apart. Elongation of the filaments was confirmed to be powered by insertional polymerisation of ParM monomers near to the ParRC complexes bound at either end of the filament (Møller-Jensen et al. 2003). These findings helped develop the following model for segregation of plasmids in bacteria. *In vivo*, it is understood that ParM filaments emanate from ParRC complexes on bacterial plasmids. These filaments "search and capture" ParRC complexes on replicate plasmids, stabilising the ParM filament between them. The bound ParRC filaments accelerate the growth of the filament through catalysing insertional polymerisation at the bound tips, pushing the plasmids at either end apart (Gayathri et al. 2012). As the filament grows, it aligns with the longitudinal axis of the cell. Once the plasmids reach opposite poles, the ParM filament depolymerises, with the deposited plasmids sufficiently spaced away from each other. Cell division can now occur with each cell inheriting a copy of the plasmid. This model is illustrated in **Figure 5**.

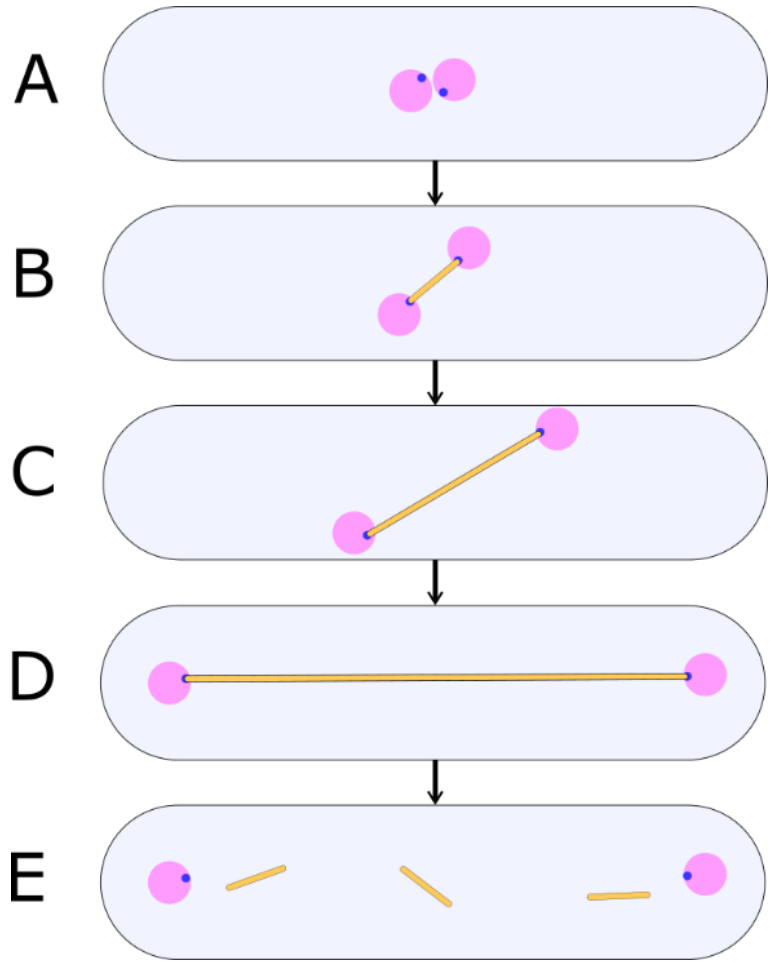

Figure 5. Model for plasmid segregation by action of type II partition system. *(A) Replication of plasmid (pink) at mid-cell. (B) ParM filament "search and capture" and stabilise between ParRC complexes (blue) on both plasmids. (C, D) The stabilised filament elongates, pushing the plasmids apart. (D) The elongating filament aligns with the longitudinal axis of the cell and positions the plasmids at the cell poles. (E) The ParM filament depolymerises, leaving the plasmids at opposite ends of the cell in preparation for division.*

1.3.1.3 Type III

The other subgroup of partition systems which segregates DNA cargo through the dynamic instability of filaments is type III. These systems encode for a GTPase (TubZ) which is distantly related to tubulin, a partition site binding protein (TubR) and a partition site (*tubC)*. The TubZRC loci has been identified on the large, virulence plasmids of various *Bacillus* species (Tang et al. 2006; Akhtar et al. 2009; Hoshino and Hayashi 2012). TubZ from *Bacillus* plasmids has been shown to polymerise *in vitro,* forming two or four strand filament bundles (Anand et al. 2008; Chen and Erickson 2008; Aylett et al. 2010; Montabana and Agard 2014). *In vivo* observation of TubZ-GFP from *Bacilus thuringiensis* pBtoxis plasmid found that TubZ filaments were polarised, with a recognisable plus end and minus end (Larsen et al. 2007). TubZ monomers were observed to polymerise at the plus end of the filament and disassemble from the trailing minus end. The apparent motion of TubZ filaments through the cell was hypothesized to occur from a treadmilling mechanism. This occurs when a filament grows at one end at the same time as shrinking from the other end. This

observation was coupled with evidence that TubRC forms a ring like structure (Aylett and Löwe 2012), capable of interacting with C-terminal extensions found on TubZ filaments (Ni et al. 2010). A mechanism was therefore proposed where the TubRC ring structure can hitch a ride on treadmilling TubZ filaments, facilitating their segregation to the cell poles. A reconstitution of the TubZRC system was used to elucidate how the movement of TubZ filaments translated to the segregation of plasmids (Fink and Löwe 2015). During the reconstitution, observations made using TIRFM showed that TubRC complexes tracked the depolymerising end of TubZ filaments. This provided evidence for a mechanism where a treadmilling filament exerts a pulling force on a plasmid that can effectively segregate it to the cell pole. The entire segregation mechanism is illustrated in **Figure 6**. Here, the TubRC complex on a plasmid binds to the shrinking minus end of a treadmill TubZ filament. As the TubZ filament moves along the long axis of the cell, the TubRC complex tracks the minus end of the filament, pulling the plasmid towards the cell pole. Upon reaching the pole, the plasmid detaches from the filament, coming to rest.

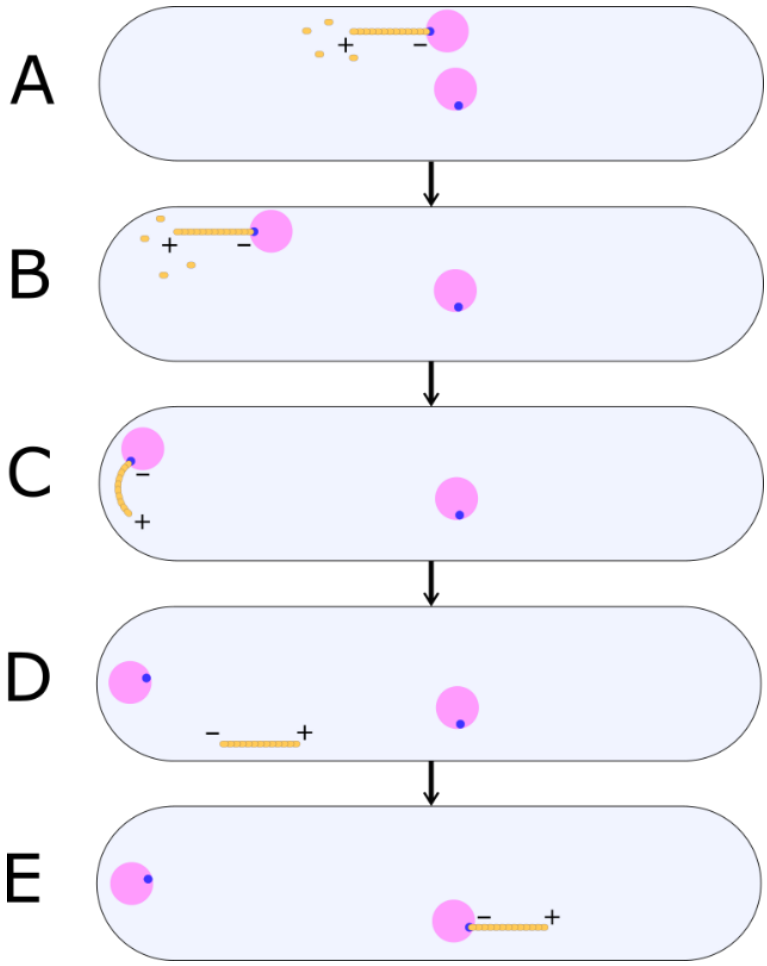

Figure 6. Model for plasmid segregation through treadmilling of TubZ filaments. *(A) TubRC complex (blue) binds to treadmilling TubZ filament at shrinking minus end. (B) Treadmilling of filament exerts a pulling force on the TubRC filament and its attached plasmid (pink), moving them along the long axis of the cell towards the pole. (C, D) TubRC detaches from filament at cell pole, depositing the plasmid. (E) Mechanism continues, clearing plasmid copies from mid-cell and transporting them to cell poles.*

1.3.2 ParB properties

Mechanisms for the segregation of DNA molecules rely on the formation of dense nucleoprotein complexes termed partition complexes. These complexes are formed at centromere-like sites along the plasmid or chromosome, termed *parS.* The site is recognised and bound by a site-specific protein, ParB. Centromere-binding proteins are typified by the presence of either a helix-turn-helix (HTH) or ribbon-helix-helix structural motif. All ParB proteins encoded for by bacterial chromosomes are of the HTH variant. The structure of ParB proteins can be broken down into three key domains: A C-terminal domain which allows ParB dimerization, a central domain for *parS* binding and a N-terminal domain for protein-protein interactions (**Figure 7**).

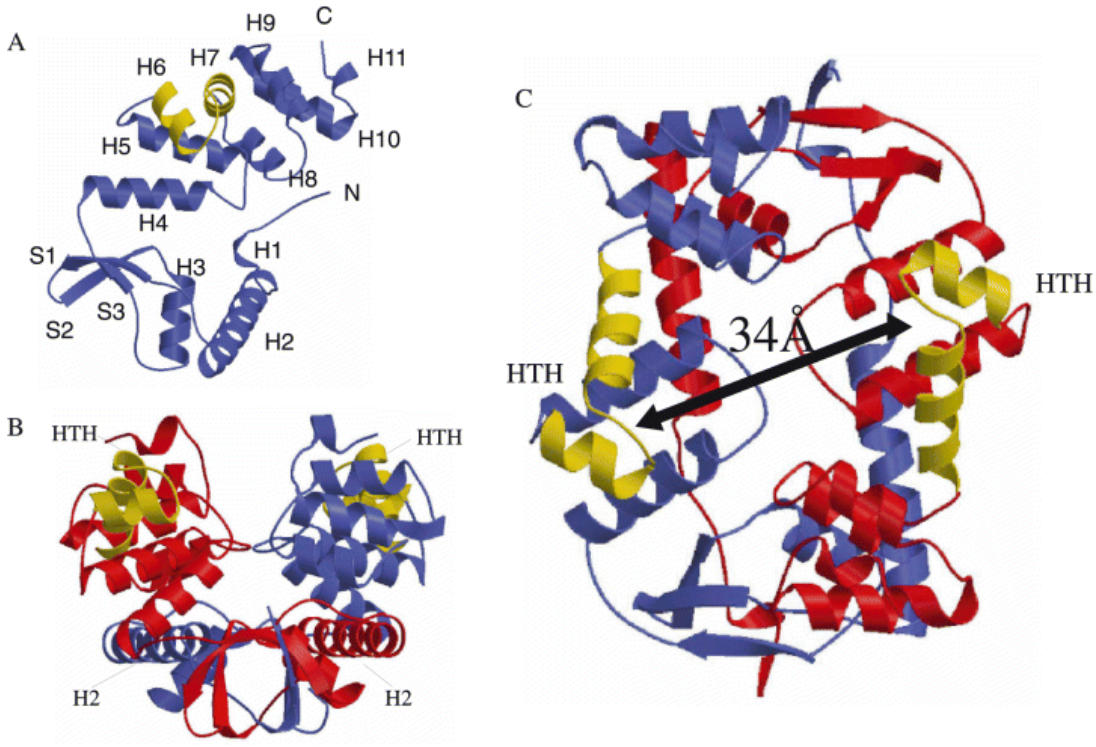

Figure 7. Structure of chromosomal ParB from Thermus thermophilus. *(A) Spo0J monomer, (B) Spo0J dimer and (C) a top-down view of the dimer. HTH motifs are coloured yellow. The N-terminal interfaces are identified by H2. A 34 Å distance is present between the HTH domains of the dimer* (Leonard et al. 2004).

An important characteristic of HTH ParB proteins is their ability to form higher-level complexes by spreading along the centromere-like site (Murray et al. 2006; Breier and Grossman 2007). This spreading is uncommon among site-specific binding proteins but has been demonstrated to be essential for proper partitioning activity (Rodionov et al. 1999). Chromatin immunoprecipitation (ChIP) measurements have confirmed this spreading, revealing that ParB binds non-specific DNA either side of the *parS* site, as far as several kb away from the location of the *parS* sequence. The bound concentration of ParB is highest at the location of the *parS* site and reduces non-linearly as distance from the *parS* site increases. Another indication of spreading is the ability of some ParBs to silence the expression of genes nearby *parS* sites, particularly when ParB is overexpressed. Silencing of genes is most likely a side effect of ParB spreading and has not been found to contribute to the partitioning process (Rodionov and Yarmolinsky 2004). Debate continues over how these large complexes can be seeded by so few *parS* associated ParB proteins. Several models have therefore been proposed to how ParB is recruited to the *parS* site and assembles into the large nucleoprotein complex required for partition. One of these models known as the “DNA bridging model” suggests that ParB interactions occur between dimers both horizontally along the DNA molecule and vertically between different *parS* sites (Graham et al. 2014). All three domains of the ParB protein are thought to be key to the spreading behaviour it exhibits *in vivo* on *parS* sites situated within bacterial chromosomes. Firstly, ParB binds to a *parS* site through its central HTH domain and

dimerises through its C-terminal domain to stabilise itself. The flexible N-terminal is then able to interact with other ParB dimers, allowing the large complex to spread horizontally along adjacent chromosomal DNA. These dimer-dimer interactions also occur vertically between *parS* sites, bridging across the chromosome and forming the large nucleoprotein complex. ParB bridging between *parS* sites on separate plasmids also presents an explanation for how plasmid pairing occurs. Mathematical modelling has supported the theory that ParB bridging, along with 1D spreading along the DNA is required for stable nucleoprotein complexes to form on chromosomes (Broedersz et al. 2014; Fisher et al. 2017).

The N-terminal domain of the ParB proteins is flexible, which has made it difficult to elucidate its structure using X-ray crystallography methods. However, recent structural studies have successfully identified this N-terminal ParB domain located within the protein PadC from *Myxococcus xanthus* (Lin et al. 2017; Osorio Valeriano et al. 2019). PadC acts as an adapter protein, recruiting ParA molecules to the bacterial cytoskeleton at the cell-poles, aiding the DNA partitioning activity of the ParABS system. The solved crystal structure of the N-terminal ParB domain revealed a tightly bound cytidine triphosphate (CTP) ligand. The discovery of a CTP-binding pocket led to the revelation that CTP binding is necessary to the proper function of the domain and therefore the mechanism of all proteins which possess it. Mutations introduced to the CTP-binding region within PadC inhibited the protein's ability to interact with ParA, suggesting that domain must be bound to CTP to enable PadC to interact with ParA. Sequence comparisons confirmed that this CTP-binding pocket is a highly conserved feature within homolog ParB proteins, meaning that CTP interactions may be involved within the mechanism of the wider ParB-family of proteins. CTP was introduced to the ParB protein from the chromosomal ParABS system of *M. xanthus*, with notable interactions taking place between the protein and nucleotide. *In vivo* visualisation compared wild-type ParB to mutants which did not permit CTPase activity. This study showed that both binding and hydrolysis of CTP by ParB dimers was required for formation of a partition complex and therefore for partition of chromosome pairs. The necessity of CTP for partition complex formation and ParB spreading on chromosomal DNA has also been confirmed *in vitro*. Here, purified ParABS components from *Caulobacter crescentus* showed that ParB only exhibited spreading onto DNA adjacent to *parS* sites in the presence of CTP (Jalal et al. 2020).

1.4 Chromosomal segregation models

Chromosomal ParABS systems encode for a Walker-type ATPase to segregate the origin region. Chromosome based *parABS* loci have been found within numerous bacterial species, including *Bacillus subtilis*, *Caulobacter crescentus* and *Myxococcus xanthus* (Mohl and Gober 1997; Kim et al.

2000; Autret et al. 2001; Godfrin-Estevenon et al. 2002; Jakimowicz, Brzostek, et al. 2007; Jakimowicz, Zydek, et al. 2007; Harms et al. 2013; Lin et al. 2017). The ParABS system has been shown to be essential in multi-chromosomal bacteria species such as *V. cholerae* and *Burkholderia cenocepacia* (Yamaichi, Fogel, and Waldor 2007; Passot et al. 2012). The force required to segregate the origin regions of bacterial chromosomes with *parABS* loci is suggested to be provided by ParA (Lee et al. 2003). The partition complex which forms at the chromosome origin is transported through the cell from its initial position through interactions with ParA-ATP throughout the volume of the cell. ParA is a weak ATPase, which is hydrolysed in the presence of the partition complex. This hydrolysis is known to provide the energy needed for segregation, but how chromosomes harness this energy to produce directed motion of the partition complex remains unclear. This uncertainty has spawned several models for the mechanism of chromosome origin segregation through ParABS, all aiming to account for the dynamics observed *in vivo*.

1.4.1 ParA dynamic filaments

Some of the earliest models for the mechanism of ParABS in chromosomes were based on the filament driven segregation systems found in eukaryotes. It is was proposed that ParA forms dynamic filaments that associate with the origin region of the chromosome and pulls it towards the cell pole (Fogel and Waldor 2006; Ptacin et al. 2010). This was supported by observations of *V. cholerae* chromosome dynamics, where epifluorescence microscopy revealed what appeared to be ParA filaments spanning between the cell pole and the chromosome origin (Fogel and Waldor 2006). These filaments appeared to exert a pulling force on the origin region by contracting towards the pole. Similar observations of ParA filaments within the cell arose from studies in *C. crescentus.* These observations together led to a model based on a spindle-like mechanism similar to that of eukaryote chromosome segregation (Ptacin et al. 2010). Within this model, the partition complex interacts with a filament composed of polymerised ParA molecules. ParB within the partition complex triggers the depolymerisation of the ParA molecules from the bound end of the filament. Subsequent reattachments to the shrinking filament result in the displacement of the partition complex towards the cell pole. This model appeared to corroborate observations of ParA forming linear filaments *in vitro*. These filaments also showed affinity for DNA, whilst addition of ParB was shown to remove ParA from DNA.

1.4.2 'Diffusion-ratchet' and 'DNA-relay' models

The apparent observation of ParA filaments exerting a pulling force on the chromosome established a mitotic filament-based mechanism as the leading model for origin segregation. It was not until further investigation into the mechanism of ParABS systems in plasmids that a non-filament model was proposed. Here, the ParABS systems of P1 and F plasmids were reconstituted *in vitro* using the

three purified components encoded for by their *par* locus (Vecchiarelli et al. 2010; Hwang et al. 2013; Vecchiarelli, Seol, et al. 2014). These components were visualised using total internal refection Fluorescence microscopy (TIRFM) and showed that directed movement of partition complexes was achievable without the presence of ParA filaments. Partition complexes were shown to interact with DNA-bound ParA dimers, triggering their hydrolysis and a local depletion of ParA. The partition complexes exhibited directed motion as they searched out higher concentrations of ParA dimers across a DNA surface. This was the first model to propose that instead of utilising filaments, the partition complex uses ParA protein gradients to propel itself across the cell (Hu et al. 2015; Hu et al. 2017). Protein gradients and protein pattern formation appeared to provide the force required for the segregation of plasmids. After proving that segregation of plasmids through protein gradients was possible, this new 'diffusion-ratchet' model was tested on chromosome ParABS systems. Simulations of chromosome segregation in *C. crescentus* based on the diffusion-ratchet model showed that displacement of the partition complex from its starting position at one pole to the opposite pole was possible (Lim et al. 2014; Surovtsev, Lim, et al. 2016; Surovtsev, Campos, et al. 2016). However, directed diffusion of the partition complex through ParA concentration gradients was not enough for persistent motion to be achieved. The elastic dynamics of the underlying nucleoid structure had to be factored in before sufficient movement of the partition complex from pole to pole was achieved. These investigations led to a new model being built upon the initial diffusion-ratchet, where the partition complex binds intermittently to DNA-bound ParA within the nucleoid. The movement of the nucleoid then causes the partition complex to be passed to other ParA rich regions in a relay mechanism. This model, termed 'DNA-relay' underlines the importance of the nucleoid as a dynamic scaffold on which the partition complex moves.

Observations of ParA proteins localised within high density regions (HDRs) within chromosomes have been made using 3D-structured illumination microscopy (3D-SIM), multifocus microscopy (MFM) (Abrahamsson et al. 2013), single-particle tracking PALM (Manley et al. 2008; Stracy et al. 2015) and widefield deconvolution microscopy (Marbouty et al. 2015; Le Gall et al. 2016). Here, plasmid partition complexes were observed to "hitch-hike" between high HDRs within the nucleoid through interactions with ParA. These observations suggest that segregation occurs primarily within the volume of the nucleoid, as opposed to the cytosolic space between the nucleoid and the cell membrane.

A subsequent model, known as the Venus flytrap, has since proposed where partition proteins segregate DNA molecules through a hybrid ParA polymer and gradient based mechanism (McLeod et al. 2017). Using super-resolution 3D-SIM microscopy, the ParF Walker ATPase from TP228 plasmid was observed to polymerise into a cage-like complex which permeates the nucleoid. Newly

replicated plasmids are shuffled through the cell volume as the ParF complex oscillates from pole to pole. As the complex oscillates, a network of ParF polymers grows between the sister plasmids until one copy falls off the trailing edge of the complex, deposited at the cell pole. The other copy remains bound within the cage complex and is transported and ultimately deposited to the opposite cell pole.

1.4.3 Par-independent chromosome segregation

The typical location of the partitioning locus near to the origin of replication hints at a role in the segregation and positioning of chromosome origins. However, how essential they are to this process is unclear. Many species, including *E. coli*, lack *par* loci within their genomes but still exhibit proper segregation and localisation of their chromosome origins (Li et al. 2002; Lau et al. 2003; Nielsen et al. 2006). Strikingly, many chromosomes which do encode for *par* loci show little change in their segregation and localisation dynamics when ParABS is deleted (Ireton et al. 1994; Webb et al. 1998; Kim et al. 2000; Lewis et al. 2002; Fogel and Waldor 2006). It has therefore been proposed that the ParABS system in many chromosomes refines and improves the efficiency of chromosome positioning but is made redundant by the presence of other drivers of DNA segregation.

Structural maintenance of chromosomes (SMC) proteins are widely conserved across all domains of life and are involved in numerous processes within chromosomes including DNA repair, segregation and condensation (Hirano 1999; Strunnikov and Jessberger 1999; Jeppsson et al. 2014). This includes bacterial chromosomes which also encode for ParABS loci. In *B. subtilis*, fluorescent variants of SMC have shown to associate with DNA, forming discrete foci along the nucleoid and also close to the cell poles (Britton et al. 1998; Graumann et al. 1998). During chromosome replication, SMC forms a complex with two other proteins: ScpA and ScpB. This complex is called a condensin. The condensin plays a pivotal role in the condensation of the bacterial chromosome through introducing positive supercoiling into DNA, forming superhelices (Kimura et al. 1999). This ability to condense DNA is hypothesized to partially drive the segregation of chromosome pairs. The exact mechanism is unclear, but recent single-molecule visualisations have shown that condensin complexes cooperatively interact to form a dimeric motor that forms condensed DNA (Kim et al. 2020). SMC complexes within opposite halves of a cell are thought to condense replicated chromosomes after their initial separation at the mid-cell. This way, each daughter cell inherits a copy of the chromosome. Some bacterial species, such as *E. coli*, do not possess a *smc* operon, but instead encode for a structurally similar protein, MukB. Similarly to SMC, MukB has been shown to associate with two other proteins, MukF and MukE to form a complex both *in vivo* and *in vitro* (Yamazoe et al. 1999). The presence of all three Muk proteins is essential for the correct segregation of *E. coli* chromosome pairs. However, the mechanism of SMC complexes and the ParABS system in some

bacterial species appear to be entwined. In *B. subtilis*, the SMC complex is recruited by ParB bound to the *parS* sites on the chromosome, causing the SMC complex to co-localise with the regions proximal to the chromosome origin (Sullivan et al. 2009).

Another model states that entropy is the primary driver of chromosome segregation in bacteria (Jun and Wright 2010). Unlike the mixing of individual molecules to maximise entropy, polymer chains achieve maximal entropy when they are separate. The properties of *E. coli* chromosomes appear to fit within this model (Romantsov et al. 2007), where strongly compressed chromosomes achieve maximal entropy when separated. Within this model, proteins such as ParAB and SMC complexes are used in a supporting role, separating, and positioning the chromosome origin, whist segregation of the bulk is due to entropy.

1.5 *Vibrio cholerae*

1.5.1 General introduction

The model organism which this project focusses on is the bacterial pathogen, *Vibrio cholerae*. *V. cholerae* is a Gram-negative bacterium that has short comma-shaped cells measuring 0.3 µm in diameter and 1.3 µm in length. Bacteria of the *Vibrio* family differ from most other bacterial species due to their possession of two circular chromosomes, as opposed to the more common single chromosome bacterium. A single flagellum at the cell pole makes *V. cholerae* highly motile throughout its life cycle within the host and the inhabited aquatic environments (Echazarreta and Klose 2019). The ability of *V. cholerae* to adapt to numerous environments throughout its lifecycle is essential to its pathogenicity it has exhibited throughout history. The presence of a divided genome has been proposed to confer benefits to their host organisms like *V. cholerae*, allowing them to potentially amplify genes present on individual chromosomes, dependent on their environment (Srivastava and Chattoraj 2007).

1.5.2 Pathogenicity

V. cholerae causes the diarrheal disease cholera which can be lethal if left untreated. Cases of cholera are estimated to be responsible for 21000 to 143000 deaths worldwide annually (Ali et al. 2015). Infection occurs through ingestion of contaminated food or water, making it especially prevalent in countries with substandard sanitation and poor access to clean drinking water. *V. cholerae,* along with other *Vibrio* species, are typically found in brackish water, making it part of the flora of estuaries and other coastal areas. Contamination of drinking water is a frequent source of infection. Upon ingestion, *V. cholerae* must withstand the acidic milieu of the stomach. *V. cholerae* grows best at neutral pH and has a low tolerance for acidic conditions. In order to survive this hostile environment, it is hypothesized that *V. cholerae* forms biofilms which provide increased physical

protection for the duration of acid exposure (Silva and Benitez 2016). After passing through the stomach, the bacteria reach the intestine. Colonisation of the small intestine epithelium is enabled by the toxin-coregulated pilus (TCP). These are a type IV pili which are long, thin and flexible appendages that help the cells to aggregate into microcolonies. The bacteria within a microcolony benefit from increased protection from the host's defences as well as the ability to concentrate the secretion of cholera toxin (CT). The released toxin binds to the membrane of intestinal epithelial cells. This triggers a rise in cyclic adenosine monophosphate (cAMP) which results in vast secretions of water and electrolytes into the intestinal lumen. This causes the onset of diarrheal symptoms, characterized by grey, cloudy diarrhoea, termed "rice water stools". During this process, vast quantities of the bacteria are shed by the host, introducing the bacteria to new aquatic environments from which they can be acquired by another host.

1.5.3 Chromosome segregation in *V. cholerae*

V. cholerae is of particular interest when studying bacterial chromosome dynamics as it features a genome which is divided into two chromosomes (Trucksis et al. 1998). Both chromosomes are circular with the larger chromosome I (Chr1) measuring 3 Mbp and chromosome II (Chr2) measuring 1 Mbp (Kirkup et al. 2010). *parAB* loci have been identified on both chromosomes, located near their respective chromosome origins of replication (Heidelberg et al. 2000). Comparison to homologue ParA and ParB proteins from other systems revealed that proteins encoded by the *parAB1* locus of chromosome I are similar to those of other bacterial chromosomes, whilst the parAB2 locus of chromosome II produces proteins which resemble those of plasmid partitioning systems (Yamaichi and Niki 2000). Replication of chromosome II is coordinated with the replication of a 150-bp locus on chromosome I, called *crtS* (Chr2 replication triggering site) (Val et al. 2016). The presence of the *crtS* region facilitates communication between the chromosomes, allowing them to coordinate their simultaneous replication termination (Rasmussen et al. 2007). Each chromosome has been found to encode its own partition proteins system, ParAB1 and ParAB2, which recognise distinct *parS* sites on each chromosome (Yamaichi, Fogel, McLeod, et al. 2007). The dynamics exhibited by the two chromosomes during their individual segregation processes are wildly different, with chromosome I pairs segregating asymmetrically from each other from a single focus located at the cell pole, and chromosome II pairs segregating symmetrically from the mid-cell position to the quarter-cell positions (**Figure 8**). The organism therefore provides a unique opportunity to study two distinct segregation machineries which co-exist and operate within the same cellular environment.

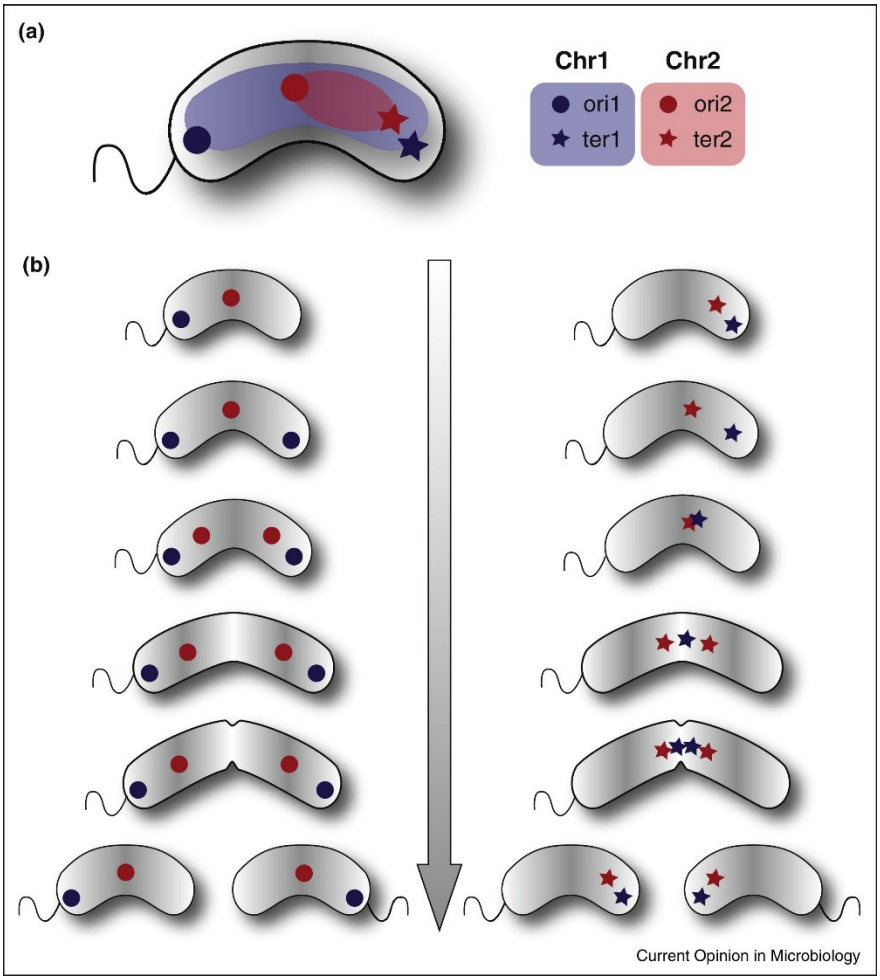

Figure 8. Localisation of origin and terminus regions of both V. cholerae chromosomes (a) *Spatial arrangement of V. cholerae chromosome I and II in a new-born cell.* ***(b)*** *Time-lapse of origin and terminus localisations during chromosome segregation process* (Val et al. 2014).

1.5.3.1 *V. cholerae* chromosome I

V. cholerae's larger chromosome, chromosome I, contains most of the essential genes associated with cell growth, metabolism, and cell structure. It also encodes for the major virulence factors associated with pathogenicity. The ParABS1 system of chromosome I mediates and fine tunes the polar localisation and asymmetric segregation of the chromosome's origin region. This process is independent of the segregation of chromosome II, with mutations in *parAB1* loci shown not to affect the partitioning of its origin region (Fogel and Waldor 2006). Three centromere-like sites, (*parS*1 sites) specific to the ParB1 adapter protein, are clustered within an 8 kb region located approximately 60 kb from the chromosome origin (Yamaichi, Fogel, McLeod, et al. 2007). ParB1 is recruited to the *parS1* sites to form a dense partition complex containing the origin region. Within the cell, the origin of replication for chromosome I is positioned at the old cell pole, anchored by a trans-membrane polar protein, HubP (hub of the pole). This anchoring is provided through interactions with ParA1 which retains the chromosome origin by binding the chromosome partition complex (Yamaichi et al. 2012). This anchoring of the chromosome origin to the cell pole resembles

that observed in *C. crescentus*, where a polar protein, PopZ, interacts directly with the chromosome's partition complex to retain the origin at the pole (Bowman et al. 2008; Ebersbach et al. 2008). The terminus region of the chromosome I is positioned at the opposite pole to the origin immediately after cell division but moves near the mid-cell position prior to DNA replication. As DNA replication commences, partition complexes formed on the origin regions of each sister chromosome commence segregation. This segregation occurs asymmetrically with one chromosome origin moving towards the opposite pole, leaving the other behind at the old pole (**Figure 8**) (Fogel and Waldor 2005; Val et al. 2014). The movement of the partitioning complex towards the new pole is coordinated with the dynamics of a diffuse cloud of ParA-ATP. The partition complex colocalises with the retreating edge of this cloud as it concentrates at the new cell pole. The retraction of the ParA-ATP cloud towards the pole exerts a "pulling" force on the partition complex which results in its translocation of the origin region from its initial position at the old cell pole, to the new pole (Fogel and Waldor 2006). As with other Walker-type ParA proteins, hydrolysis of ATP is required for them to exhibit the wild-type dynamics and localisation of the partition complexes. The cell divides after the chromosome replicates have fully segregated, with each new chromosome positioned as a mirror image to the original. Deletion of the *parA1* locus does not significantly disrupt the segregation of chromosome pairs, with cells still able to inherit a copy of chromosome I (Fogel and Waldor 2006). A lack of ParA1 however does result in the defective localisation of the chromosome origin to the mid-cell instead of the cell pole. (Saint-Dic et al. 2006). These observations support the possibility that the primary role of ParABS in chromosome I is to fine-tune the localisation of the origin regions to a very high proximity with the cell poles. The role of driving the translocation of the origin regions to opposite poles is therefore taken up by a number of other mechanisms such as the condensation of the chromosome by SMC complexes (Errington et al. 2005).

Original observations of the partitioning of chromosome I origins suggested a model in which ParA1 filaments mediate segregation of chromosome pairs. Here, one ParB1-*parS*1 partition complex is captured at the old cell pole by a ParA filament bound to a polar protein and retained here throughout the segregation process. The other partition complex bound to the sister chromosome origin is captured by a filament which extends from the new cell pole. This ParA filament was proposed to nucleate at the closing septum during cell division and gradually extend across the cell length. Once captured, interactions with the partition complex triggers the hydrolysis of ParA-ATP within the filament, causing the bound edge to depolymerise. The partition complex subsequently rebinds to the shrinking edge of the ParA filament and repeats this process until the origin reaches the new cell pole. Formation of ParA filaments has so far only been evidenced *in vitro* and not *in vivo*. Subsequent models based on the segregation of *C. crescentus* chromosome origins maintain

that ParA dimers can facilitate the movement of partition complexes through a diffusion-ratchet based mechanism. In this case, ParA concentrations which span the length of the cell, reaching a maximum at the new cell pole, have been shown to provide the appropriate force required for origin segregation (Lim et al. 2014). However, the movement of chromosome I's origin appears to be less dependent on its ParABS system than that of *C. crescentus*, with the origin able to move up to 80% of the cell length in the absence of ParA1 and ParB1 (Kadoya et al. 2011). Additionally, studies have shown that deletion of *parS* sequences from chromosome I does not alter the bulk longitudinal organisation of the chromosome, with origin still maintained at its polar position. Chromosome I therefore appears to have many other mechanisms, such as the condensing of the chromosome by SMC complexes, which are able to compensate for a missing ParABS system, therefore making it difficult to deduce how important ParABS to its maintenance.

1.5.3.2 *V. cholerae* chromosome II

V. cholerae contains a smaller secondary chromosome: chromosome II. Fewer essential genes are present on chromosome II than on its larger partner chromosome I. It is the presence of these essential genes however which grant it the status of chromosome as opposed to a large plasmid. Chromosome II also undergoes replication which closely resembles other chromosomes, where replication is initiated at a predictable time during the cell cycle. Plasmids on the other hand initiate their replication randomly (Leonard and Helmstetter 1988; Sengupta et al. 2010). The ParABS2 system of chromosome II is essential to the segregation and localisation of the chromosome's origin region. This has been demonstrated through mutations of the *parAB2* locus, which resulted in the random distribution of the origin regions throughout the cell and loss of chromosome II upon division (Yamaichi, Fogel, and Waldor 2007). 9 centromere-like, *parS2* sites, have been identified on chromosome II. 6 of these *parS2* sites are located within 70 kb of the chromosome's origin, with the remaining 3 located at least 100 kb from the origin. These *parS*2 sites are bound specifically by the adapter protein, ParB2. Recruitment of ParB2 molecules to the *parS*2 site forms a partition complex at the chromosome's origin region. ParA2 exhibits a dynamic localisation pattern, oscillating back and forth throughout the cell (Fogel and Waldor 2006). This localisation pattern is also exhibited by ParA homologues from plasmid systems (Ebersbach and Gerdes 2001; Lim et al. 2005; Adachi et al. 2006). It has been suggested that chromosome II was originally a captured megaplasmid which became incorporated into an ancestral *V. cholerae* (Heidelberg et al. 2000). This would explain the bias of essential genes located primarily on chromosome I. The presence of essential genes on chromosome II is thought to arise from its coevolution with chromosome I, causing the megaplasmid to become domesticated by the host cell as it gained genes conveyed upon it. Unlike most chromosomal ParA proteins, ParA2 is most similar to plasmid type Ia ATPases (Yamaichi and Niki

2000). This suggests a reason for the similarity between the segregation choreography displayed by chromosome II and that of plasmids. ParA2 also exhibits oscillatory patterns throughout the cell (Fogel and Waldor 2006), similar to those displayed by ParA homologs from plasmid systems (Marston and Errington 1999; Ebersbach and Gerdes 2001; Lim et al. 2005; Adachi et al. 2006; Hatano et al. 2007; Ringgaard et al. 2009; McLeod et al. 2017). Unlike other ParA homologs however, ParA2 is not able to form higher weight structures in the presence of ATP alone, requiring the presence of DNA to do so (Hui et al. 2010). Due to its smaller size, complete replication of chromosome II takes less time than in chromosome I. Initiation of replication in chromosome II is delayed, commencing after the replication phase of chromosome I has begun, coinciding with the replication of the short *crtS* region on chromosome I (Rasmussen et al. 2007; Val et al. 2016; Kemter et al. 2018). Prior to replication, the origin of chromosome II is located at the mid-cell position. The origin and its adjacent sites are replicated first and immediately begin to segregate, both moving away from each other towards opposite ends of the cell. The result of this symmetric segregation is the origins of the sister chromosomes positioned at the quarter cell positions, that upon cell division, become the mid-cell positions of the two daughter cells (**Figure 9**). Unlike chromosome I, ParABS is essential not just for the localisation of the origin proximal region but the segregation of the bulk of chromosome II (Yamaichi, Fogel, and Waldor 2007). Deletion of ParABS2 significantly disrupts segregation of chromosome II copies, resulting in anucleate cells. The essentiality of ParABS for the proper segregation of *V. cholerae* chromosome II resembles the reliance of plasmids on their related ParABS systems, supporting the hypothesis that chromosome II evolved from a plasmid ancestor. Cells that failed to inherit chromosome II and contained only a copy of chromosome I were shown to divide once more, evidencing that the absence of chromosome II itself does not restrict cell division. However, the newly formed cells containing only chromosome I were shown to degrade into abnormally large cells, containing condensed nucleoids. These cytological changes are believed to be in part due to the activation of toxin-antitoxin system, causing the death of cells and a loss of pathogenesis (Yamaichi, Fogel, and Waldor 2007).

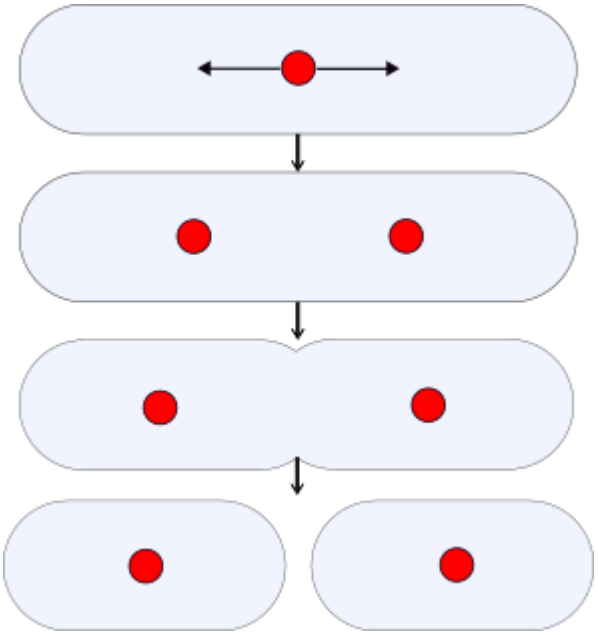

Figure 9. Movement of V. cholerae chromosome II origin during segregation. *The origin of chromosome II (red) replicates at the mid-cell position. The two copies then segregate to the quarter cell positions. Upon division, the origins are positioned at the mid-cell of each daughter cell.*

The similarity between the segregation patterns of *V. cholerae* chromosome II and well-studied plasmid systems makes it a prime candidate to study the molecular mechanisms that underpin bacterial chromosome segregation. Could chromosome II, like many plasmids, uses ParA protein gradients to drive its movement? If so, how does this mechanism differ to translocate much larger DNA molecules such as chromosomes?

1.6 Microscopic methods for studying bacterial chromosome segregation

Traditionally, bacteria have been considered little more than bags of enzymes with little to no organisation of their internal structure. It was assumed that due to their small size and lack of membrane-bound organelles, random diffusion would sufficiently transport molecules to where they were required. In recent years, advances in microscopic imaging have begun to resolve the intracellular structure of bacteria and internal organisation of the bacterial nucleoid. The models that have been developed for the segregation of bacterial chromosomes are largely based on observations from fluorescence microscopy. This technique has been used extensively to determine the localisation of the different components of ParABS systems within the cell volume and compare between the localisation patterns of different species. Due to their size, bacteria, and the processes which occur within them, have historically been challenging to image.

Visualisation of smaller objects, including the proteins of chromosomal ParABS systems, was only possible after the introduction of epifluorescence microscopy (Webb et al. 1997). Epifluorescence microscopy has been used extensively to identify the localisation patterns of ParA and ParB proteins encoded on both chromosomes and plasmids. This technique was key to the discovery of the pole to

pole oscillatory dynamics of ParA protein "clouds" and their co-localisation with partition complexes bound to plasmids, as well as translocation of bacterial chromosome origins (Ebersbach and Gerdes 2004; Adachi et al. 2006; Fogel and Waldor 2006). The same technique was also used to confirm the location of *parS* sequences by identifying where on the chromosome fluorescent variants of ParB adapter protein localise. The filament-based models for the mechanism of ParABS in the segregation of chromosome origins was developed from observations made during these epifluorescence experiments, producing images of what appeared to be dynamic filaments of ParA.

Total internal reflection fluorescence microscopy (TIRFM), a microscopy technique which illuminates a thin volume of the sample to increase signal to noise has been used successfully to further understanding of bacterial DNA segregation. Using this technique, diffusion ratchet-based mechanisms were developed from observations made during *in vitro* reconstitution experiments of the ParABS systems of P1 and F plasmids (Hwang et al. 2013; Vecchiarelli et al. 2013; Vecchiarelli, Neuman, et al. 2014). TIRFM was also used to study how the presence of CTP molecules affects the binding and spreading of ParB around *parS* sites (Soh et al. 2019).

Confocal microscopy has also been used to study the interplay between ParA, ParB and *parS in vivo* and *in vitro*. Using this technique, researchers revealed that archaeal pNOB8 ParA interacts with the bacterial nucleoid of *E. coli*, evidencing the non-specific nature of the ParA-DNA interaction (Zhang and Schumacher 2017). This data indicates that ParA proteins from different species can bind the nucleoid of different species. Due to limited resolution in z-axis microscopy, the majority of ParABS localisation studies have been conducted using 2D methods. Our understanding of the localisation of ParABS components within bacterial cells has since been expanded into the third dimension. 3D Structured Illumination Microscopy (SIM) observations of ParABS components from both plasmids and chromosomes located within the nucleoid volume (Le Gall et al. 2016). The development of models based on ParABS systems has therefore occurred alongside advances in microscopy and will continue to unveil how they function to segregate both plasmid and chromosome origins.

Despite these imaging-based studies, the molecular mechanism which governs chromosome segregation remains unclear. The generation of ParA depletion zones has been shown to create protein gradients capable of translocating both plasmids and carbon-fixing organelles within bacteria (Vecchiarelli, Neuman, et al. 2014; Maccready et al. 2018). It is unknown if a protein gradient mechanism exists for chromosome segregation. If it does exist, how does it differ to allow for the translocation of much larger cargo, such as chromosomes? For plasmids, the presence of ParA, ParB and DNA containing *parS* is sufficient to create directed movement. Could this hold true for chromosomes, or are other factors such as DNA elasticity vital to the process? (Lim et al. 2014)

1.7 Aims and objectives

How ParABS systems on bacterial chromosomes function to segregate chromosome origins is relatively unknown. ParABS is essential for the maintenance of *V. cholerae* chromosome II, and cells lacking this chromosome become abnormally large and die. ParABS is believed to be responsible for relocating the recently replicated origin region from the mid-cell towards the quarter-cells position (**Figure 10**). Current models now lead away from a ParA-filament based model, towards a diffusion-ratchet mechanism where the partition complex is positioned through interactions with ParA concentration gradients through the cell volume. However, experiments involving high-resolution imaging and computer simulations still leave a lot of uncertainty about the exact molecular mechanisms of chromosome segregation. For instance, can translocation of chromosomes occur purely through the action of protein gradients? Better understanding of how chromosomes move and segregate to new daughter cells will aid understanding of the bacterial cell cycle. Cell-free reconstitution has been key to improve our understanding of the molecular mechanisms involved in the segregation of plasmids and carbon-fixing organelles within bacteria (Hwang et al. 2013; Vecchiarelli et al. 2013; Vecchiarelli, Neuman, et al. 2014; Maccready et al. 2018). I therefore believe a cell-free reconstitution will help tie together knowledge of the biochemistry of ParABS systems and the *in vivo* dynamics of chromosomes.

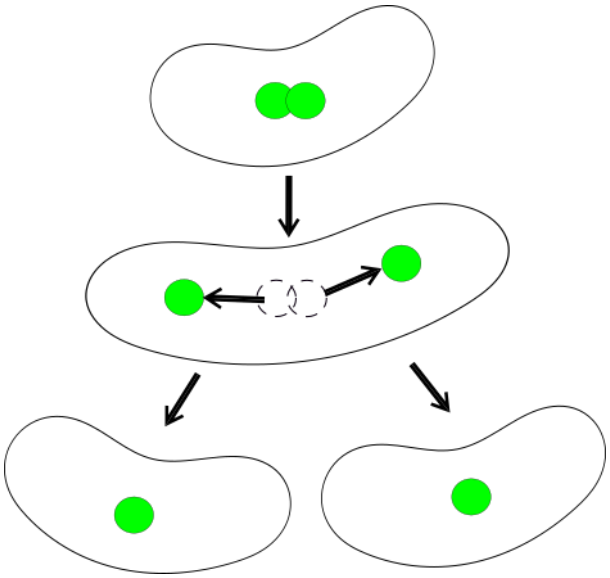

Figure 10. Segregation of V. cholerae chromosome II origins prior to cell division. *Chromosome origins (green) undergoes replication at the mid-cell position and segregates to the quarter-cell positions. Upon cell division, the origins (along with the rest of the chromosome) are inherited by both daughter cells.*

Aim

The overall aim of this project was to investigate the molecular mechanism of chromosome segregation in bacteria, by building a custom TIRF microscope capable of visualising the partitioning

(*par*) system of *V. cholerae* chromosome II. Reconstitution of the system using purified components of the *par* system would aid in uncovering the interactions which produce directed DNA segregation and improve understanding of how this minimal system is sufficient to drive the segregation process. Additionally, a new technique which uses TIRF microscopy to detect single molecules diffusing in solution was developed. The intention of this was to use the current imaging system to image ParABS system components without the constraint of surface immobilisation.

Objectives

1. Build and optimise a single-molecule microscope capable of TIRF imaging in dual colour (Chapter 2).
2. Use TIRF microscopy to characterise ParA-DNA binding activity and its role within chromosome segregation (Chapter 3).
3. Reconstitute the ParABS segregation system of *V. cholerae* chromosome II (Chapter 4).
4. Develop an *in vitro* single molecule detection system which detects freely diffusing molecules within aqueous solution using TIRF illumination (Chapter 5).

Chapter 2

Building and optimising a single molecule microscope capable of TIRF imaging in dual colour

I performed all the work and experiments involved within this chapter.

2.1 Introduction

Microscopy has had an important role in the development of ParABS models of chromosome segregation. One of the key techniques which have been used to successfully image ParABS systems is Total Internal Reflection Fluorescence Microscopy (TIRFM) (Axelrod 1981; Stout and Axelrod 1989). Here, illumination of the sample occurs within a thin electromagnetic field (evanescent wave) which is generated adjacent to the coverslip. To produce the evanescent wave, the illumination light is directed through a high refractive material, typically glass optics, towards a lower refractive index aqueous medium. The refractive behaviour of light at the boundary between the two mediums is governed by Snells Law:

$$n_1 \times sin\theta_1 = n_2 \times sin\theta_2$$

Where n_1 is the higher refractive index and n_2 is the lower refractive index. The angle of incidence the light beam makes with the normal of the boundary is θ_1 and the refracted angle for beam within the lower refractive index material is θ_2. When the angle of incidence θ_1 is sufficiently large, the refractive beam angle becomes 90°, causing it to propagate parallel to the boundary surface. This is termed the critical angle. Any incidence angle greater than the critical angle causes the light to reflect off the boundary and remain within the higher refractive index material. This reflection induces a thin electromagnetic wave within the lower refractive index medium, adjacent to the boundary. The electromagnetic wave is greatly diminished at increased distances from the surface, giving its name, the evanescent wave. The intensity of the evanescent field reduces exponentially as the distance from the interface increases:

$$I_z = I_0 e^{-z/d}$$

where I_z is the intensity at a distance of **z** from the interface and I_0 is the intensity at the interface. The penetration depth, d , of the evanescent field is given by:

$$d = \frac{\lambda_0}{4\pi}(n_2{}^2 \sin^2\theta - n_1{}^2)^{-1/2}$$

where λ_0 is the wavelength of the illumination light in a vacuum, n_2 is the refractive index of the higher density material and n_1 is the refractive index of the lower density material. The penetration depth of the evanescent wave, d, is therefore dependent on the incident angle of the light at the interface, θ.

In TIRF microscopy applications, fluorophores within the evanescent wave are excited and fluorescence. By limiting illumination to the thin depth conferred by the evanescent wave (~100 nm), only fluorophores close to the coverslip are excited (**Figure 11**). Therefore TIRFM offers a

greater reduction of out of focus light than epifluorescence and confocal. Unlike in confocal microscopy however, optical z-sectioning of the sample is not possible since the evanescent wave must always be adjacent to the coverslip surface.

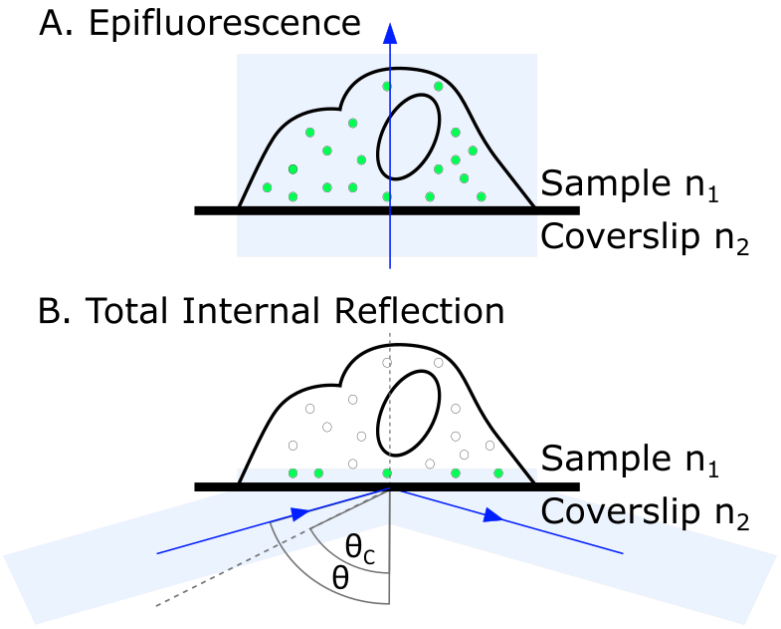

Figure 11. Difference between illumination provided by epifluorescence and total internal reflection. *(A) Epifluorescence provides illumination deep into the sample, exciting fluorophores throughout. (B) Total Internal reflection of the excitation laser at the sample/coverslip interface induces an evanescent wave which selectively excites fluorophores close to the coverslip surface. Total internal reflection only occurs at incident angles* (θ) *greater than the critical angle* (θ_C). (Figure adapted from Mattheyses et al., 2010).

The optical sectioning of TIRF microscopy makes it a great candidate for studying single molecules or small structures that are obscured by the fluorescence molecules outside of the plane of focus. Although the physics of the evanescent field constrains the use of the technique to the study of objects close to the coverslip, it is ideal for the study of surface and membrane bound molecules than other techniques struggle to image. **Table 1** below summarises the pros and cons of TIRF microscopy when compared to other techniques.

Pros	**Cons**
• Large field of view. • Reduced photobleaching and phototoxic stress to live cells. • Greater signal to noise performance.	• Shallow imaging depth. • Limited to samples close to coverslip surface.

Table 1. Pros and cons of TIRF microscopy when compared to other light microscopy techniques.

In recent years, TIRFM has become popular amongst biologists due to the availability of commercial setups and objective lenses specifically designed for TIRF, making achieving the necessary critical angle of illumination light simpler. Biological applications of TIRF include counting the number of

proteins within a membrane complex and measuring their motility, as seen in studies of MotB, a component of the bacterial flagellar motor which spans bacterial membranes (Leake et al. 2006). Here, live cells were tethered to a coverslip surface by the flagellum motor complex, allowing the imaging of individual proteins within the motor complex.

2.1.1 Prism-TIRFM

One way to create the shallow angle of incidence required for TIRFM is by using a glass prism to direct the light at the sample. The prism is typically placed on top of the sample, with the objective lens collecting the fluorescence emission signal from the reverse side of the mounted sample (Axelrod 1981) (**Figure 12**). This geometry benefits in a reduced background due to the separation of excitation and emission pathways as well as a larger range of incidence angles. Since the illumination light is not directed at the sample through the objective lens, a standard fluorescence objective can be used within this setup. A disadvantage of prism based TIRFM with modern inverted microscopes is that the emission signal must travel through the bulk of the medium before reaching the objective lens. This has the potential to increase light scattering within the sample, resulting in deterioration of the signal to noise. A second drawback inherent in this type of setup when used to study biology is the increased difficulty of sample manipulation. Owing to the placement of the prism a top of the sample, experimenters are required to employ microfluidics to inject samples or change buffer conditions during imaging. Overall, the reduced cost of a prism-TIRF due to the use of objective lenses which are cheaper than specialised TIRF objectives required for objective-TIRF is balanced with the increased difficulty of engineering and maintaining the setup. Prism-TIRFM has been an important tool in the study of bacterial segregation proteins, and has so far been the preferred method for capturing the dynamics of the ParABS systems from bacterial plasmids (Vecchiarelli et al. 2013; Vecchiarelli, Neuman, et al. 2014). The *in vitro* experiments for these systems relied on the dynamics of surface confined DNA cargo, making TIRF ideal for imaging these processes with the highest possible signal to noise.

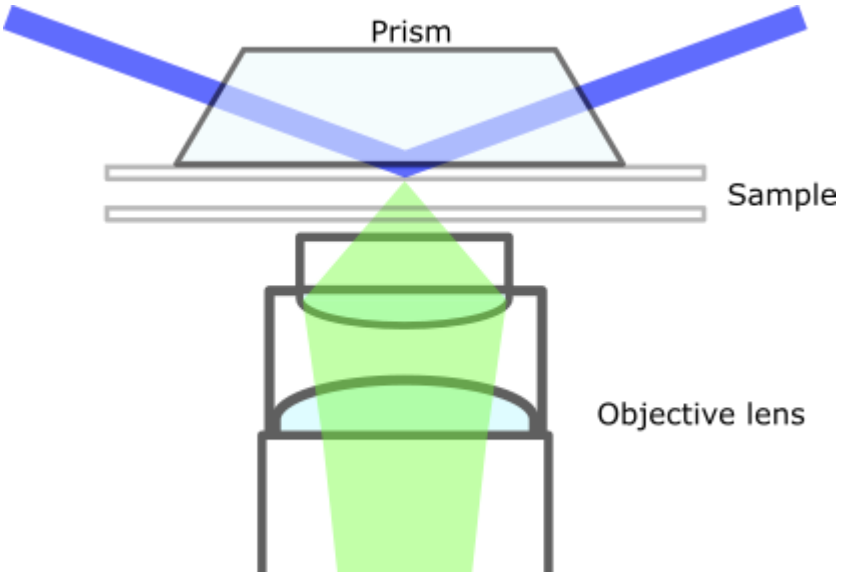

Figure 12. Prism based total internal refection fluorescence microscopy schematic. *Excitation light (blue) is directed towards a coverslip at an angle greater than the critical angle through a trapezoidal prism. The excitation light totally internally reflects at the interface between the coverslip and sample medium, inducing an evanescent wave on the interior surface of a sample chamber. Emission light (green) passes through the sample depth and is collected by an objective lens on the opposite side. The light is from there directed towards the detector.*

2.1.2 Objective-TIRFM

More recently, objective lenses have become available which are able to direct excitation light at the shallow incident angles required to perform TIRFM (Kawano et al. 2000). To do so, these objectives have particularly high numerical apertures (above 1.45), allowing refraction of the illumination beam to occur at the necessary incident angle. Emission light is then collected from the same surface by the objective lens (Stout and Axelrod 1989) (**Figure 13**). When used in conjunction with an inverted microscope, this geometry clears the top surface of any obstruction allowing access to the samples. This is of significant benefit to biologists which intend to change sample conditions during the imaging process. However, since the excitation and emission light are both present within the objective, careful use of fluorescence filters is needed to reduce the presence of unwanted wavelengths at the detector. Objective TIRF has been used to capture the dynamics of intercellular structures within bacteria, including the treadmilling behaviour of FtsZ, which is a central component to cell division apparatus (Yang et al. 2017)

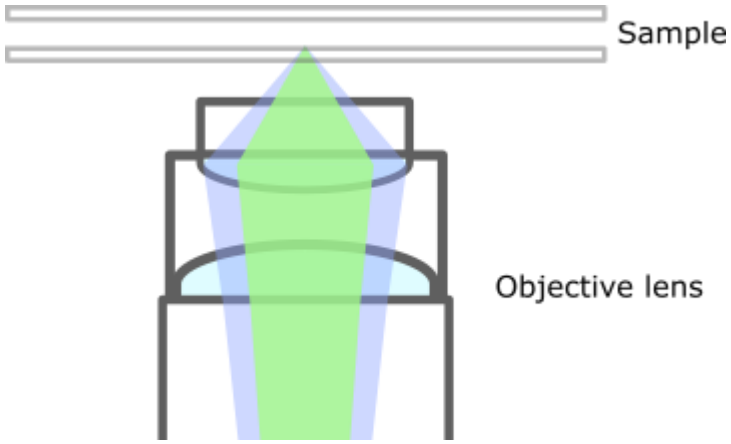

Figure 13. Objective based total internal reflection fluorescence microscopy schematic. *Excitation light (blue) is directed at the lower coverslip surface by an objective lens. The incidence angle of the excitation light is greater than the critical angle, causing it to reflect at the boundary between the coverslip and sample. This induces an evanescent wave adjacent to the interface, illuminating any nearby fluorophores. Emission light (green) is collected by the same objective lens and directed towards the detector.*

2.1.3 Building a TIRF Microscope for *in vitro* visualisation of ParABS

To better understand the molecular mechanism of chromosome segregation, I required a microscope which could directly image the protein-protein-DNA interactions and their dynamics in real time. My aim was to use TIRF microscopy to image purified proteins and isolated minimal components of the ParABS system of *V. cholerae in vitro* and reconstitute the dynamics which drives chromosome segregation. By studying the choreography of the molecular components of the ParABS system, I would gain direct insight into the molecular interactions that occur during chromosome segregation and how they create the directed transport of DNA seen in bacterial cells.

The experiments planned required a microscope capable of the following:

1. **TIRF capability**: High signal to noise imaging would capture the protein-protein-DNA interactions. This mode of microscopy had been used successfully during previous reconstitutions of plasmid partition systems (Hwang et al. 2013; Vecchiarelli et al. 2013; Vecchiarelli, Seol, et al. 2014)
2. **Multicolour fluorescence**: making it possible to identify and distinguish between different molecules using multiple fluorophore tags.
3. **Microfluidics**: to be used to surface immobilize DNA and allow for quick exchange of multiple samples and wash buffers during acquisitions (e.g. changing sample concentrations). This would all be required for the eventual reconstitutions of the ParABS systems of *V. cholerae.*

4. **Magnetic beads trapping**: previous reconstitutions of plasmid partition systems required magnetic confinement of ParABS components to the TIRF illumination surface to observe interactions and active segregation (Vecchiarelli, Seol, et al. 2014). This method is similar to the use of magnetic tweezers in fluorescence microscopy (Neuman and Nagy 2008).

Neither a commercial nor home-built microscope was available to use for this project with all the above features. Therefore, a custom microscope system would be built to include all the above features. **Figure 14** shows the basic layout which the microscope would follow.

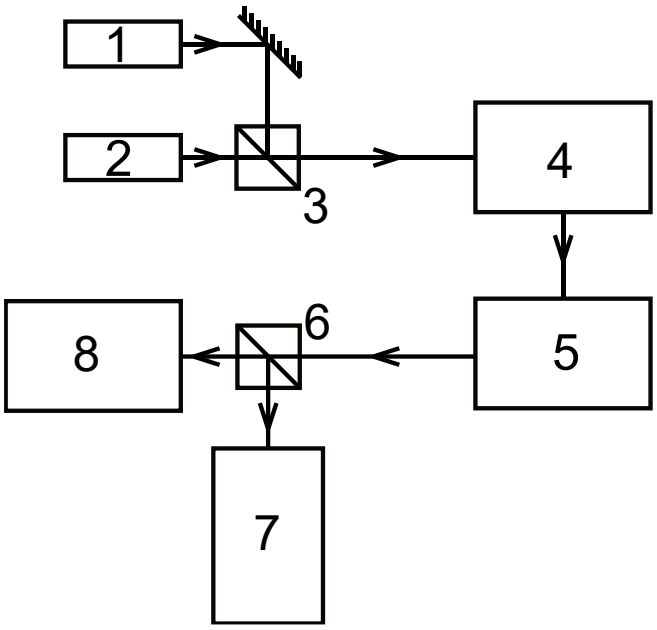

Figure 14. Initial schematic of Fluorescence TIRF setup. *The microscope would be built as a standard prism-based TIRF setup with two imaging channels for dual-colour imaging. (1 & 2) Two laser diodes output light at 488 nm and 633 nm wavelengths couple directly into single mode fibre optic cables. (3) The wavelengths are then combined onto the same path and coupled into a single fibre cable within a beam combiner. (4) The laser light exits the fibre through an attached collimator and focussing lens and is incident on the sample. (5) Emission light from the sample travels through the microscope body. (6) Two emission bandwidths are separated upon entering an emission splitter. (7 & 8) sCMOS detectors are used to capture the emission light.*

This chapter will discuss (i) construction of a bespoke prism-TIRF microscope starting with the selection of its hardware and components, (ii) the optimisations made to the assembled TIRF setup and (iii) modifications which had to be made before commencing any experiments on the ParABS system. The use of prism-TIRF over objective-TIRF was based primarily on higher signal to noise performance which is achievable. This is because the angle of incidence from the illumination light is not limited by the objective lens and stray light isn't as prevalent due to illumination of the sample taking place above the sample and not through the same objective which also collects emission.

2.2 Materials and Methods

2.2.1 Microscope body and objectives

The TIRF setup was built around a Nikon Ti-Eclipse microscope body. This inverted microscope base features a manual x-y stage for sample mounting, an objective lens turret and a fluorescence filter cube turret. Below the filter cube turret is an interchangeable tube lens which can be set to 1× or 1.5× magnification (f = 200 mm). The microscope body features multiple imaging ports for the attachment of detectors. The entire imaging setup was built on a passively damped optical table (Thorlabs), which reduces the impact of vibrations when imaging. A PlanApo 100 x NA = 1.45 oil-immersion objective (Nikon) was used for all the imaging within this project.

2.2.2 TIRF illumination

2.2.2.1 Lasers

Laser diodes (Cobolt MLD), with wavelengths measuring 488 nm and 633 nm, were used for laser excitation. These lasers provided a coherent light source for fluorescence microscopy. Laser light was coupled directly from the laser heads into a 1 m single-mode fibre with 3 mm jacketing. The lasers featured pig-tailing, where one end of the fibre optic cable is permanently fused to the laser diode, providing minimal back reflection at the site of laser coupling. The use of fibre optic lasers allowed the transmission of a beam with a high quality gaussian profile over long distances, compared to multimode fibres or free space lasers. The primary disadvantage of fibre coupling was the reduction of laser power by 50%. This reduced the respective 80 mW and 60 mW max powers of the 633 nm and 488 nm lasers to 40 mW and 30 mW. However, these laser powers were sufficient for the purpose of TIRF illumination.

2.2.2.2 Fibre-coupled laser combiner

In TIRF microscopy, the penetration depth of the evanescent field is related to the angle of incidence the excitation light makes with the surface of the sample. To achieve a similar penetration depth for both illumination wavelengths, both 488 and 633 nm lasers needed to be emitted from the same point above the prism. A laser combiner (OZ Optics) containing multiple dichroic mirrors was used to align and combine multiple beam paths and couple them into a single output fibre (**Figure 15**). The laser combiner we used was compatible with our 488 nm and 633 nm lasers which could be coupled directly out of their respective fibres by inserting them into the combiner.

Figure 15. Combining lasers into a single output fibre. *488 and 633 nm laser paths were combined into the same single fibre using a laser combiner (OZ optics).*

The penetration depth of the evanescent wave induced by each laser was calculated using the formula:

$$d = \frac{\lambda_0}{4\pi}({n_2}^2 \sin^2\theta - {n_1}^2)^{-1/2}$$

where λ_0 is the wavelength of the illumination laser light in a vacuum, n_2 is the refractive index of the higher density material (1.46; quartz) and n_1 is the refractive index of the lower density material (1.33; water). The penetration depth of the evanescent wave, d, is therefore determined by the incident angle of the laser light θ. The theoretical penetration depths of the evanescent waves induced by the 488 nm and 633 nm were calculated at 115 nm and 150 nm respectively.

2.2.2.3 Laser Focuser and mount

Laser light was emitted from the output fibre onto the sample through a polarisation maintaining collimator (OZ Optics) and containing a focussing achromatic lens f = 10 mm (OZ optics). The role of the collimator and lens was to convert the diverging illumination light emitted from the fibre into a coherent, convergent beam. The beam was incident upon the prism mounted to the microscope stage, directing illumination onto the sample. The collimator was positioned above the stage by a multi-axis (XYZ and rotational) optical fibre mount (Newport). The mount enabled fine adjustment to

the angle of the illumination light exiting the collimator. This level of control was essential for fine tuning the angle at which the laser beam hits the prism and therefore the properties of the TIRF field induced at the sample. The collimator mount was attached directly to the microscope *via* a custom platform (designed by a summer student, Pauline Vila Creus) (**Figure 16**). The platform could be adjusted to move the collimator mount up and down, and toward and away from the stage. By mounting the collimator directly to microscope base, the emission path of the illumination beam would be unaffected if the microscope were to move, saving on future alignment.

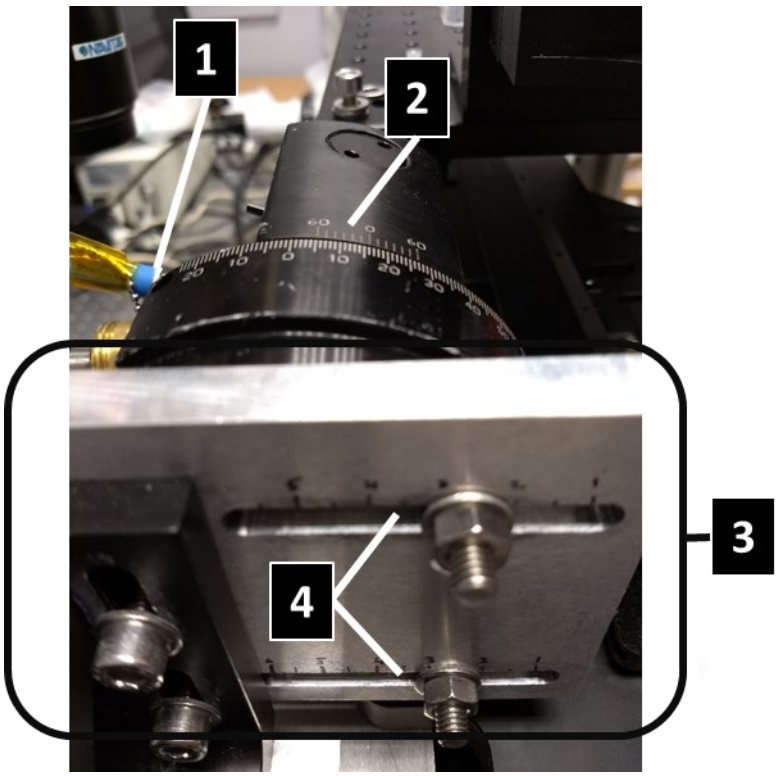

Figure 16. Multi-axis fibre mount attached to microscope by custom platform. *The beam angle can be adjusted using the fibre mount. (1) Fibre containing laser connected into back of collimator; (2) Collimator angle is adjustable through fibre mount; (4) Custom platform holds fibre mount above microscope stage; (4) Collimator position can be moved along machined tracks, allowing positioning closer to or further from sample stage.*

2.2.3 Emission path

2.2.3.1 Fluorescence detection

Fluorescence images were captured using a sCMOS camera (Prime 95B, Photometrics). Typical camera settings used were: exposure time 100 ms; frame rate 1 Hz; 16-bit depth. The exposure time was long enough to provide strong signals from fluorophore detections whilst not over saturating the pixels. The frame rate of 1 Hz provided sufficient resolution when plotting intensity over time whilst not exposing fluorophores to unnecessary illumination, prolonging fluorescence lifetime. The camera bias of 100 grey units was subtracted from measured intensities.

2.2.3.2 Fluorophores and filters

Green fluorescent protein (GFP) and Alexa 647 were used to fluorescently label samples. A Dual-view emission splitter (Photometrics) containing a dichroic mirror (ZT488/640rpc-UF2, Chroma) was used to separate green and red emission wavelengths. The 488 nm excitation laser line was removed with a notch filter (NF488-15, Thorlabs, centred at 488 ± 2 nm wavelength) placed within a custom filter holder. A bandpass filter (ET535/70m, Chroma) and a long pass filter (ET655lp, Chroma) were positioned inside the Dual-view filter cube.

2.3 Background

2.3.1 Fluorescence microscopy

The phenomena of absorption and subsequent emission of light by a compound, known as fluorescence, is one of the cornerstones of modern light microscopy. Use of fluorescence in light microscopy allows specific intracellular structures to be dyed, greatly improving the contrast and overall quality of any acquired images. The use of fluorescence in microscopy begins with labelling the structure of interest with a fluorescent substance (fluorophore). The fluorophore emits light at a specific range of wavelengths when illuminated by an excitation source. The emission light has a slightly longer wavelength than the excitation light, allowing it to be separated from other visible light sources within the image. This means that selective imaging of the fluorescent object can be obtained. The vastly improved contrast and resolution of fluorescence microscopy over traditional methods has unlocked new possibilities in the imaging of live cells and tissues, making it possible to study the components of the ParABS system, ranging in size from individual monomers (approx. 200 aa) to the larger partitioning complex which consists of tens of ParB dimers (100-700 aa) and several kB of DNA.

2.3.1.1 Fluorescence

Fluorescence is a phenomenon where a substance emits light after absorbing light from an illumination source. The process occurs over several steps, which are illustrated in the Jablonski diagram in **Figure 17** (Jabłoński 1933). First, absorption of an external photon excites the fluorophore from its ground state (S_0) to a higher energy state singlet state (S_1). To achieve this, the energy of the photon must be sufficient to bridge the gap between the ground and higher energy levels. Once in its higher energy state, multiple conformation changes and interactions with its environment causes a partial dissipation of energy. This non-radiative energy decay brings the molecule to a relaxed energy state at the bottom of the excited energy band. The time spent in the excited energy level is finite, typically lasting 1-10 nanoseconds. The molecule then undergoes rapid relaxation back to its initial ground energy state by radiating a photon. The emitted photon most often has a longer wavelength than the absorbed photon. This is known as Stokes shift and is the

result of the non-radiative energy decay which occurs within the higher energy state. The Stokes shift is fundamental to fluorescence microscopy as it allows the signal of emitted photons to be isolated from background noise and excitation wavelengths, improving image contrast and resolution.

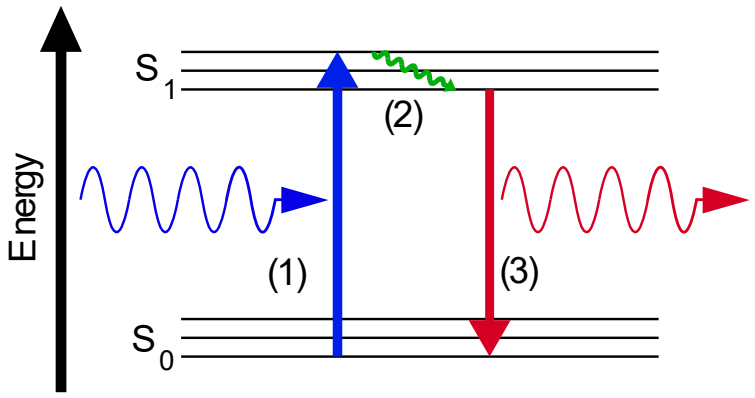

Figure 17. Jablonski diagram for typical fluorescent molecule. *(1) Photon (blue) absorption increases the energy of the fluorophore from the S_0 ground energy state to the higher S_1 energy state. The transition is very fast, on the order of 10^{-15} seconds. (2) Rapid non-radiative decay, causing the fluorophore to relax to the bottom of the S_1 energy band. The cause of this non-radiative decay is dissipation of energy into other vibrational modes. (3) Photon emission (red) occurs resulting in the relaxation of the fluorophore from the S_1* state back to the *S_0 state. This emitted light is detected as fluorescence. The resulting emitted wavelength is longer than the wavelength of light used to excite the fluorophore due to the loss of energy which occurs within the upper energy band.*

2.3.1.2 Fluorescent dyes and proteins

A wide selection of fluorophores is used to label biological structures. They vary in their suitability to bind certain biological targets and are available in a large variety of colours. A major group of fluorophores are fluorescent proteins, the first of which was green fluorescent protein (GFP). GFP is a protein that emits green light when illuminated by blue light, and was originally extracted from the *Aequorea victoria* jellyfish in 1962 (Shimomura et al. 1962). The use of wild-type GFP as a tool in microscopy, however, did not begin until its nucleotide sequence was reported, allowing it to be expressed in cells (Prasher et al. 1992; Chalfie et al. 1994; Inouye and Tsuji 1994). Subsequent derivatives of wild-type GFP led to improved performance in its role in fluorescence microscopy. More desirable fluorescence characteristics were developed such as greater brightness, a more efficient absorption at 488 nm and improved folding at 37°C, securing its place as a key tool in fluorescence imaging (Kilgard et al. 1995; Cormack et al. 1996). The use of fluorescent protein is no longer limited to just the green portion of the visible spectrum either. Colour mutations of the protein have produced blue, cyan and yellow derivatives of GFP, leading to the expression of fluorescent proteins across a range of wavelengths. Other advances in fluorescent protein technology include the development of monomeric variants (Campbell et al. 2002; Zacharias et al.

2002; Ai et al. 2006; Shaner et al. 2013). These are fluorescent proteins that do not oligomerize, a process which often affects the localisation and/or the function of the protein they are attached to. Techniques have been developed to allow researchers to fluorescently tag specific proteins of interest. One such way is through genetic labelling, where the fluorescent protein gene is fused onto the end of the DNA sequence which encodes for the protein of interest. An advantage of this labelling method is that subsequently produced molecules within the cell will be automatically fluorescently tagged. The location of these molecules can therefore be monitored as the cell grows. Also, no further manipulation of the sample is required for the expression of the fluorescent protein, reducing the related stress placed on the organism.

Another group of fluorophores used in microscopy to facilitate fluorescence are dyes. This group includes the popular rhodamine and cyanine derivatives which are commonly used in modern imaging. These molecules are typically bound to structures of interest using antibodies (termed immunofluorescence). Direct immunofluorescence labels the protein/structure with antibodies carrying the fluorescent dye molecule. Indirect immunofluorescence involves two types of antibody. The first antibody binds the protein/structure of interest. A second antibody, carrying the fluorescent dye, then binds specifically to the first antibody. Dyes are also commonly used to stain DNA, as seen in the application of DAPI stain. When bound to double-stranded DNA, DAPI exhibits strong blue fluorescence when illuminated by ultra-violet light. DAPI's ability to permeate the cell membrane makes it a popular choice for imaging nuclei and other DNA structures in fixed cells. Its ability to pass through the membrane is hindered in live cells, making it useful for identifying cells which have had their membrane compromised in viability assays.

2.3.2 Epifluorescence microscopy

A common mode of microscopy to visualise fluorescently labelled samples is epifluorescence. Here, light is passed straight through the microscope objective and into the bulk of the sample. This method of illumination allows for a wide angle of illumination and excitation of fluorophores deep into the sample, making it useful when studying thick samples. However, illumination of fluorophores outside of the focal plane can produce images with a high background signal, reducing overall signal to noise performance. Photobleaching is also a concern due to the intense illumination used within the technique.

Epifluorescence microscopy has been used successfully to localise chromosome and low-copy plasmid origins *in vivo* and capture time-lapse images of their movement within the cell during segregation (Gordon et al. 1997; Webb et al. 1998; Li and Austin 2002; Fogel and Waldor 2005; Fogel and Waldor 2006). The method has also been used to study the localisation of ParA and ParB

proteins within the bacteria, and observe how their dynamics influence the positioning of DNA (Ebersbach and Gerdes 2001; Ebersbach and Gerdes 2004; Fogel and Waldor 2006; Iniesta 2014). Out of these studies, one apparent observation was the formation of higher-weight ParA structures (Ebersbach and Gerdes 2004; Ebersbach et al. 2006; Ptacin et al. 2010). Such observations led to filament-based mechanisms which the bacteria use to segregate their DNA (Adachi et al. 2006; Fogel and Waldor 2006; Ringgaard et al. 2009; Ptacin et al. 2010; Shebelut et al. 2010).

2.3.3 Confocal microscopy

Widefield fluorescence microscopy passes excitation light throughout the bulk of the sample. This results in the excitement of fluorophores both inside and outside of the intended focus plane, increasing the background of the sample, limiting the achievable spatial resolution. This background can be dramatically reduced by confining illumination to a single focus plane (0.5 to 1.5 μm) of interest whilst imaging. Confocal microscopy uses a pinhole aperture within the excitation light path to selectively excite individual 2D planes orthogonal to the z-axis. A second pinhole in the emission path blocks light emitted from planes which are below or above the plane of interest. A diagram of the confocal microscopy setup is available in **Figure 18**. By selective illuminating and detecting emission light from individual 2D planes, background is significantly reduced, improving the overall image quality. The point illumination of confocal microscopy often means that simultaneous imaging of the entire sample area is not possible. In this case, the confocal illumination spot is scanned rapidly across the sample, measuring the emission intensity at each spot. The overall image is reconstructed once the entire sample has been scanned. The plane of interest can be adjusted through the sample, allowing optical sectioning of thick samples to be perform. The recombination of these individual planes results in a 3D composite image. Additionally, optical sectioning of live cells can be used to deduce the 3D localisation of these components within the cell volume. The increased resolution of confocal microscopy allows for observation of the individual components of the ParABS system. This technique was successfully employed to localise fluorescently labelled ParA from an archaeal pNOB8 plasmid (Zhang and Schumacher 2017). Through observation of archaeal ParA binding a bacterial nucleoid, this experiment demonstrated that ParA binds the DNA of exposed nucleoids, regardless of species.

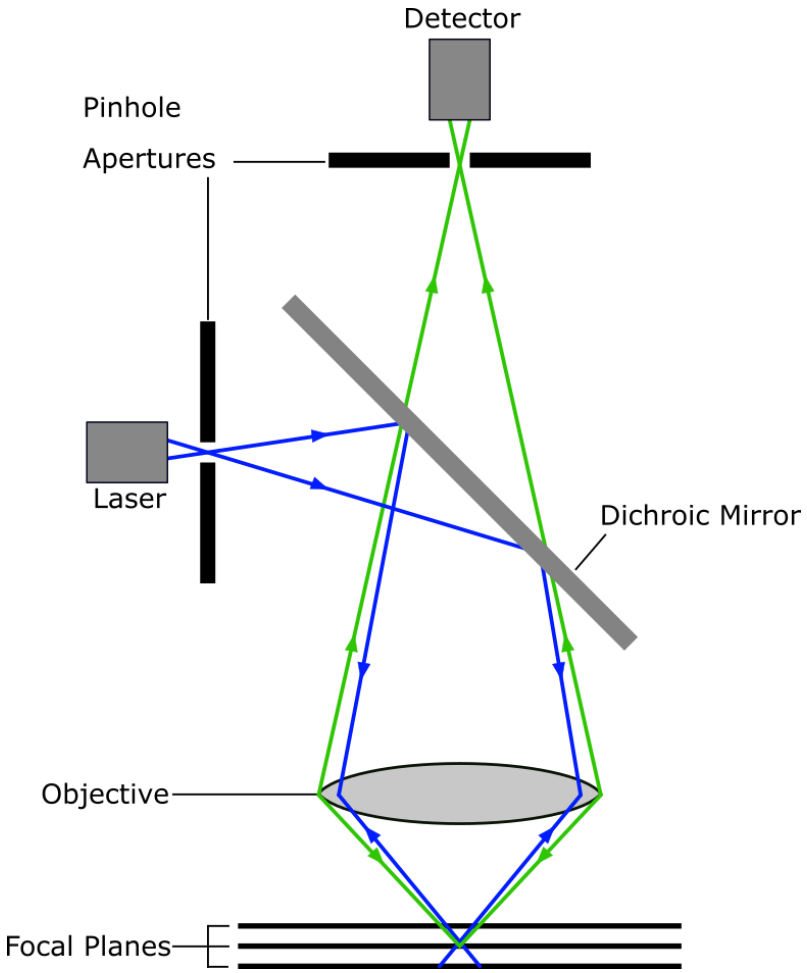

Figure 18. Diagram of a confocal microscope. *Excitation light (blue) from a laser source passes through a pinhole aperture and is reflected off a dichroic mirror, through the objective lens and onto a 3D sample. The excitation pinhole allows for selection of a particular 2D plane. Emission light (green) from the sample passes back through the objective lens, through the dichroic mirror. A pinhole aperture in front of the detector rejects light from out of focus planes, reducing the overall background.*

2.3.4 Total Internal Reflection Microscopy (TIRFM)

2.4 Hardware selection

2.4.1 Prism-based TIRF illumination

A trapezoidal quartz prism with 70° sides (J.R. Cumberland) used to direct laser illumination towards the sample. The prism face closest to the collimator was orientated perpendicular to the incident laser beam (**Figure 19**). The beam would then reflect off the bottom face of the prism inducing an evanescent wave at the sample. The face of the prism which the excitation laser exits through was slightly angled off-axis by 3°. This angling reduced reflection from this surface back into the objective. Limitation of back scattered light into the objective ensures that illumination of the sample is only provided at the determined TIRF angle (**Figure 19**).

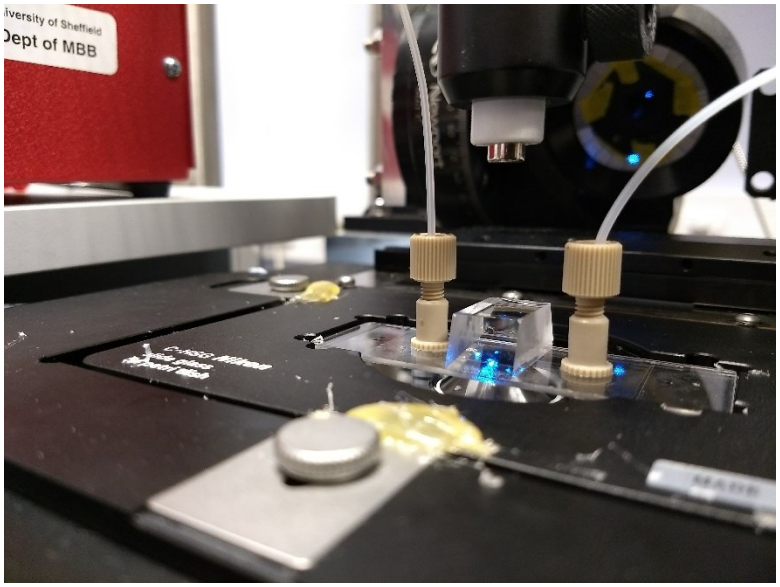

Figure 19. Prism mounted atop a flow cell. *Light from the collimator enters the prism via the perpendicular face. The exiting light beam leaves via the opposite, angled face preventing reflection of light back into the objective lens.*

2.4.2 Microscope objectives

A Plan Apo 100x / 1.45 oil immersion lens (Nikon) was used to provide the necessary high numerical aperture needed for TIRF whilst supporting corrections for chromatic aberration and field curvature. Chromatic aberration an issue present within lenses where different wavelengths are focussed to different focal points due to dispersion. Field curvature is another aberration where centre and edge of the field are never in focus at the same time due to the sharpest focus point existing on a curved surface, instead of a flat plane. The imaging resolution of the microscope had to be sufficient to image the interactions between the components of the ParABS system. Imaging resolution characterises the minimum resolvable distance between two objects. This resolution intrinsically is part determined by the numerical aperture (*NA*) of the objective lens; a measure of the objective's

ability to collect light over a range of angles. We can work out the minimum resolvable distance for a given NA using the following equation:

$$D = \frac{0.61\lambda}{NA}$$

Where *D* is the minimum resolvable distance and λ is the wavelength of illumination light. Since our illumination wavelengths are already set at 488 and 633 nm, the only way to reduce the minimum resolvable distance is to use a high numerical aperture objective lens. The maximum numerical aperture is however limited by the refractive index of the imaging medium. The relationship between the numerical aperture and refractive index of the imaging medium is given in the following equation:

$$NA = n(sin\theta)$$

Where n is the refractive index of the medium and θ is the maximum angle of image forming emission light which can be captured by the objective lens. The maximum numerical aperture of an objective which operates in air ($n = 1$) is around 0.95 due to $sin\theta$ only ever being less than or equal to 1. This means that the minimum resolvable distance achievable using an air objective when imaging GFP would be around 330 nm. For this reason, immersion lenses which image through synthetic oils have been developed and are commonly used in modern microscope setups. By using oil as the imaging medium, the refractive index can be increased beyond that of air, allowing greater numerical apertures and therefore greater resolving power to be achieved. Modern imaging oils have a typical refractive index of around 1.515. This increased index of refraction of the imaging medium results in a reduction of the minimum resolvable distance calculated at 330 nm to 215 nm.

2.4.3 sCMOS detector

An sCMOS detector (Prime 95B, Photomertics) was used to capture fluorescence images. Control of the detector was through Micro-Manager (Edelstein et al. 2010; Edelstein et al. 2014), an open source microscopy software. The software allows adjustment of variables such as camera exposure time, gain amount and framerate. All imaging and acquisitions would therefore take place through Micro-manager. Since the setup involved a single camera and minimal automated components, extra interface options offered by paid license software were not required. The exposure out port of the camera was connected to the illumination shutter driver, causing the shutter to open for the duration of each frame exposure. The camera was connected to the computer *via* the provided Prime 95B PCI express data cable and PCI express interface card installed onto the PC motherboard. The PCI express connection was more stable at higher data transfer rates since the USB 3.0 connection must shares bandwidth with other devices on the same bus. This means that increased

maximum data transfer rates (1064 MB/s) can be achieved when compared to a USB 3.0 connection. This is important since the Prime 95B's can produce high volumes of data when operated at high framerates.

2.4.4 Fluorophores and filters

Fluorophores used in multi-colour imaging should ideally have their own unique excitation profile, meaning a separate laser would be required for each fluorophore intended to use. We would need at least a pair of fluorophores in our experiments to make use of multi-channel imaging. Green fluorescent protein (GFP) was to be one of these pairs due to its wide availability and ease of use when tagging proteins. GFP has a peak absorption wavelength of 488 nm. Laser heads with an output wavelength of 488 nm are widely available and cheap, making it easy to obtain one for our setup. To ensure the second fluorophore we used was spectrally distinctive from GFP, we referred to the excitation and emission profiles of both fluorophores (**Figure 20**). Firstly, it was important that the emission profiles of the two fluorophores did not overlap to a significant degree. Any overlap would present potential fluorescence cross talk issues when imaging through multiple channels. We also needed to ensure that the absorption peak of the second fluorophore was well removed from 488 nm, to prevent cross excitation. In the end, we decided to use Alexa 647 dye as our second fluorophore since its excitation and emission spectra was sufficiently distinctive from that of GFP. Alexa 647 is also bright and commonly used in biological imaging applications. To excite Alexa 647, a laser with a wavelength of 633 nm was used.

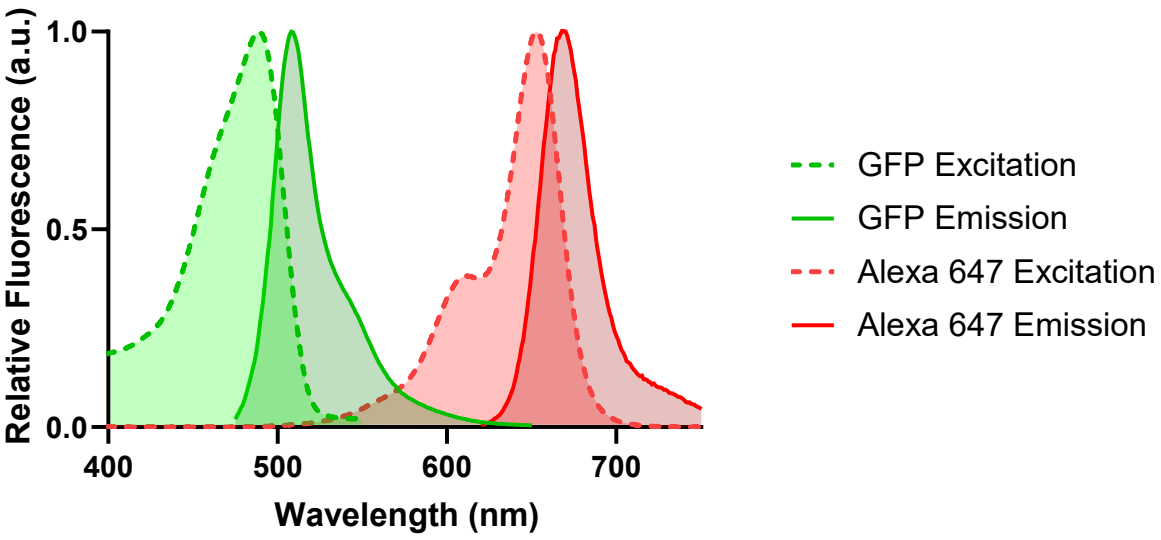

Figure 20. Excitation and emission spectra for Green Fluorescent Protein (GFP) and Alexa 647 fluorophores. *Excitation profiles (dotted lines) of GFP and Alexa 647 show strong sensitivity to 488 and 633 nm respectively. Emission profiles (solid lines) show very little overlap between fluorophores. Data obtained from chroma.com/spectra-viewer.*

2.4.5 Selection of optical filters for multicolour fluorescence and emission splitting

When excited, fluorophores emit photons at wavelengths corresponding to their emission spectra. For our system using GFP and Alexa 647, the emission signal consists of a mixture of green and red light. The ability to successfully separate the emissions of different fluorophores is key to multicolour imaging. A common technique is to use a series of emission filters and dichroic mirrors to separate the component emission wavelengths into distinct bandwidths. Each emission bandwidth is then detected by its own dedicated camera, meaning a separate camera is required for each colour to be imaged. As an alternative system, we chose to use an emission splitter to achieve multicolour imaging. An emission splitter allows multiple wavelengths to be detected within a single detector. It does this by diverting the emission paths of different wavelengths to separate sections of a camera pixel grid. This results in images produced by the detector that are spatially similar but spectrally different. The trade-off is a reduction of the field of view due to channels displaying the same area in multiple bandwidths. A Dual View emission splitter (Photometrics) was used to display two channels, green and red, onto a single detector. It contained a dichroic mirror (ZT488/640rpc-UF2, Chroma) which effectively splits green and red emission into two separate emission pathways. Each emission pathway also had filter slots in which emission filters could be positioned to block any undesired wavelengths from reaching the detector. Emission filters used at this location would be the final optics prior to the camera, providing an effective way to clean up the emission signal within both channels ahead of detection. The emission filters we selected for this purpose were a bandpass filter (ET535/70m, Chroma) for GFP emission and a long pass filter (ET655LP, Chroma) for Alexa 647 emission. Decisions on which dichroic mirror and emission filters to use were based upon emission spectra and transmission data for each filter (**Figure 21**)**.** The final emission path is illustrated in (**Figure 22**).

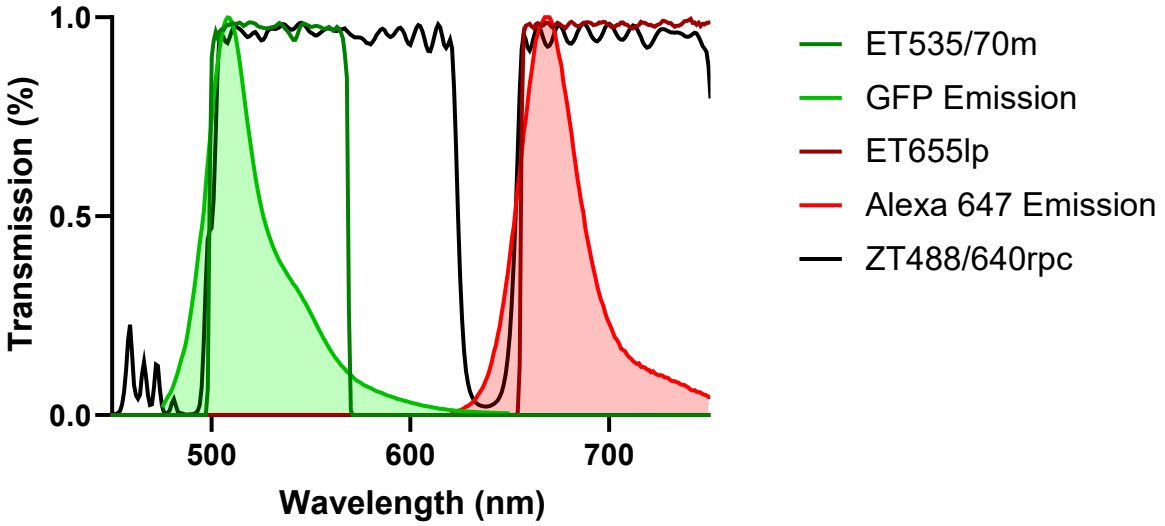

Figure 21. Transmission profile of optical filters in relation to GFP and Alexa 647 emission spectra. *A ZT488/640rpc dichroic mirror (black line) separates the emission wavelengths of GFP and Alexa 647. An ET535/70m bandpass filter (green line) and ET655lp long pass filter (red line) were positioned in the Dual View to select for the desired detection wavelengths in each channel.*

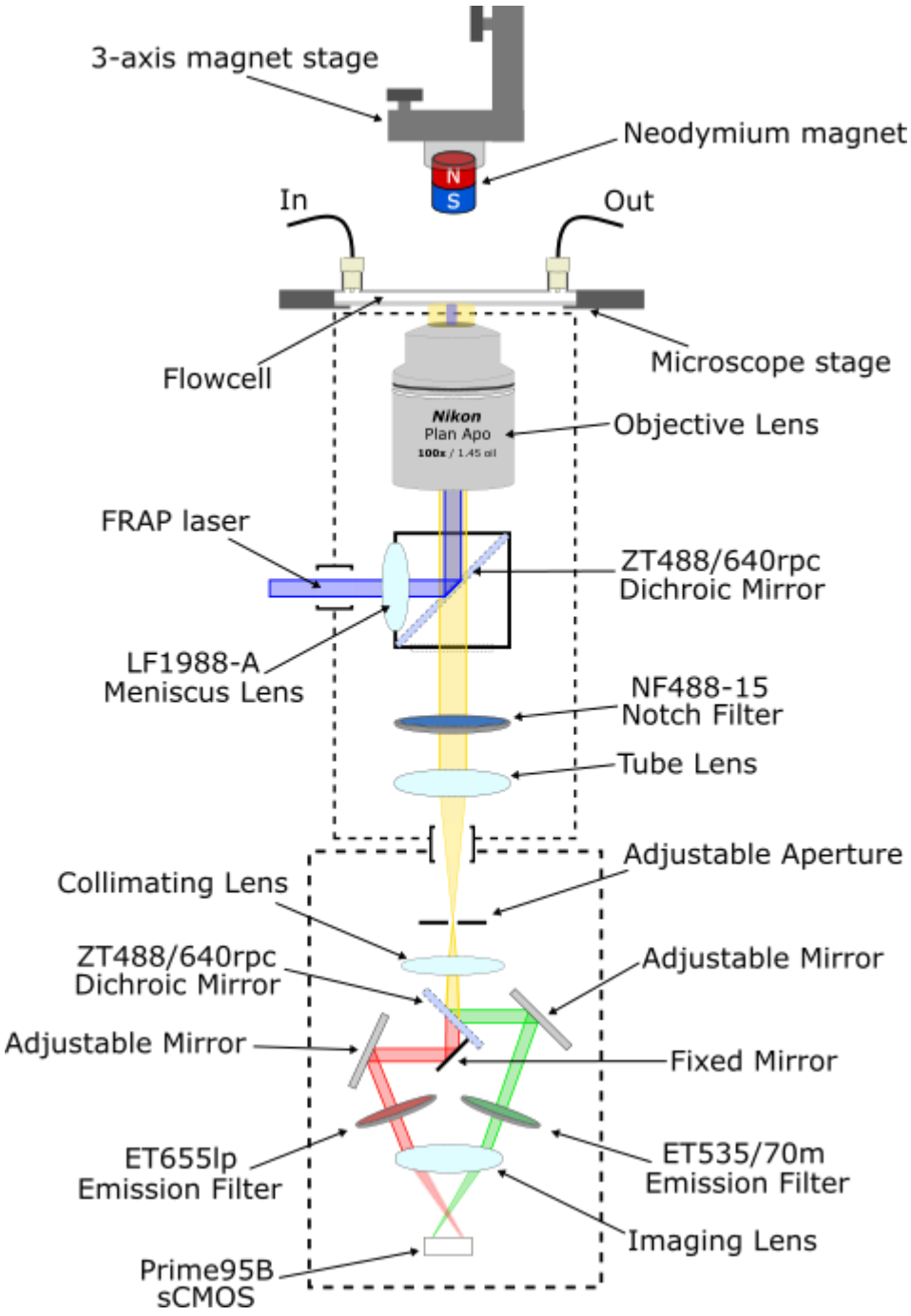

Figure 22. Emission paths within microscope body and emission splitter. *Manual x-y sample stage with mounted flow cell is illuminated. Emission light is collected by an oil immersion objective lens (Plan Apo 100x/1.45, Nikon). A fluorescence filter cube (Chroma) contains a meniscus lens (LF1988-A; Thorlabs) within the excitation filter slot to focus the FRAP laser to small spot. The FRAP laser is directed up through the objective lens by a dichroic mirror (ZT488/640rpc; Chroma) situated within the filter cube. The emission light passes through a 488 nm notch filter (NF488-15; Thorlabs) housed in a custom filter holder directly filter turret. The emission light then passes through the microscopes tube lens (f = 200 mm, Nikon). Upon exiting the microscope body, emission light enters an emission splitter (Dual View, Photometrics) containing a dichroic mirror (ZT488/640rpc, Chroma) and emission filters (ET535/70m & ET655lp, Chroma). The separated colour channels are directed onto an sCMOS detector (Prime 95B, Photometrics).*

2.4.6 Motorized Shutter for lasers

A blade shutter (LS2 2 mm Laser Shutter, Uniblitz) was installed directly after the fibre laser combiner to minimise fluorophore photobleaching during illumination. When engaged, the shutter

would block any light entering the output fibre and therefore any illumination of the sample. This reduced the time under illumination by using a shutter to block illumination between camera exposures. The electronic pulses required for automatic engagement of the shutter were provided by a dedicated shutter driver (VCM-D1, Uniblitz).

The shutter driver was connected to an exposure out port on the Prime 95B. The driver was configured to open the shutter only when it received a signal during camera exposure. This resulted in the triggered closing of the shutter between camera exposures, limiting the illumination of any sample strictly to the duration of each exposure. For a typical exposure time of 100 ms at intervals of 1 s, when using the automated shutter the sample would receive 1/10 of the laser illumination than when constant laser exposure was used over the same period of time.

2.4.7 Microfluidics and flow cells

The main challenge when designing a prism based TIRF setup is the inability to access the sample when mounted to the stage. Due to illumination entering from above the sample stage as opposed to through the objective lens, a method was required to allow modifications to the sample without having to remove it from the stage. To allow continued access to the sample during experiments, imaging chambers (flow cells) were connected to pumps, allowing the interchange of samples without disturbing the mounted imaging volume or prism (**Figure 23**).

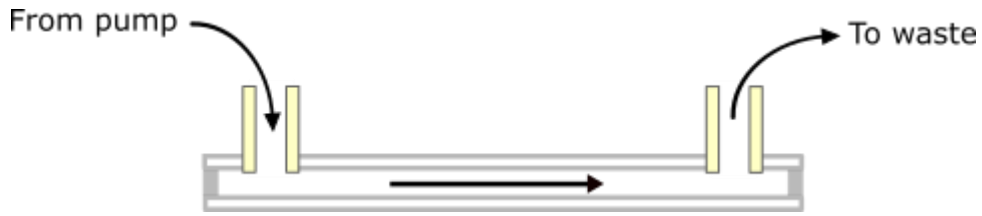

Figure 23. Flow cell flow dynamics of sample. *Sample is infused into the flow cell through an inlet port (left). The sample then proceeds though the volume of the flow chamber. The sample exits through an opposite port (right). This method allows a sample to be interchanged without having to remove a microscope slide from the sample stage.*

Flow cells were fabricated to be mounted to the microscope stage, working as small imaging chambers. Samples and buffers would flow through these flow cells from a connected syringe pump. To change the conditions inside the flow cell such as sample concentration and the presence of different proteins, the flow cells were designed to operate with connected syringes (B. Braun).

To minimise any scattering when the laser beam transitions between the prism and flow cell, the flow cells were constructed using a quartz slide (Esco), matching the refractive index of the prism. Immersion oil (Type FF, Cargille, n = 1.48) with a similar refractive index to quartz was used between the prism and flow cell to reduce refraction at this interface. This ensured that the laser light propagates through a near uniform refractive index until it is incident upon the sample.

The flow cells were constructed by sandwiching a piece of 25 µm thick double-sided tape (3M) between a quartz slide and glass coverslip. A central section measuring 4 mm wide and 34 mm long of the double-sided tape was removed prior to assembly using a laser cutter. Once assembled this formed an empty chamber sealed on all sides. The quartz slides featured two predrilled holes (diameter of 2 mm and spaced 30 mm apart) at either end of the flow chamber, meaning solution could be flowed through the chamber *via* the holes. The flow cells were heated to 120°C at which point the double-sided tape melts, bonding the quartz slide to the coverslip. Nano ports (UpChurch) were fixed atop of the inlet and outlet holes to allow connection to a syringe pump.

The inlet nano-port (UpChurch) of a flow cell was connected to a syringe pump (Al-1000, World Precision Instruments) using plastic tubing (TFZL 1/16" x 0.02", IDEX Health and Science) to allow solutions to flow through at a steady rate. The pump was also programmable, making it possible to automate the process *via* a connection to the microscope computer.

2.4.8 Confinement of magnetic beads using a z-axis magnet

With a diameter of 0.3 µm, the volume of a *V. cholerae* cell is significantly smaller than the 25 µm depth of our flow cells. Without a method of confining Par components to the TIRF illumination surface, imaging interactions would be difficult to achieve since. This was demonstrated by the inability to follow a partition once it had detached from the imaging surface during the reconstitution of P1 ParABS (Hwang et al. 2013). Therefore, a method was used where DNA-coated beads, representing cellular DNA cargo, are confined to the TIRF imaging surface by a magnetic force (Vecchiarelli, Neuman, et al. 2014). This method required a magnet to be suspended above the sample stage, directly above the prism and microscope objective (**Figure 24**). Once in position, the magnetic field held magnetic beads within the TIRF illumination field. This was an attempt to simulate the tight spatial confinement experienced by the partitioning complex as it navigates the narrow cytosolic corridor between the cell membrane and the nucleoid (**Figure 25**). This was an approximation, as I did not have a suitably shallow flowcell depth to recreate this tight space.

The magnet alignment process proceeded as follows:

1. The beads' movement was monitored and recorded for 15 min.
2. Bead trajectories were visualised to reveal the overall displacement of the beads.
3. If the beads were seen to drift as a group towards a given direction, the magnet position was altered to compensate for this drifting.
4. Step 1-3 were repeated until no group drifting was discernible and beads moved randomly under Brownian diffusion.

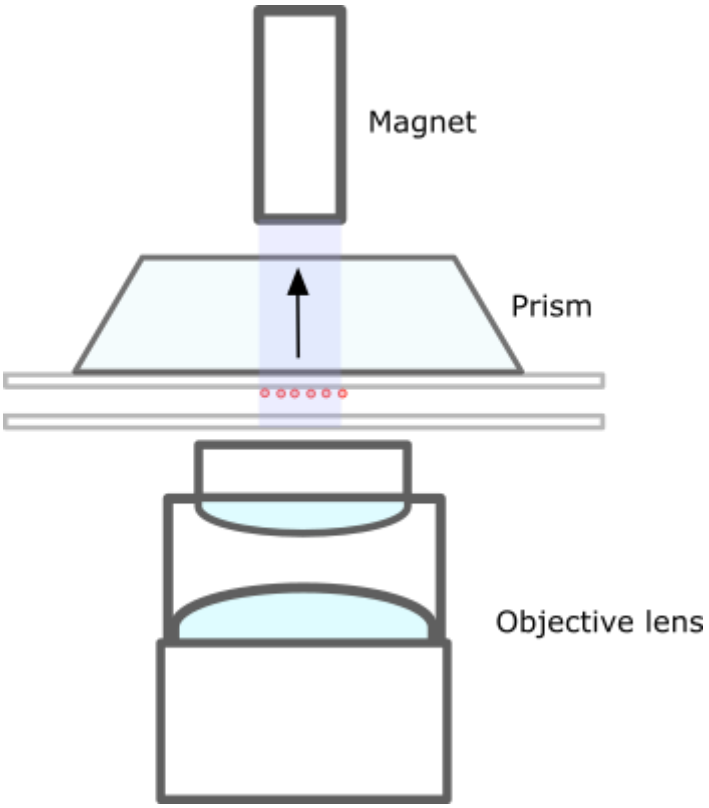

Figure 24. Magnet confines beads to upper surface of flowcell chamber. *A neodymium magnet was positioned directly above the flowcell chamber, in line with the objective lens. The magnetic field produced by the magnet was used to confine magnetic beads situated above the objective lens to the upper surface of the flowcell, where the evanescent field was present.*

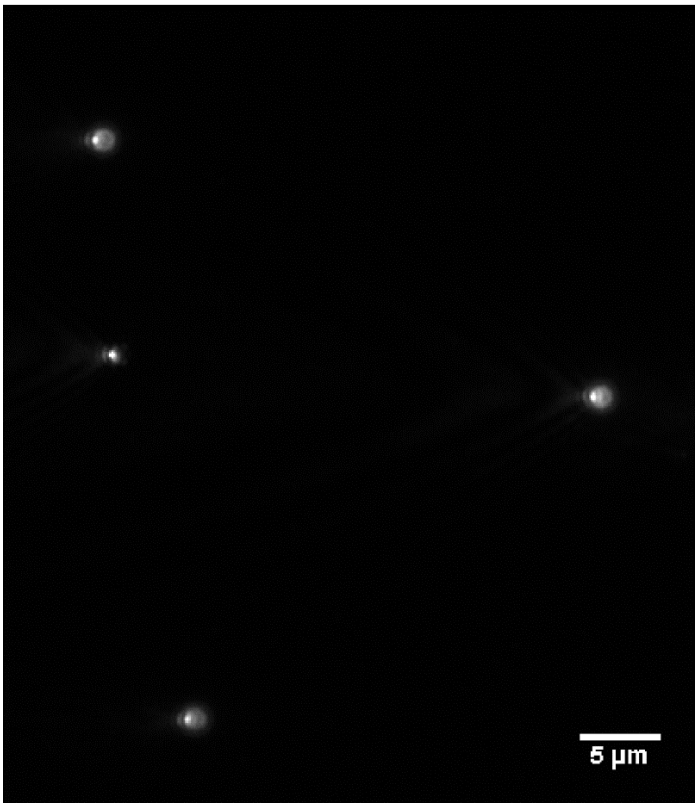

Figure 25. Magnetic beads confined to imaging surface. *1 µm diameter magnetic beads were confined within the TIRF imaging volume by a perpendicular magnetic positioned above the microscope sample stage.*

A cylindrical, neodymium magnet (N 52 cylindrical magnet, K&J Magnetics, 0.25" dia. x 1.5") was used. The magnet's cross section was comparable to the opening of the objective lens and was mounted within a 3D printed magnet holder. The magnet holder was attached to a XYZ translation stage (Thorlabs) which allowed precise adjustment of the magnet's position and pitch relative to the sample (**Figure 26**).

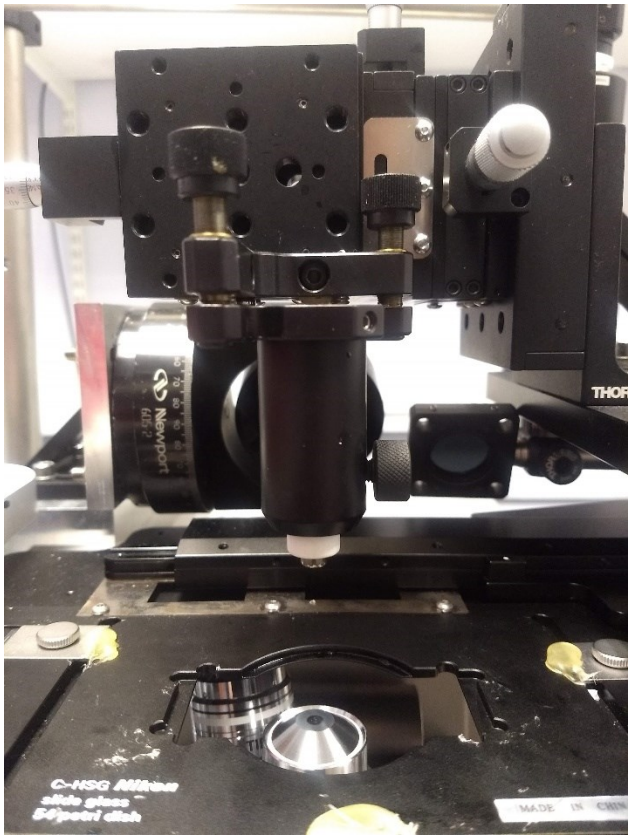

Figure 26. Magnet mounted to translation stage above microscope stage. *A neodymium magnet is suspended above the objective lens. An adjustable mirror mount allows the pitch of the magnet to be changed. The mirror mount is attached to a XYZ-axis translation stage.*

2.4.9 Fluorescence Recovery After Photobleaching (FRAP)

The capability to perform Fluorescence Recovery After Photobleaching (FRAP) experiments was added to the microscope setup. FRAP uses high intensity illumination to bleach a small patch within the field of view (Axelrod et al. 1976). As photobleached molecules within this region as replaced by fluorescent molecules, the bleached region recovers. This method can therefore measure the mobility of proteins and other molecules within the flow chamber. A free space 488 nm laser beam (Coherent) was focussed through an N-BK7 negative meniscus lens (Thorlabs) and aligned to the backport of the microscope base *via* a series of mirrors. The beam reflects up off a dichroic mirror (ZT488/640rpc, Thorlabs) held within a filter cube through the objective lens and incident upon the sample. By using a free space laser instead of a fibre coupled laser, the FRAP illumination has the higher power desirable for fast photobleaching of the sample (Weiss 2004). A diaphragm beam shutter (Thorlabs) was placed within the path of the laser and connected to a shutter controller (Thorlabs). The shutter was manually opened and closed using the controller for the desired bleaching time. The shutter controller accepts an external TTL signal, allowing it to be automated by connecting an external driver. Due to budget constraints, a TTL signal from a separate shutter driver

was not used, and the shutter was instead engaged/disengaged using the power button on the controller body.

2.5 Hardware alignment and optimisation

2.5.1 Calculating the TIRF Angle and Collimator Distance

TIRF is only achieved when the beam angle of incidence to the sample is greater than that of the critical angle of incidence. Total internal reflection occurs at the boundary between the high refractive index quartz slide and the sample. The equation below was used to calculate the critical angle for our setup:

$$\sin \theta_c = \frac{n_2}{n_1}$$

Where n_2 = 1.40 (refractive index of quartz) and n_1 = 1.33 (refractive index of water) and θ_c is the critical angle. When n_1 = 1.46 (refractive index of quartz) and n_2 = 1.33 (refractive index of water), the critical angle is calculated at θ_c = 65.6°. This meant that the collimator should be angled at least 25° from the horizontal for TIRF to occur.

Several incident angles were tested to find the maximum signal to background ratio (SBR) that could be achieved when viewing fluorescent beads.

$$SBR = \frac{Signal}{Background}$$

Where the signal of the bead was defined as the brightest point along a line profile of an individual bead and the background was the area directly adjacent to the bead. The mean SBR of fluorescent beads at the centre of the field of view was measured using each collimator angle (**Figure 27**). The highest SBR was obtained when the collimator was at an angle of 20° from the horizontal and positioned midway along its platform (position 3 in **Figure 28**). The SBR increased as the angle of the collimator approached 20°, contrasting my expectation that lower angles would show the greatest reduction in background intensity. Angles beyond 20° (data not shown) caused beads floating within the flow cell to be visible, indicating the microscope was no longer imaging in TIRF.

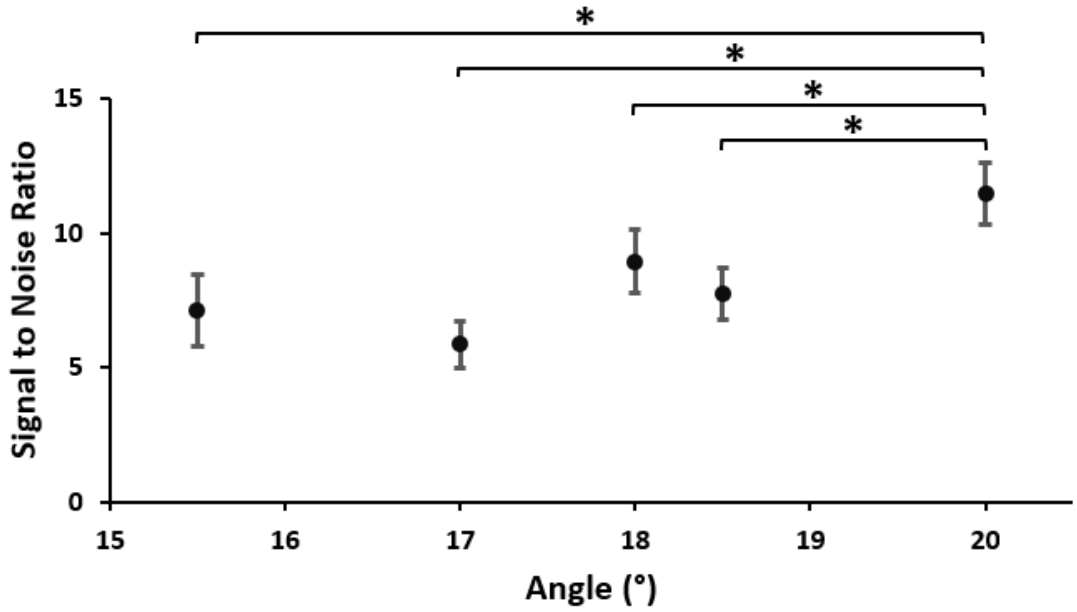

Figure 27. Effect of collimator angle on signal to background ratio. *Fluorescent beads were imaged using various collimator angles. Laser power was kept constant at 10 mW and exposure time of 100 ms. Each signal was the average of 5 beads at the centre of the field of view. Noise values were averaged over multiple 10x10 pixel areas without beads. Statistical significance determined via unpaired t-test comparing signal to background using each collimator angle; asterisk indicates P < 0.05.*

The distance between the centre of the collimator and microscope objective could be varied by positioning the collimator at different locations along its platform. This distance needed to be optimised to provide the highest SBR over the field of view. We measured the SBR of fluorescent beads at various collimator distances (**Figure 28**). Bead and background intensities were taken from both the centre and edge of the field of view to determine the uniformity of TIRF illumination field and bead SBR across the entire visible area.

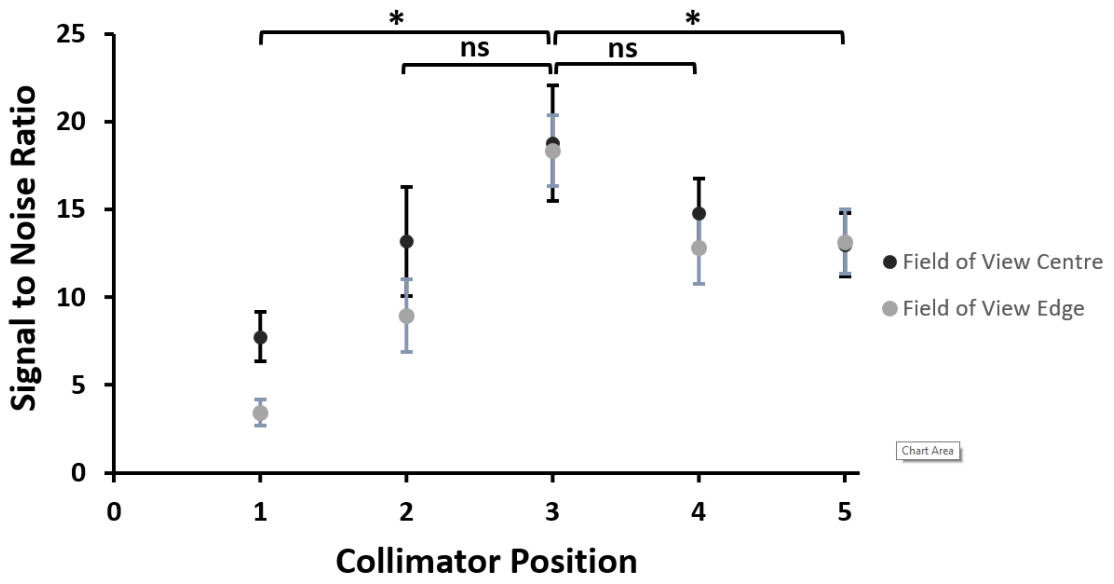

***Figure 28. Effect of collimator-stage distance on signal to background ratio**. Fluorescent beads were imaged using various collimator-stage distances by placing the collimator at approximately 1-inch increments along its mounting platform. Collimator positions are denoted 1-5 where 1 is the closest and 5 is the furthest from the stage. Laser power was kept constant at 8 mW and exposure time of 100 ms. Each signal was the average of 5 beads at the centre (blue) or near the edge of the field of view (grey). Noise values were averaged over multiple 10x10 pixel areas absent of beads. Statistical significance determined via unpaired t-test comparing signal to background using each collimator angle; asterisk indicates $P < 0.05$; ns indicates $P > 0.05$.*

Collimator-stage distance not only determined maximum SBR, but also uniformity of illumination across the field of view. This was due to the divergence of the laser beam exiting the collimator. This was seen at the shortest collimator-stage distance where beads at the centre of the field of view had a significantly higher SBR than beads at the edge. Collimator position 3 provided the highest SBR for all beads in addition to the greatest uniformity of SBR over the entire field of view. This means similar SBR for beads regardless of their location within the field of view, providing the ability to use the entire field of view without degradation towards the edges of the image.

These results determined the best angle and position to set the collimator (20° from horizontal; notch 3) to maximise SBR. We therefore used these collimator settings for the entirety of this project.

2.5.2 Optimising FRAP spot size

Before it could be used in any experiments, the FRAP laser profile had to be aligned and optimised. An ideal FRAP spot has a perfectly circular profile with a wide, central intensity peak. Our FRAP laser prior to any modifications had a very slim, gaussian profile (FWHM = 50 pixels) when incident on the sample. The profile was already circular and centralised in the camera's field of view, meaning that the laser path was correctly travelling straight up out of the objective. The laser spot size was expanded to create a wider and more even illumination profile on the flowcell surface whilst maintaining the angle at which it entered the objective. This was achieved by placing a focusing lens

within the excitation filter slot of the filter cube to change the focus distance. Two lenses, a planoconcave (LC1715-A, Thorlabs, f = -50.0 mm) and a N-BK7 negative meniscus lens (LF1988-A, Thorlabs, f =-500 mm) were tested to compare their illumination profiles on the flowcell surface (**Figure 29**). The negative meniscus lens was found to widen the laser profile compared to when no lens was present whilst maintaining a steep drop off in intensity at the profile edges. The plano-concave lens increased the profile diameter even further but with a shallower intensity drop off. The meniscus lens was therefore selected to expand the photobleaching laser profile for the FRAP experiments during the project.

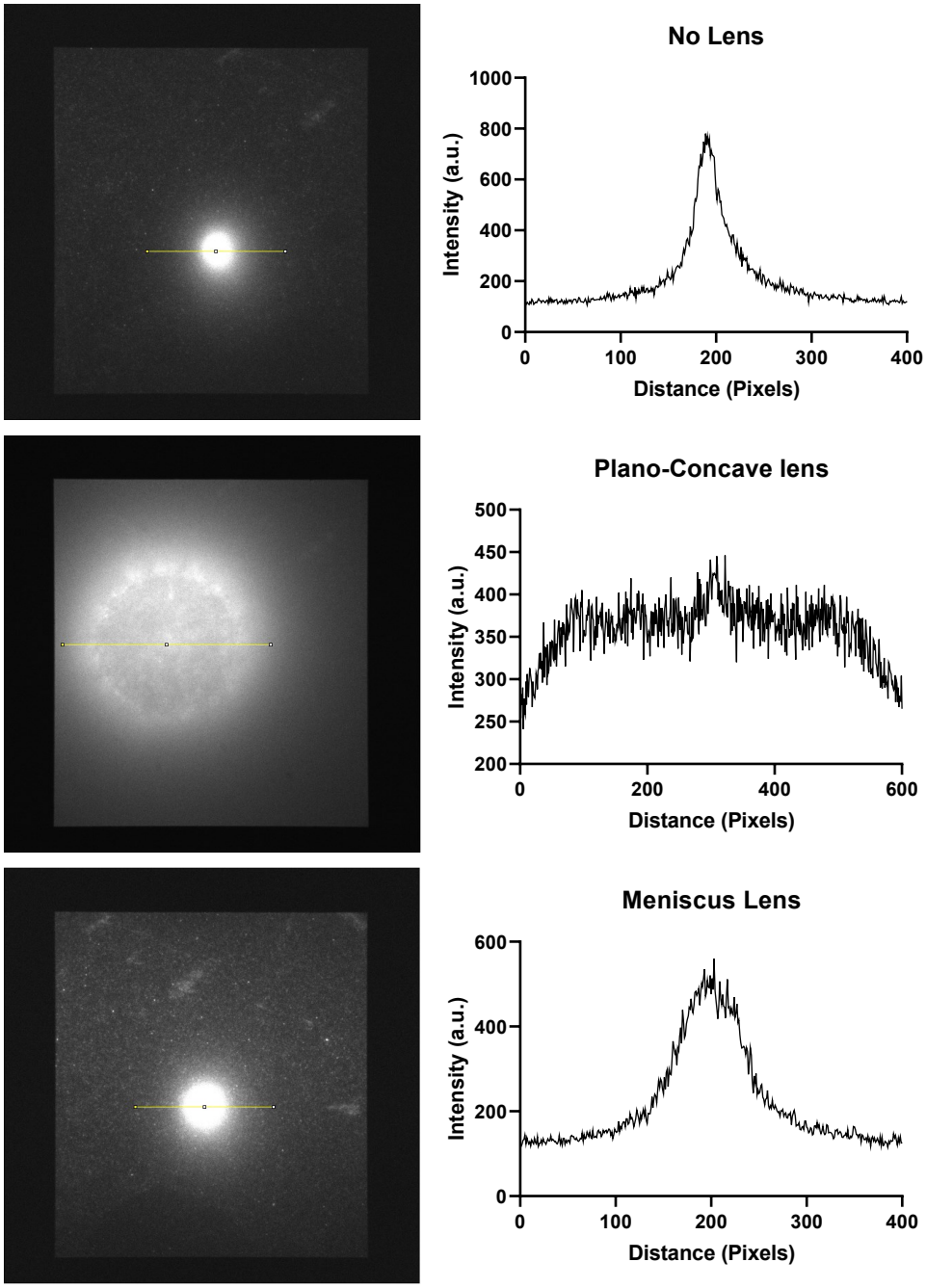

Figure 29. The effect of different lenses on FRAP laser profile. *FRAP laser spots incident on the surface of a slide were imaged. Spot size and shape was modified by lenses placed within the excitation slot of a filter cube. Each laser spot was imaged using a Prime 95B camera. All FRAP laser spot profiles were created using 1 mW laser power. Illumination profile graphs were created using ImageJ by measuring the intensity across the waist of each laser spot.*

2.5.3 Reducing background from excitation light with a notch filter

Although prism TIRF benefits from a reduced amount of excitation light entering the emission pathway when compared to objective TIRF, it is still helpful to use notch filters to reject any excitation wavelengths which still manage to enter the objective. The Thorlabs notch filters in our possession were too thick (3.5 mm) to be housed within any of the available filter cubes, meaning there was nowhere for the notch filters to be placed without the purchasing of additional

components. On the body of the Nikon Ti, there was an unused slot situated directly below the filter turret. A tray holding the notch filters could slide into this slot, making it possible to place the notch filter into the emission path. I designed and 3D printed a filter tray which could house the notch filter and fit securely within the empty slot. A small indent was made on the exterior of the filter tray causing it to click into place when the centre of the notch filter was positioned directly below the objective lens. The presence of a notch filter within the emission path removed any excitation light should it enter the objective lens during imaging.

2.5.4 Dual inlet flow cells

Although single inlet flow cells were suitable for experiments involving a single infusion stage, they posed a problem when instantaneous switching between samples was desired. For example, later experiments within the project would measure the binding and dissociation rates of ParA2-GFP from a DNA-coated surface. A single inlet flow cell was only capable of infusing a binding sample or a wash buffer, and it would be impossible to capture both within a single acquisition. This is due to the lag time present from the displacement of old sample between the inlet port and objective which must occur when switching to a new sample. Removal of the tubing from the inlet ports when switching samples also introduced air bubbles into the flow cell on many occasions. Acquisition would also need to be paused whilst switching between samples and buffers. This meant that the association of a protein when infused into the flow cell and its subsequent dissociation when washed away with a buffer solution would be impossible to capture within a continuous image sequence.

Fast switching between samples was achieved through laminar flow steering (Tan et al. 2007; Allen et al. 2010). This method takes advantage of a phenomenon that occurs when two samples flow alongside each other, establishing a laminar boundary between them. Neither solution can cross this boundary, preventing any mixing of the two samples. The position of this boundary can be shifted side to side by modifying the ratio of flowrates between the two samples. For example, when sample **A** is flowed alongside sample **B** at a 10:1 flowrate ratio, the boundary was positioned so **A** would occupy the majority of the flow chamber, with **B** flowing alongside it within a much smaller volume. Sudden switching of the flowrates between the two pumps would then cause the laminar boundary to instantly shift, making **B** now dominant within the flow chamber. By imaging at the location of this boundary shift, an instantaneous change of samples is observed within the field of view.

Laminar flow steering was achieved by creating dual inlet flow cells (Vecchiarelli et al. 2013) (**Figure 30**). These flow cells were very similar to our previous flow cells except for an extra inlet hole

present in the quartz slide. The double-sided tape was cut with a new design which created a Y shaped chamber. The two inlets were connected to a syringe mounted within its own syringe pump. The pumps were simultaneously controlled *via* the microscope computer, connected to the pumps through an RS232 ethernet cable. Sending computer instructions to initiate and control the individual flowrates of each pump was essential for setting up laminar flow switching as it ensured that commands are given to both pumps simultaneously.

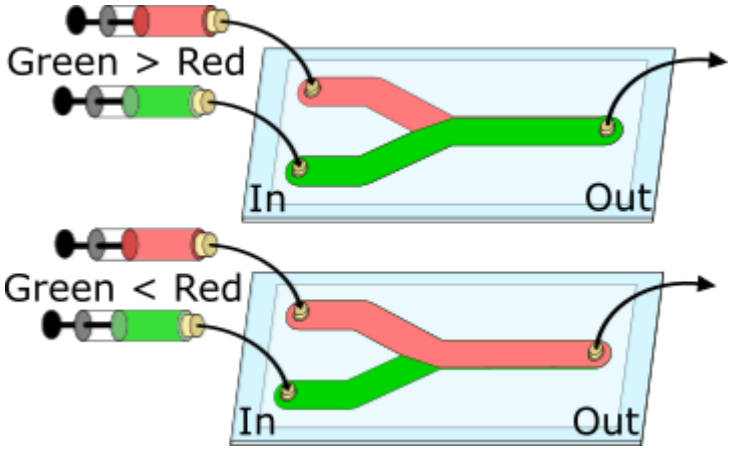

Figure 30. Laminar flow switching using two-inlet flow cell. *Varying the ratio of flowrates between two solutions shifts the laminar flow boundary within the flow chamber. When the flowrate of the green sample is greater than that of the red sample* ***(Top)****, most of the chamber will be occupied by the green sample. After switching flow rates so the red sample now has the greater rate (****Bottom)****, the red sample now occupies the most space. When the objective is located at the junction between the two flow cell inputs, instantaneous switching of the solution occurs within the microscope's field of view.*

2.6 Discussion

In this chapter, we have described the process of building and optimising a TIRF microscope capable of multi-colour imaging. Due to the unique challenges associated with the study of bacterial chromosome segregation in a cell free system, no commercially available microscopes were suitable for our experiments. We therefore opted for a custom-built microscope. The majority of design decisions were made with the aim to visualise an *in vitro* reconstitution of the ParABS system using our microscope setup and influenced by the microscope used in the reconstitutions of the P1 and F-plasmid partition systems (Hwang et al. 2013; Vecchiarelli et al. 2013).

The process of building the microscope began by selecting the necessary hardware for its construction. It then progressed to the fine alignment and optimisation of each component to gain the best performance from the system. Additional components were added, and the final design and build is shown in **Figure 31**.

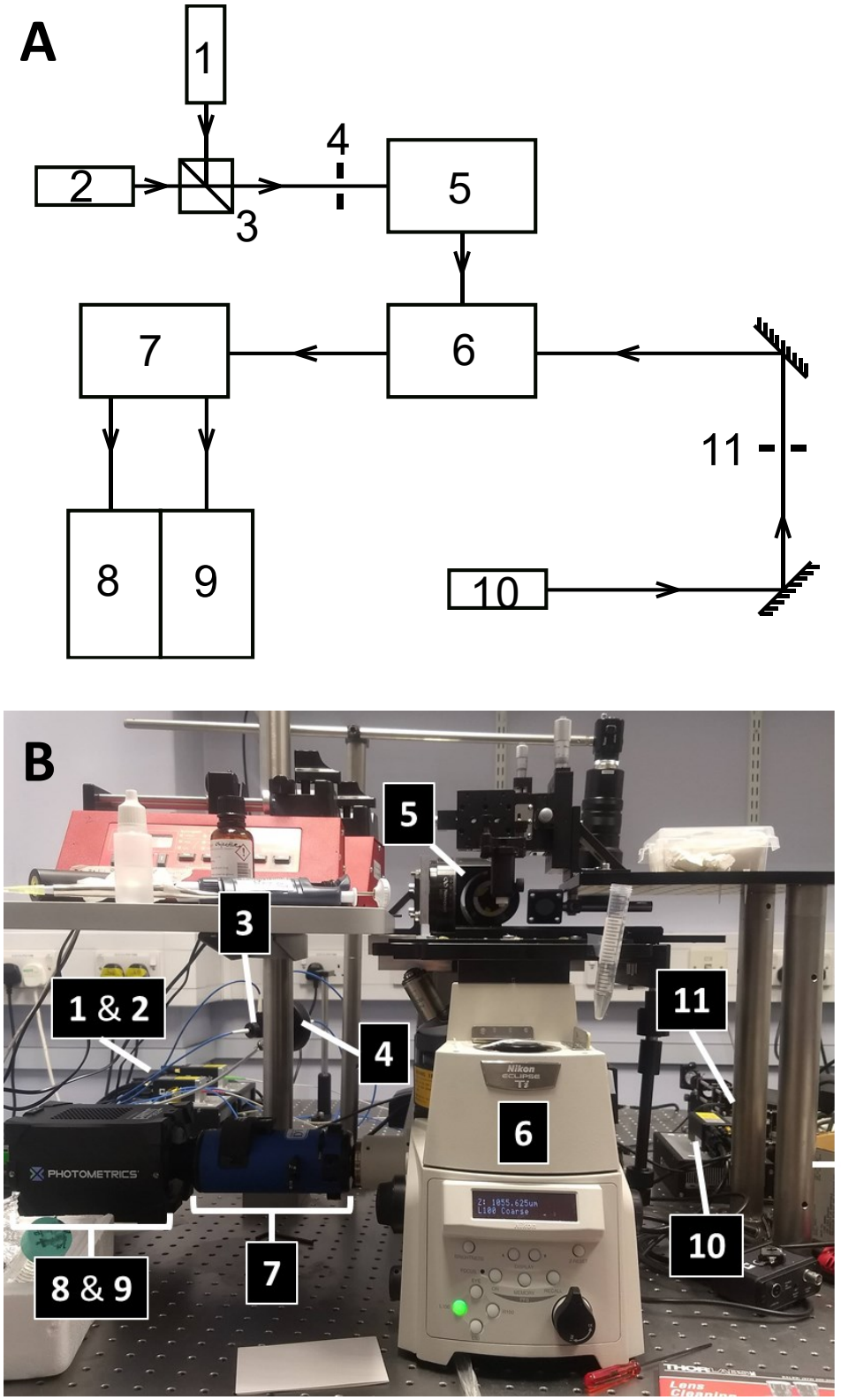

***Figure 31*. (A) Final schematic and (B) build of TIRF microscope.** *Original TIRF design was expanded upon and components finalised. (1) 488 nm, fibre coupled laser (Cobolt); (2) 633 nm fibre coupled laser (Cobolt); (3) Fibre coupled laser combiner; (4) Blade shutter (Uniblitz); (5) Collimator mounted within multi-axis optical fibre mount; (6) Microscope body (Nikon Ti Eclipse); (7) emission splitter (Dual-View; Photometrics); (8 & 9) Separate green and red emission channels on single sCMOS detector (Prime 95B; Photometrics); (10) 488 nm free space FRAP laser (Coherent); (11) Diaphragm shutter (Thorlabs).*

2.6.1 Optimising signal to background performance

By modifying the angle of the imaging laser and the distance from which it is emitted from the sample, the signal to background (SBR) of fluorescent beads was maximised (**Figure 27** and **Figure 28**). This optimisation considered solely the effect of changing the properties of the TIRF illumination field. Fluorophore SBR is also affected by many other factors such as temperature, sample preparation and buffer conditions. It was therefore important that these initial settings were considered as a start point and parameters were adjusted accordingly when imaging.

2.6.2 Sample switching *via* laminar flow steering

Microfluidic flow cells were designed, fabricated and optimised for TIRF microscopy. The original single-inlet flow cells were quickly replaced with dual-inlet versions to allow instantaneous switching of samples *via* laminar flow switching. This technique allowed changing of the sample conditions during acquisitions with minimal physical manipulation of the sample. The ability to quickly change between solutions made the setup suitable for a broad range of applications in which rapid exchange of the chemical environment surrounding stationary molecules is desired.

2.6.3 Additional components and capabilities

Many of the components added to the microscope were not part of the original design. This includes a notch filter holder to reduce excitation light intensity at the detector and an illumination shutter which reduces unnecessary illumination of the sample. The illumination shutter in particular made the microscope viable for live cell imaging, due to minimising the effects of phototoxicity over long periods of imaging (Icha et al. 2017). Although *in vivo* imaging is out of the scope of this project, it could prove useful in future work investigating chromosome segregation in live cells.

The capabilities of our setup were extended with the inclusion of a FRAP system. The profile of the FRAP laser was optimised to the field of view of the camera using a meniscus lens within the filter cube (**Figure 29**). Due to the absence of a dedicated shutter driver, we rely on manual operation of the FRAP shutter controller. For our experiments, the timing discrepancies introduced by manual control were negligible. However, if greater precision of the FRAP pulse duration is desired, the addition of a FRAP shutter driver would make a suitable upgrade to the setup. Further optimisation would still need to take place to work out the ideal laser intensity for bleaching of each fluorophore. The bleaching time should be kept minimal for accurate estimations of recovery times to be made. These optimisations however would only be possible to be carried out once imaging of our fluorophore tagged proteins had started.

Chapter 3

Characterising *Vibrio cholerae* chromosome II ParA2 interactions on DNA carpet using TIRFM

Parts of this chapter have been included within a manuscript in preparation.

Expression and purification of ParA and ParB proteins was performed by Satpal Choda, Alexandra Parker and Sveta Sedeinikova. I performed all other experiments within this chapter.

3.1 Introduction

Prior to cell division, high copy DNA molecules are evenly distributed throughout the cell, guaranteeing that newly formed daughter cells will receive at least a single copy (Wang 2017). Low copy DNA molecules, such as chromosomes and single-copy plasmids, however, must be positioned on either side of the cell prior to septum formation to guarantee that each daughter cell inherits a copy. In fact, due to their size, chromosomes will deny septum formation if they are not clear of the mid cell, preventing cell division (Bernard et al. 2010; Cambridge et al. 2014). This positioning cannot be reliably achieved through diffusion alone but by directed transport of these molecules. Within bacterial cells, molecular motors transport cargo at speeds exceeding those permitted by diffusion alone. These motors consume energy, typically ATP, to produce the mechanical force required to power to movement of their cargo.

Most current knowledge of how ParA interacts with DNA and different components of the ParABS system has been derived from studies of plasmid ParA. Studies of ParA from plasmid positioning *par* systems suggest that the ATPase binds the nucleoid non-specifically when in its ATP-activated state (Vecchiarelli et al. 2010). To visualise ParA-DNA interactions, a method was required to tether DNA molecules to the inner surface of the flowcells. Previous studies of ParA from low-copy plasmids used individual molecules of λ DNA to coat the surface of flowcells and visualised protein binding through TIRFM (Vecchiarelli et al. 2010; Han and Mizuuchi 2010). Later experiments mimicked the nucleoid surface by forming a uniform layer of DNA on the imaging surface, termed a DNA carpet (Hwang et al. 2013; Vecchiarelli et al. 2013; Vecchiarelli, Neuman, et al. 2014). From these experiments arose a diffusion ratchet model of how ParA drives the segregation of plasmids, discussed within Chapter 1, part 1.4 of this thesis. The basis of this model is the formation of protein concentration gradients on the surface of the nucleoid. This gradient is formed around the point of nucleoid-plasmid attachment due to ParB-*parS* complexes triggering the hydrolysis of nearby ParA-ATP to ParA-ADP. ParA which undergoes this hydrolysis is no longer in its DNA-binding configuration and so quickly detaches. Upon clearing its vicinity of ParA, the plasmid then proceeds along the surface of the nucleoid to denser areas of the ATPase. The existence of these protein gradients for plasmid systems is due to a time delay between ATP association and the conformational change which allows ParA to bind DNA. This time delay reduces the rate of ParA rebinding back to the cleared area around the plasmid, causing the plasmid to translocate to denser regions of ParA.

ParA2 is the ATPase component of the *par* system which regulates the segregation of the smaller chromosome of *V. cholerae,* chromosome II. As an ATPase, it is a molecular motor, hydrolysing ATP to produce the driving force of the segregation mechanism. Although ParA2 is key to creating the

forces required for directed segregation of chromosome II, our understanding of the exact mechanism that generates these forces is limited. The segregation pattern of chromosome II closely resembles that of single-copy plasmids, symmetrically segregating from mid cell towards the quarter cell positions. Within the diffusion-ratchet mechanism, the DNA-binding characteristic of ParA is integral to its role in the generation of mechanical force. ParA2 is known to bind nsDNA (Hui et al. 2010), but the rate of binding and dissociation have not yet been accurately measured. A time delay between ATP association and a DNA binding state is also yet to be characterised for ParA2 or any other chromosomal ParA ATPase. This chapter aims to directly visualise ParA2 binding to a DNA carpet to better understand this important interaction. By doing this, I hope to reveal the differences and similarities between the force generation mechanisms of plasmid and chromosomal ParA. If a time delay and a nucleotide dependent binding switch exists for ParA2, it would suggest that chromosomes, like plasmids, are able to use protein gradients to drive the directed motion seen in segregation (Fogel and Waldor 2005; Fiebig et al. 2006).

3.2 Materials and Methods

Note: Expression and purification of ParA and ParB proteins was performed by Satpal Choda, Alexandra Parker and Sveta Sedeinikova.

3.2.1 TIRF microscopy

Prism-TIRFM was performed using an Eclipse Ti microscope (Nikon) with a PlanApo 100 x NA = 1.45 oil-immersion objective (Nikon). Fluorescence images were captured using a sCMOS camera (Prime 95B, Photometrics). Typical camera settings used were: exposure time 100 ms; frame rate 1 Hz; 16-bit depth. The camera bias of 100 grey units was subtracted from measured intensities. This bias is an offset in the minimum threshold of the camera which prevents negative intenisty readings arising from natural fluctuations in read noise. For experiments involving ParA2-GFP interactions with DNA-carpets, sample excitation was provided by a 488 nm fibre coupled laser (Cobolt). Laser power was calibrated and adjusted to a typical level of 100 µW. The excitation laser line was removed with a notch filter centred around the 488 nm wavelength (NF488-15, Thorlabs) and a bandpass filter (Chroma) was used to clean up emission light. Measured intensity of bound ParA2-GFP was taken from the centre of the illumination profile. Micro-manager open software was used for camera control and image acquisition. ImageJ was used for image analysis. Control over syringe pumps (WPI) was *via* open software, RealTerm. ParA2-GFP fluorescence measurements were background-subtracted and analysed using GraphPad Prism 7. Binding curves were fitted with a “one phase association” model whilst decay curves were fitted with a “two phase decay” model. Both models are built-in to Prism.

3.2.2 Flow cell fabrication

Predrilled quartz slides (Esco Products) were washed overnight in concentrated sulphuric acid (Fisher). The following day, Milli-Q water was used to thoroughly rinse the slides. Slides were then partially dried under a stream of nitrogen to remove larger water droplets prior to air drying at 60 °C. Air plasma cleaning the dry slides for 15 min (Diener Electronic) was used to remove any residual contaminants. 25 µm thick, double sided adhesive tape (3M) was laser cut with the desired channel profile. This was either a single channel or, for dual inlet flow cells, a Y-shaped channel (Vecchiarelli et al. 2013) to enable laminar flow steering. Microfluidic flow cells were fabricated by sandwiching the cut double-sided adhesive tape between a cleaned, quartz slide and a #1.5 microscope coverslip (Marienfeld). Flow cells were then clamped between two microscope slides using metal clips and placed in an oven at 120 °C for 2 hr. Once the adhesive had melted (observed as turning transparent) the microscope slides and clamping metal clips were removed. Nano ports (UpChurch) were positioned atop each hole and adhered using UV glue (Norland), cured with UV illumination for 15 min. Completed flow cells were stored in a microscope slide box.

3.2.3 Biotinylated liposomes

Stock DOPC (10 mg/mL) (Avanti) and biotin-PE (10 mg/mL) (Avanti) were removed from -20 °C and thawed at room temperature. 247.5 µL of DOPC was mixed with 2.5 µL biotin-PE within a glass tube. This was completed for 4 tubes. Chloroform was lyophilized from the lipid solution by running tubes in speed vacuum for 1.5 hr at 50 °C. Once chloroform removal was complete, lipids were resuspended in 250 µL TN100 buffer overnight in the dark. The next day, lipids were vortex for 1 min and transferred to 4 Eppendorf tubes. At this point, the lipids mixtures are turbid. Each tube was sonicated for 3 min in a 10 s on/10 s off fashion until the lipid mixtures were clear. Tubes were centrifuged at 12,000 g for 2 min to pellet centrifuge probe residue. Lipids were then filtered through Proteus Mini Clarification 0.22 µm Spin Columns for 1 min. Lipids were transferred to glass tubes, argon blown into the tubes and sealed tightly. Lipids were stored at 4 °C for maximum 1 month.

3.2.4 Purification of sonicated salmon sperm DNA

Salmon sperm DNA (Sigma) was prepared to 10 mg/mL in TE buffer and aliquoted into 250 µL volumes. Samples were probe sonicated on and off for 10 s intervals for a total time of 1 min and 45 s. Tubes were centrifuged at 12,000 g for 3 min to pellet centrifuge probe residue. Supernatant was transferred to another Eppendorf. 40 µL sodium acetate pH 5.2 was added to the DNA along with 1 mL of ice cold 100% ethanol. The mixture was vortexed for 2 min and incubated for 1 hr at -20 °C. Once incubation time had elapsed, the mixture was centrifuged at 12,000 g for 30 min at 4 °C

to pellet DNA. Supernatant was discarded and 200 µL ice cold 70% ethanol added to the pellet. Mixture was centrifuged at 12,000 g for 10 min at 4 °C. Supernatant was removed and DNA pellet was air dried on a 30 °C heat block for 20 min. Pellet was resuspended in TE buffer and stored at -20 °C.

3.2.5 Biotinylated DNA

Sonicated salmon sperm DNA (1 mg/mL) was added to reaction mixture (1x TdT Buffer, 0.25 mM $CoCl_2$, 40 µM biotin-14-dCTP (Jena), 0.6 u/µL TdT) and incubated for 30 min in a water bath at 37 °C. Reaction was terminated after 30 min had elapsed by heating mixture to 70 °C for 10 min on a heat block. DNA was eluted by spinning in S200 micro spin columns (Sigma) for 2 min. 20 µL sodium acetate and 550 µL 100% ice cold ethanol was added to each 200 µL preparation of DNA. Mixture was incubated for 1 hr at -20 °C and then centrifuged for 1 hr at 4 °C. Supernatant was removed and the DNA washed with 200 µL 70% ethanol. Mixture was again centrifuged for 5 min at 12,000 g, after which the supernatant was removed. Remaining ethanol was evaporated by placing sample on 30 °C heat block for 20 min. DNA pellets were dissolved in 20 µL TE and stored at -20 °C.

3.2.6 DNA carpet preparation

Liposomes (99% DOPC, 1% Biotin-PE) created through probe sonication were manually injected into an empty flow cell and left to form a lipid bilayer over 1 hr. Neutravidin (1 mg/mL) (Fisher) was subsequently infused into the flow cell at a rate of 50 µL/min and left to bind the exposed biotin molecules within the bilayer for 1 hr. Sonicated salmon sperm DNA (1 kb) was biotinylated at both ends and infused into the flow cell. The biotinylated DNA was left overnight at 4 °C to bind exposed neutravidin, forming a DNA carpet. The following day, the DNA-carpet was washed with 500 µl Par Buffer containing 1 mg/mL α-casein (Sigma) and left to incubate on the benchtop for 1 hr. The presence of α-casein was to block any exposed glass surface where the bilayer is not present. A subsequent wash with 500 µl Par Buffer containing 0.1 mg/mL α-casein was required before any experimental runs.

3.2.7 ParA2-GFP Binding and Dissociation

ParA2-GFP (10 µM) was preincubated in Par Buffer [50 mM Tris (pH 7.5), 100 mM NaCl, 5 mM $MgCl_2$, 10% (vol/vol) glycerol, 1 mM DTT, 0.1 mg/mL α-casein] with 1 mM ATP (or given alternative nucleotide). The sample was incubated for 30 min at 25 °C. The sample was then diluted to final concentration, loaded into a 1 mL syringe (BD) and attached to one of two inlets of a Y-channel, DNA-carpeted flow cell. A separate syringe was loaded with wash buffer (Par Buffer with no ParA2-GFP) and attached to the remaining inlet. Sample and wash buffer were infused simultaneously into a DNA-carpeted flow cell at 20 µl/min and 1 µl/min respectively during the binding portion. After

380 s, sample and wash buffer flow rates were switched to 1 µl/min and 20 µl/min respectively, initiating the dissociation process. Imaging close to the point of flow convergence minimised the impact of protein rebinding the DNA-carpet.

Additional dissociation experiments involved wash buffer containing additional cofactors (100 µg/mL sonicated salmon sperm DNA and/or 2 µM ParB2). These experiments all used ParA2-GFP (10 µM) which had been preincubated with ATP (1 mM) for 30 min at 25 °C. Samples were diluted to a final concentration of 1 µM and infused into a DNA carpeted flow cell in the same manner as the above. After the intensity of the carpet reached a steady state, flow was switched to a wash buffer containing an additional cofactor at a rate of 20 µl/min.

3.2.8 ATP Start

Separate solutions of ParA2-GFP (2 µM) and ATP (2 mM) were prepared in Par Buffer. The two solutions were loaded into 1 mL syringes and attached to a micro-static T-mixer (IDEX). The T-mixer was attached to the outlet port of a Y-channel, DNA-carpeted flow cell. Both syringes were set to pump at a rate of 10 µl/min, resulting in a final rate of 20 µl/min entering the flow cell. The surface of the DNA-carpet was monitored using TIRF microscopy. Intensity of the DNA-carpet was measured close to the inlet port to minimise the time between the point of solution mixing and image capture.

3.2.9 FRAP

A free-space 488 nm laser (Coherent) was directed up through 100x objective lens *via* the back port of the microscope. A meniscus lens, f = -500 mm, (Thorlabs) was positioned in the excitation filter slot of the filter cube (Chroma) to expand and focus the FRAP beam. A dichroic mirror (ZT488/640rpc, Chroma) was positioned inside the filter cube to direct a free 488 nm free laser (Coherent) up towards through the objective lens (Nikon).

ParA2-GFP was preincubated at 10 µM in the presence of 2 mM ATP for 15 min at 25 °C. The protein sample was infused into a DNA carpeted flow cell and visualised using TIRF microscopy [exposure = 100 ms, 1 frame per second]. A diaphragm shutter (Thorlabs) placed within the path of the FRAP beam was opened/closed with a manual shutter controller (Thorlabs). A laser power of 35 mW was used to bleach ParA2-GFP bound to the DNA carpet to around 50% of its initial intensity. Continued recording of the DNA carpet was maintained until a steady state of ParA2-GFP had recovered to the bleached area. Analysis of FRAP recovery curves was carried out in OriginPro.

3.3 Results

3.3.1 DNA carpet setup as a method to simulate conditions during chromosome segregation

In our experiments, a DNA carpet was formed within a flowcell in three steps (**Figure 32**). First, a supported lipid bilayer was formed *via* vesicle fusion of biotinylated, small unilamellar vesicles (SUVs). Neutravidin is then infused into the flowcell, binding the exposed biotin present within the bilayer. Sonicated salmon sperm DNA (1 kb/300 nm) which has been biotinylated at either end is then layered on top of the lipid layer. The biotin ends of the DNA bind to the neutravidin sites, coating the entire bilayer with a near uniform blanket layer of nsDNA. Given a typical persistence length of double-stranded DNA of approximately 50 nm (Mitchell et al. 2017), biotinylated DNA measuring 300 nm could potentially bind twice to the same Neutravidin molecule.

The DNA carpet used in conjunction with TIRF provided a robust method to measure the association and dissociation rates of fluorescent molecules to nsDNA. By measuring the intensity of the DNA carpet, the amount of bound fluorescent molecules was estimated. The binding and dissociation of these fluorescent molecules is reflected respectively by the increase and decrease in the measured carpet intensity.

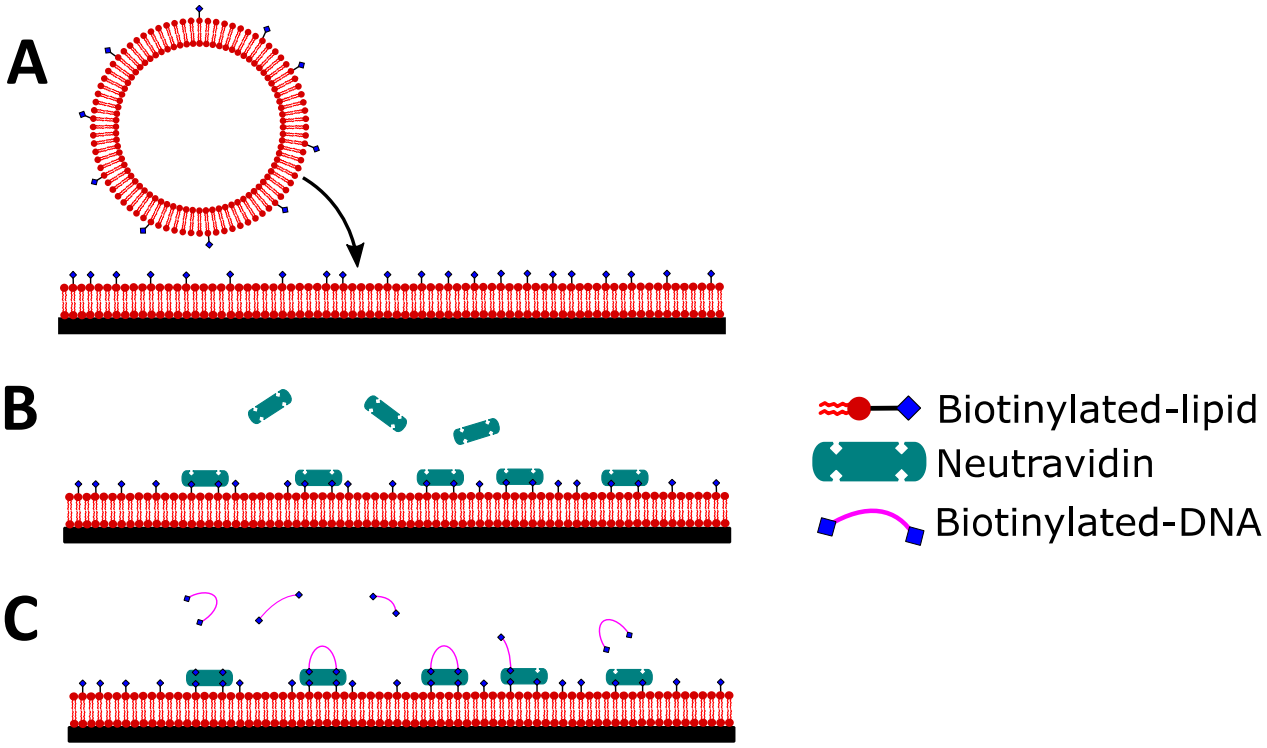

Figure 32. Formation of DNA carpet within flowcell. *(A) Biotinylated liposomes form a supported bilayer on a glass surface through vesicle fusion. (B) Neutravidin binds biotin on bilayer. (C) Biotinylated DNA (1 kb/300 nm in length) binds to exposed Neutravidin sites, coating the surface of the supported bilayer, forming DNA carpet.*

3.3.2 ATP-dependency of ParA2 for non-specific DNA binding

First, the role of ParA2-nucleotide binding was studied. Previous studies using electron microscopy (EM) showed evidence of ParA2 forming filaments on DNA in the presence of ATP, ADP and no nucleotide (Hui et al. 2010), but role of these filaments during chromosome segregation is unknown. The importance of ATP in ParA2-DNA binding was confirmed using TIRF microscopy to visualise the binding of ParA2-GFP to non-specific DNA within a DNA carpeted flowcell. ParA2-GFP (10 μM) was preincubated with various nucleotides (1 μM) for 30 min. The sample was diluted down to its final concentration (1 μM) and infused into the flowcell. ParA2-GFP that was preincubated with ATP displayed rapid binding to the DNA carpet upon infusion into the flowcell with a time constant τ=19 s, plateauing at a steady-state within 1 min (**Table 2**, **Figure 33**). This steady state intensity occurred without saturation of the DNA carpet, indicating that ParA2-GFP was simultaneously binding and dissociating from DNA. When incubated with no nucleotide, ParA2-GFP showed negligible binding to the DNA carpet. The same absence of binding was observed for ParA2-GFP preincubated with ADP. ParA2-GFP which was preincubated with ATPγS showed considerable DNA-binding activity (time constant of τ=65 s), although at a slower rate than seen with ATP (**Table 2**). The steady-state level of bound ParA2-GFP was similar for both ATP and ATPγS. The dissociation of ParA2-GFP from the DNA carpet was triggered by switching flow to a wash buffer containing no protein. Upon switching to the wash, a rapid decay of ParA2-GFP from the carpet at a faster rate than the rate of binding was observed (**Table 2**). This indicated that ParA2-ATP binding to DNA is reversible. The dissociation rate of the ATPγS associated protein was considerably slower than for ATP (**Table 2**). These results suggest that although ATP hydrolysis is not a requirement for ParA2 to bind DNA, it does however increase the rate of ParA2 association and dissociation from DNA. The negligible binding of ParA2-ADP and ParA2 in the absence of a nucleotide contradicted results from previous electron microscopy studies (Hui et al. 2010). This was likely because of far higher concentration of nsDNA present within the DNA carpet compared to that used within the EM study. The conditions within the DNA carpeted flow cell better represented the physiological conditions found within the cell, and therefore suggest a more accurate picture of interactions which occur *in vivo* than the prior EM study.

Table 2. Binding and dissociation rates of ParA2-GFP on DNA carpet.

ParA2-GFP		1 µM (ATP)	500 nM (ATP)	250 nM (ATP)	1 µM (ATPγS)
	Binding				
K (s^{-1})		0.053 ± 0.006	0.051 ± 0.009	0.049 ± 0.011	0.016 ± 0.004
τ (s)		18.8 ± 1.9	20.0 ± 3.4	21.1 ± 4.4	64.5 ± 14.6
	Dissociation				
K_1 (s^{-1})		0.11 ± 0.04	0.17 ± 0.08	0.19 ± 0.12	0.015 ± 0.002
τ_1 (s)		10.0 ± 4.2	7.2 ± 4.5	7.0 ± 4.3	70.2 ± 9.7
K_2 (s^{-1})		0.0046 ± 0.0001	0.0048 ± 0.0001	0.0041 ± 0.0001	0.0016 ± 0.0002
τ_2 (s)		218 ± 6	208 ± 6	242 ± 6	627 ± 6
$\%_1$		78.6 ± 4.1	79.7 ± 5.0	83.2 ± 1.3	48.7 ± 3.4

K_1: Rate of fast decay species

K_2: Rate of slow decay species

τ_1: Time constant of fast decay species

τ_2: Time constant of slow decay species

$\%_1$: Fraction of decay due to fast decay species

p-value of approximately 0.5 was determined via unpaired T-test for ParA2-GFP binding and dissociating at different concentrations with ATP, meaning that the binding and dissociation rates are not significant from one another.

p-value of 0.02 was found between the ATP and ATPγS associated binding rates, meaning that they are significantly different.

Errors are calculated as ± standard deviation from at least 3 repeats. Intensities were background subtracted. The effect of photobleaching was removed by measuring the intensity of bound ParA2-GFP over a long exposure time, and compensating for this loss by subtracting this baseline from the measured intensities.

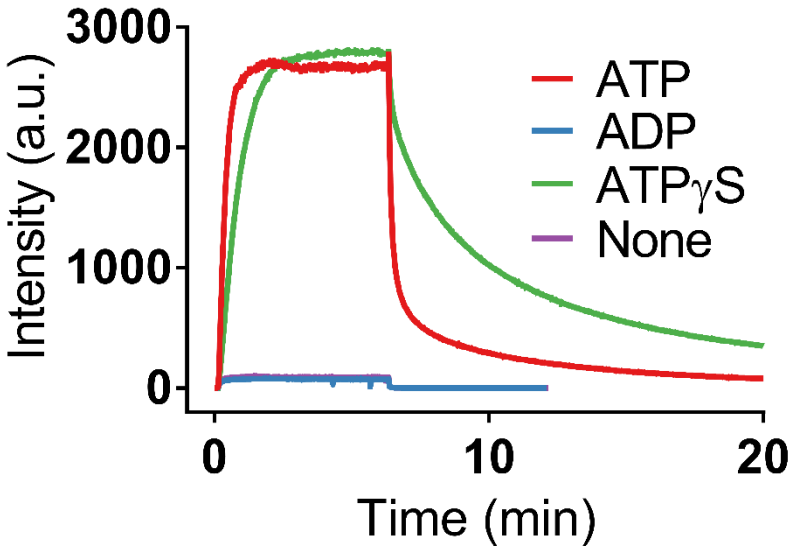

Figure 33. Binding and dissociation of ParA2-GFP on DNA carpet with different nucleotides. *10 µM ParA2-GFP was preincubated with ATP, ADP, ATPγS or with no nucleotide for 30 min. Samples were diluted to 1 µM and infused into a DNA carpeted flow cell for 380 s before switching to a wash buffer. Fluorescence intensity of the DNA carpet was measured over time. Both sample and wash buffer are infused at a rate of 20 µL/min. Trace for "None" is hidden by similar trace for "ADP". 3 repeats were performed and errors (**Table 2**) were calculated as ± standard deviation of these repeats.*

3.3.3 Impact of ParA2 concentration on non-specific DNA-binding

The effect that varying ParA2-GFP concentration has on its ability to bind nsDNA was then studied. Buffer containing different concentrations of ParA2-GFP was infused into a DNA-carpeted flow cell and TIRF was used to measure the fluorescence intensity of the DNA carpet. All sample concentrations exhibited rapid non-specific binding to the DNA carpet, with similar binding rates of 0.05 s^{-1} (**Table 2**, **Figure 34**). The steady state level of 500 nM ParA2-GFP was approximately double that of 250 nM. 1 µM ParA2-GFP showed the highest steady state level. Upon switching to a wash buffer, rapid dissociation occurred for all three concentrations of ParA2-GFP. The time taken for each sample concentration to reach background level was proportional to its steady state intensity. The measured dissociation rates for all three concentrations were significantly faster than those of plasmid ParAs (Vecchiarelli et al. 2010; Hwang et al. 2013). These fast dissociation rates may translate to fast dynamics and movement of ParA within the cell *in vivo*.

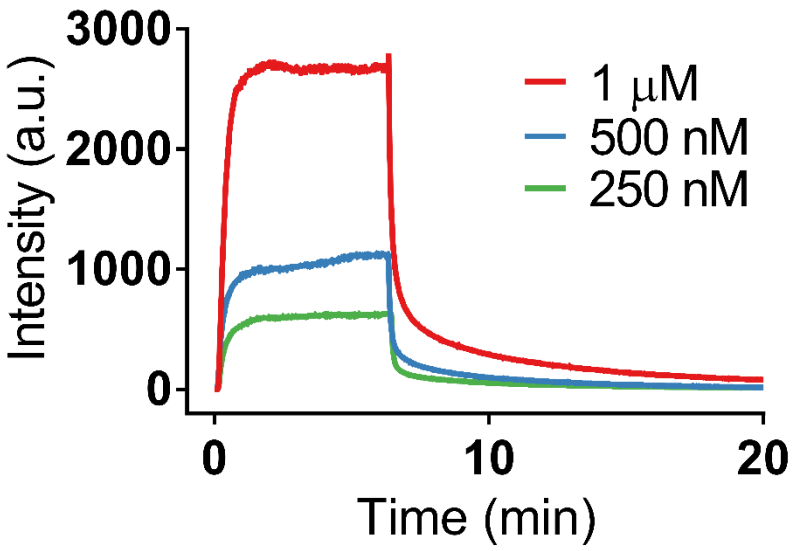

Figure 34. Binding and dissociation of ParA-GFP on DNA carpet at different concentrations. *ParA2-GFP (1 µM) was preincubated with ATP for 30 min at 25°C. Samples were diluted in buffer to final concentrations of 1 µM, 500 nM and 250 nM. Samples were infused into a DNA carpeted flow cell for 380 s before switching to a wash buffer. Fluorescence intensity of the DNA carpet was measured over time. Both sample and wash buffer are infused at a rate of 20 µL/min.*

All the above samples were preincubated with ATP for 30 min prior to infusion. This allowed time for ParA2-GFP to associate with ATP, resulting in a higher proportion of ParA2-GFP in a state capable of binding nsDNA. To test for a time delay between ATP binding and ParA2-GFP configuring into a DNA binding state, an 'ATP start' assay was performed. Two separate syringes containing ParA2-GFP (2 µM, 1 µM and 500 nM) and a buffer containing ATP (2 mM) were infused into a T-mixer junction at the input of a DNA carpeted flowcell. The two solutions were combined inside the mixer, halving the sample concentrations to their final values (1 µM, 500 nM and 250 nM) prior to the sample

entering the flowcell. TIRF was used to measure the carpet intensity as ParA2-GFP bound nsDNA (**Figure 35**). The intensity was measured as close as possible to the flowcell inlet to reduce the time elapsed between ParA2-GFP and ATP mixing and the detection of protein binding. The steady state intensity level of all concentrations was significantly reduced compared to when preincubation was used. Proportionality between 500 nM and 250 nM was lost with both concentrations achieving a similar steady state level. The reduced ParA2-GFP steady state binding level and slower rate of association to the DNA carpet suggests the presence of a time-delay between ParA2s initial association with ATP and the ability for ParA2-ATP to bind DNA. These experiments were repeated at least 3 times within the same flowcell containing the same DNA carpet.

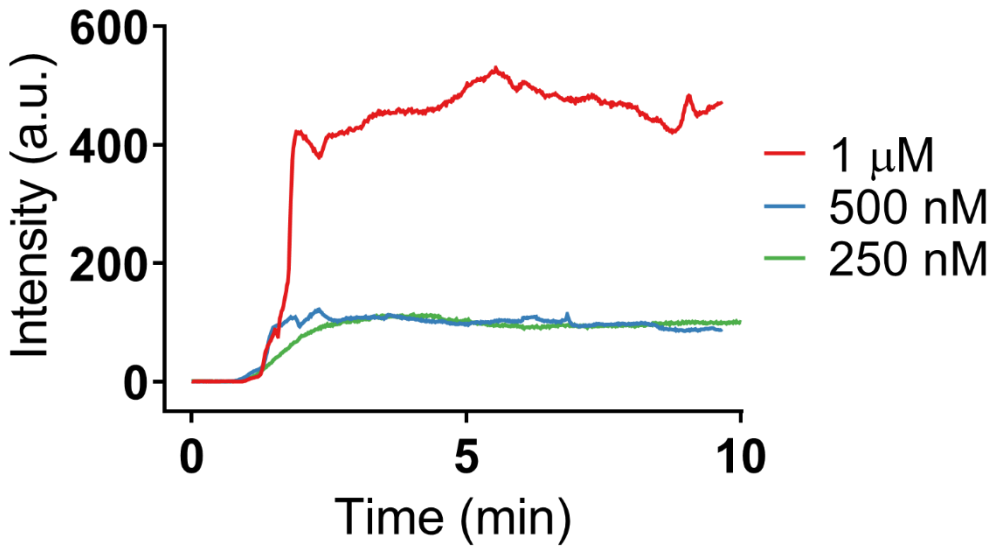

Figure 35. 'ATP start' assay of ParA2-GFP. *ParA2-GFP (2 µM, 1 µM and 500 nM) mixes with ATP (2 mM) within a T-mixer junction immediately upstream of DNA carpeted flowcell. Both ParA2-GFP and ATP solutions were pumped at equal rates of 10 µl/min. This resulted in final concentrations of ParA2-GFP (1 µM, 500 nM and 250 nM) and ATP (1 mM) entering the flowcell at 20 µl/min. The intensity traces here appear noisy in comparison to previous plots due to the different scale present on the vertical axis.*

3.3.4 Impact of additional cofactors on the dissociation rate of ParA2 from non-specific DNA

The same TIRF microscopy method above was used to measure the effect of additional cofactors on the dissociation rate of ParA2-GFP from nsDNA. Previously, it was unclear how freely diffusing ParB2 and DNA would interact with DNA bound ParA2. ParA2-GFP preincubated with ATP was flowed onto a DNA carpet until reaching a steady state. Flow was then switched to a wash buffer containing one of the following: nsDNA (100 µg/mL), ParB (2 µM), DNA + ParB (100 µg/mL and 2 µM respectively) or no additional cofactor (**Figure 36**). Buffer containing no additional cofactors produced a dissociation rate of 0.11 ± 0.001 s^{-1}. This rate was subtly increased to 0.13 ± 0.002 s^{-1} with the addition of 2 µM ParB to the wash buffer. ParB appeared to impede the rate of dissociation for the initial 20-30 s of

flow, indicating ParB's ability to stabilise the ParA-DNA interaction prior to triggering the hydrolysis of the ATPase. The addition of 100 µg/mL competitor nsDNA to the wash buffer had little effect on the rate of ParA2-GFP dissociation from the DNA carpet. The combination of 2 µM ParB and 100 µg/mL nsDNA within the wash buffer however resulted in the highest dissociation rate observed, measured at 0.15 ± 0.003 s^{-1}. This result provides evidence for ParA2-GFP transferring from the bound DNA of the carpet to freely diffusing DNA in solution, as well as stimulated hydrolysis of bound ParA2-GFP due to the added cofactors within solution.

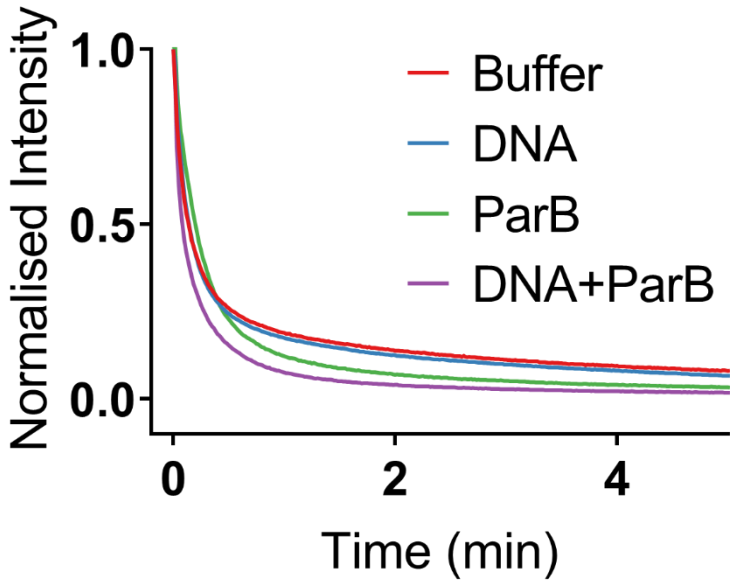

Figure 36. Dissociation of ParA2-GFP from DNA carpet with additional cofactors added to wash buffer. *Buffer containing 1 µM ParA2-GFP preincubated with ATP was infused into a DNA carpeted flowcell until a steady state was achieved. Flow was switched at t=0 to a wash buffer containing additional cofactors DNA [100 µg/mL], ParB [2 µM], DNA+ParB [100 µg/mL and 2 µM respectively] or no additional cofactor. Fluorescence intensity was measured over time. This figure shows the average of 3 measured intensities for each condition (as opposed to their fits), background subtracted and normalised to their prewash levels.*

3.3.5 Measuring ParA exchange time using FRAP

A mitotic model for the segregation of *V. cholerae* chromosome I was proposed by Fogel & Waldor, in which dynamic filaments of ParA1 pull the replicated origin towards the opposite cell pole (Fogel and Waldor 2006). Stable filaments of ParA2 had previously been shown to form with and without the presence of ATP *in vitro* (Hui et al. 2010). I therefore tested for the existence of ParA2 filament formation within a DNA carpeted flowcell. Fluorescence recovery after photobleaching (FRAP) was used to probe the mobility of ParA2-GFP when bound to nsDNA. The exchange time of ParA2-GFP was measured as it transitioned to and from a DNA carpet bound state. ParA2-GFP was flowed in significantly lower than the level required to saturate the DNA carpet, representing the lower concentration ratio of protein to DNA at physiological conditions. Sample flow was halted before

bleaching the carpet to roughly 50% of its intensity. The intensity of the bleached area was measured over the duration of its recovery (**Figure 37**).

The recovery of ParA2-GFP back to the DNA carpet occurred over two-time constants, 2.1 s and 150 s, corresponding to a fast and a slow species. The fast species accounted for most of the ParA2-GFP dimers with roughly 2/3 of the population. Upon the addition of ParB2, the recovery time constants of both ParA2-GFP species increased, most notably for the less present slow species. This effect was most apparent at 2:1 concentration ratio of ParB2 to ParA2-GFP, increasing the slow species time constant about τ=300 s. The accuracy of the determined slow rate was hindered by not being able to follow the FRAP trace for long enough. The increased recovery time of ParA2-GFP to the DNA carpet is an indication of the ability of ParB2 to impede ParA2 binding to nsDNA. This would allow for a significantly longer-lived depletion of ParA2 from areas where ParB2 is abundant, such as near a partition complex. This could be important to the production of a protein gradient that is of sufficient size to drive movement of the chromosome origin. The dominant faster species was significantly reduced in the presence of ParB2, converted primarily over to the unrecovered fraction. This increase in the unrecovered fraction hints at ParB2's ability to stabilise ParA2 to DNA. The slower species fraction was largely unchanged.

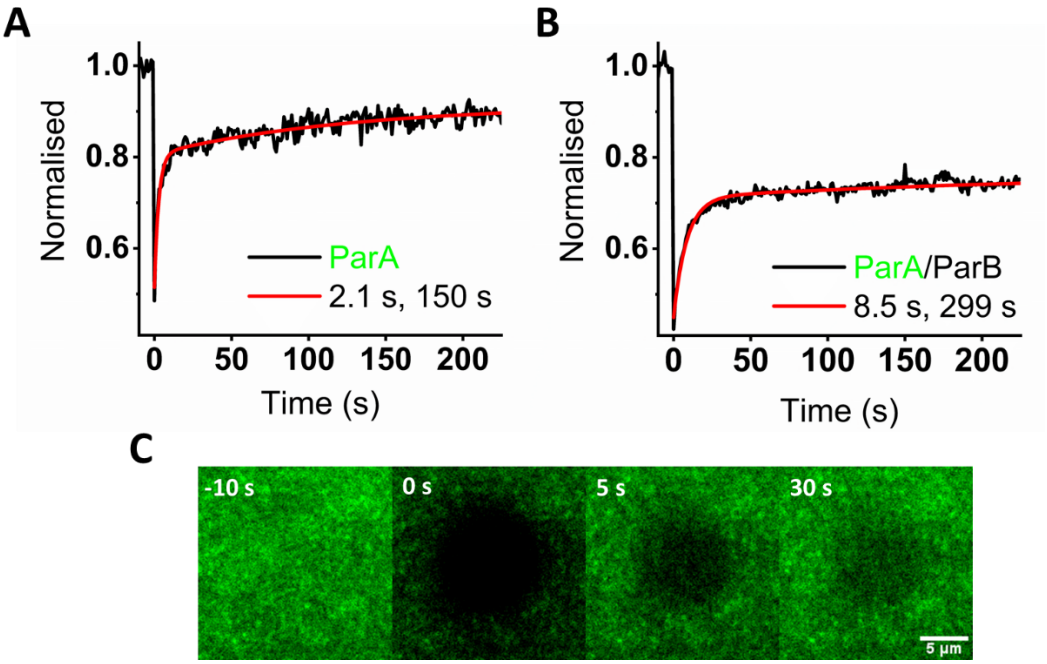

Figure 37. **(A) FRAP rebinding curve ParA2-GFP to DNA carpet at low carpet saturation.** Intensity of the bleached area was measured over time by measuring a 10x10 pixel area at the centre of the FRAP spot in ImageJ. Recovery curve was fitted to a two phase exponential decay function using OriginPro (red line), fixing the start of the fitting curve at t = 0 where recovery begins. Two rates correspond to a fast species (recovery time of 2.1 s) and a slow species (recovery time of 150 s). **(B) FRAP rebinding curve of ParA2-GFP with ParB (2:1 ratio).** Curve was again fitted to a double exponential (red line). The recovery times of both species increased (8.5 s for fast species; 299 s for slow species). **(C) Time-lapse images of ParA2-GFP rebinding DNA carpet at low carpet saturation.** Snapshot images of DNA carpet briefly prior and during the main rebinding portion of **Figure 33A**. Errors indicated in **Table 2** were calculated as ± standard deviation from 3 repeats.

3.4 Discussion

This chapter has explored the interactions which occur between ParA2 and DNA, and the how the introduction of different nucleotides and ParB2 can affect these interactions. ParA2 is the ATPase which drives the segregation process for *V. cholerae* chromosome II, so characterising its ability to bind DNA non-specifically provides more information into how this binding behaviour contributes to the force generation that powers chromosome segregation. To effectively image ParA2 binding and dissociating from DNA, a fluorescent tagged version of the ATPase protein (ParA2-GFP) was used in conjunction with a faux nucleoid surface formed inside a flowcell. TIRF microscopy was used to measure the quantity of ParA2-GFP bound to this artificial nucleoid, termed DNA carpet, by measuring the intensity emitted by associated ParA2-GFP.

3.4.1 ParA2-DNA interaction is dependent on ATP

In *par* systems, the ATPase functions as the primary motor which drives the segregation process of DNA after replication. Within the diffusion-ratchet model, the partitioning complex of a chromosome chases higher concentrations of ParA across the surface of the nucleoid (Vecchiarelli et

al. 2012). This concentration gradient is produced when the partition complex interacts with bound ParA-ATP, triggering its dissociation from the nucleoid through hydrolysis. It is this pattern of binding and unbinding of the nucleoid that allows ParA to dictate the direction and velocity of the partitioning complex. ParA2-GFP was shown to only bind with DNA when incubated either with ATP or and non-hydrolysable analogue, ATPγS. This binding occurred rapidly, with ParA2-ATP binding at a rate of 0.05 s^{-1}. Upon the dissociation from the DNA carpet, the off-rate of ParA2-ATP was measured at 0.11-0.19 s^{-1}. This off-rate far exceeded that of ParA from P1 plasmid (0.013-0.03 s^{-1}) and SopA from F plasmid (0.03 s^{-1}); which were previously measured using similar TIRF microscopy techniques (Vecchiarelli et al. 2010; Vecchiarelli et al. 2013). The increased binding and dissociation rates of indicates that chromosomal ParAs, at least in the case of *V. cholerae* chromosome II, may move with a greater velocity throughout the cell than homologue ParAs of plasmid systems. These binding and dissociation rates may vary significantly between different chromosomal ParAs, and could perhaps explain the dramatically different segregation patterns of chromosome I and chromosome II (Fogel and Waldor 2005). Simulations have already explored how changing the rate of ParA-ATP binding DNA gives rise to these different modes of segregation (Hu et al. 2017).

ParA2-GFP did not bind to the DNA carpet when incubated alone or with ADP. This result is contradicting to observations made in EM, where ParA2-ADP and ParA2 alone formed linear complexes with DNA (Hui et al. 2010). I believe that the reason why these complexes formed during these EM experiments was due to a very high protein to DNA concentration ratio. The conditions within the DNA carpet experiments are closer to *in vivo* conditions, where DNA concentration is far greater than that of ParA. Our data suggest that during chromosome segregation, ParA2 binds to DNA only when bound to ATP. This nucleotide dependence indicates the existence of an ATP switch which determines binding of DNA. ParA2 of *V. cholerae* chromosome II therefore exhibits a similar ATP-dependence for non-specific binding of DNA that ATPases from other *par* systems have shown previously (Leonard et al. 2005; Bouet et al. 2007; Vecchiarelli et al. 2010).

3.4.1 ParA2 delay in binding DNA

ParA2 which had been preincubated with ATP prior to infusion onto a DNA carpet showed instantaneous binding. However, the 'ATP start' experiment demonstrated a delay between the association of ParA2 and ATP and ParA2-ATP being able to bind DNA. This delay may exist to slow down the rebinding of ParA2 to an area of the nucleoid which has been recently cleared through hydrolysis by the partition complex. This ensures that a depletion of ParA can be established in the vicinity of the partition complex, encouraging its movement towards denser ParA concentrations. Without this delay, ParA may be able to recover back to the depleted area before a large enough concentration gradient can be formed, providing the partition gradient with no imperative to move

on. A similar time delay before DNA binding is enabled has only been demonstrated previously for ParA from P1 plasmid (Vecchiarelli et al. 2010).

3.4.2 ParA2-DNA interaction is stabilised by ParB2

The addition of additional cofactors to the wash buffer was used to measure their impact on the dissociation rate of ParA2 from the DNA carpet. ParB2 was expected to trigger the hydrolysis activity of ParA2, thus increasing the rate of dissociation. Instead, ParB2 was observed to reduce the initial dissociation of ParA2 from the DNA carpet, before proceeding to dissociate at an increased rate towards a lower overall baseline intensity. This observation hints at the ability of ParB2 to stabilise the ParA2-DNA interaction prior to promoting its eventual dissociation, since ParA2 remained bound to the DNA carpet for prolonged duration when ParB2 was present. Evidence from the FRAP experiments also support this ParA2-ParB2 stabilisation theory, exhibited by the slower recovery of ParA2-GFP to a bleached area of the DNA carpet when ParB2 was present. This effect has been previously observed during the reconstitution of the ParABS systems of P1 and F plasmid (Hwang et al. 2013; Vecchiarelli et al. 2013). This stabilisation may provide the partitioning complex enough time to properly anchor itself and search out more ParA2 on the nucleoid surface. This way, the partitioning complex never loses all its anchoring points at any one time and persistent motion across the nucleoid is possible. The transient ParA2-ParB2 interaction has also been shown to maintain the motion of the partitioning complex along the longitudinal axis in simulations of plasmid *par* systems (Hu et al. 2017).

Chapter 4

Using TIRF microscopy to visualise ParABS interactions and reconstitution of a chromosome segregation system

Parts of this chapter have been included in a review paper Brooks & Hwang 2017.

Expression and purification of all proteins was performed by Satpal Choda, Alexandra Parker and Sveta Sedeinikova. I performed all other experiments within this chapter.

4.1 Introduction

In vitro reconstitutions offer a powerful experimental approach to identify and test the essential aspects of a biological system (Liu and Fletcher 2009). Previous reconstitutions of actin-like type II (Garner et al. 2007) and tubulin-like type III (Fink and Löwe 2015) partition systems furthered knowledge of the bacterial cytoskeleton and its involvement within DNA segregation. Later, reconstitutions of type I partition systems found on plasmids were conducted and provided insight into the mechanism of the most ubiquitous subgroup. (Hwang et al. 2013; Vecchiarelli et al. 2013; Vecchiarelli, Neuman, et al. 2014; Brooks and Hwang 2017). To date, the reconstitution of a ParABS system of a bacterial chromosome has not been achieved. Type I partition systems are also found on chromosomes from both bacteria and archaea, but to date, none have been successfully reconstituted *in vitro*. In this chapter, the first reconstitution of a bacterial chromosome partition system is attempted.

In chapter 3, the non-specific DNA binding activity of ParA2 was investigated. The importance of nucleotide binding of ParA2 was described, evidencing the role of ATP binding and hydrolysis in the conformational changes which permit ParA2 to bind DNA non-specifically. The characteristics of the ParA2 and how it interacted with a DNA substrate were reminiscent of how homologue ParA proteins from P1 and F plasmid interact with DNA (Hwang et al. 2013; Vecchiarelli et al. 2013). This led to the hypothesis that protein gradients, already shown capable of displacing plasmids, can actively transport chromosomal DNA. This chapter builds on our initial work with ParA2, describing an attempt made at a full reconstitution of the ParABS system for *V. cholerae* chromosome II. We combined all 3 components of the chromosome's partition system (ParA2, ParB2 and *parS2*) within a DNA carpeted flow cell and used total internal reflection fluorescence microscopy to visualise the occurring interactions.

4.2 Materials and Methods

Note: Expression and purification of all proteins was performed by Satpal Choda, Alexandra Parker and Sveta Sedeinikova.

4.2.1 Coupling of *parS*-DNA to bead

40 µL of 10 mg/mL MyOne Streptavidin C1 Dynabeads (Invitrogen) were washed in wash buffer (10 mM Tris-HCl, pH 8.2, 1 M NaCl, 1 mM EDTA). The beads were then resuspended in 1.3 mL of wash buffer plus 3 µL Tween 20. The tube containing the bead suspension was then placed on a magnet and the supernatant discarded. The beads were resuspended again in the same volume of wash buffer and Tween 20, magnetically pulled down, and the supernatant discarded a further 2

times for a total of 3 washes. Biotinylated *parS2*-DNA (2.9 kb, 5 pM in 50 µL) with a biotin molecule at one end and a Cy5 molecule at the other was added with 1.3 mL of wash buffer and 3 µL of Tween 20 to the beads and incubated whilst rotating at 193 rpm for 1 hr. The beads were then washed in 1.5 mL of wash buffer according to the manufacturers instructions for a further 3 times. Afterwards, the beads were resuspended in 40 µL of elution buffer (30 mM Tris-HCl, pH 7, 100 mM KCl, 1 mM EDTA) and stored on ice.

4.2.2 *V. cholerae* ParABS2 reconstitution

Reaction A: ParA2-GFP (5 µM) was incubated for 15 min at 30 °C in ParABS reaction mixture (1x Par buffer, 2 mM ATP, 0.1 mg/mL α-casein, 2 mM DTT) for a total volume of 20 µL. At the same time, reaction B was prepared: ParB2 (40 µM) was incubated with *parS*-DNA beads (2 mg/mL) for 30 min at room temperature in reaction mixture to a total volume of 20 µL. After incubation time had elapsed, a magnet was used to pull the beads in reaction B down and 15 µL of solution was removed. Reaction A was added to 175 µL of reaction mixture to form reaction C. Reaction C was added to the *parS* beads to form a 1:8 sample of ParA to ParB/*parS* beads.

The 1:8 sample was loaded into a 1 mL syringe (BD) and attached to the inlet port of a DNA-carpeted flow cell mounted to the microscope. The DNA carpet was visualised through TIRF using 1 in 1000 stroboscopic illumination (1 ms exposure times at 1 s intervals) through the dual-view system, allowing ParA2-GFP and Cy5-*parS*-DNA to be detected within the green and red emission channels respectively. The sample was infused into the flow cell at 20 µl/min for 380 s, at which point flow was stopped. Beads bound to the DNA-carpet along with their surrounding depletion zones were measured and recorded using Micro-manager software within ImageJ.

4.3 Results

4.3.1 Using *parS2* beads to represent the chromosome origin

Interaction between the components of a partition system occur at centromere-like partitioning sites within the DNA, termed *parS* sequences. ParB adapter proteins binds specifically to the *parS* sites, and subsequently spreads over adjacent DNA sites (Rodionov et al. 1999; Murray et al. 2006; Broedersz et al. 2014; Sanchez et al. 2015; Soh et al. 2019). The result is a nucleoprotein complex, termed a partition complex. The presence of ParB within the partition complex is believed to trigger the ATPase activity of DNA bound ParA dimers, causing ParA to dissociate from DNA.

Segregation of chromosome II origins initiates from these formed partition complexes. Once replicated, partition complexes on sister chromosomes move from the mid cell with directed motion through the cell volume before coming to rest at the quarter cell positions. The *parS* sequences of

V. cholerae chromosome II, termed *parS2*, differ in their sequence from the *parS1* sequences on the larger chromosome I. 9 *parS2* sites have been identified within the chromosome, with the majority located near the origin of replication (Yamaichi, Fogel, McLeod, et al. 2007). The proximity of the *parS2* sites to the origin suggests the priority of partition systems within the chromosomes to properly segregate the DNA regions around the origin of replication. To represent the origin region of chromosome II within the *in vitro* reconstitution, magnetic beads were coated with DNA strands, each encoding a single *parS2* site. When incubated with ParB2, partition complexes are formed over the surface of the beads as the protein bind the DNA strands. The *parS2* DNA strands were tagged with a Cy5 molecule, making the *parS2* DNA visible within the red channel of the microscope's detector. A biotin molecule was attached to the opposite end of the DNA strand, allowing binding to neutravidin molecules on the exterior of the magnetic beads (**Figure 38**).

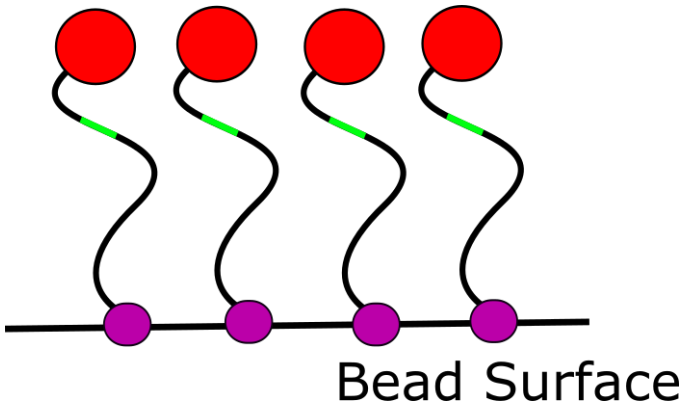

Figure 38. DNA with single parS site attached to magnetic bead. *Short strands of DNA included a single parS site (green). The DNA featured a Cy5 molecule (red) at one end and a biotin molecule (purple) at the other end to bind to the bead surface.*

The beads (Dynabeads MyOne Streptavidin C1, Invitrogen) measured 1 µm in diameter and were superparamagnetic, allowing them to be confined within the illumination field of the microscope using a magnet situated directly above the sample stage. Before they could be used within the reconstitution, the magnet had to be aligned directly over the microscope field of view. This was necessary to make sure that the beads did not move with directed motion in the absence of Par proteins. The *parS2* beads were flowed into a DNA carpeted flow cell and imaged using TIRF microscopy. Illumination of the beads using the 633 nm laser excited the Cy5 molecules, which were detected within the red emission channel of the microscope.

4.3.1.1 Magnet alignment in preparation for reconstitution

Experiments showed that the DNA-coated beads were highly sensitive to the position of the confining magnet above the flow cell. If the magnet were not directly aligned over the centre of the objective, the beads within the field of view would experience lateral forces, causing them to drift in

unison across the microscope's field of view. It was essential to eliminate this drift by correctly aligning the magnet to the objective otherwise any directed movement due to the protein interactions would have been impossible to detect.

Magnetic bead movies were analysed using the 2D single molecule tracking program, Mosaic (Sbalzarini and Koumoutsakos 2005). The program draws a displacement trace for each bead, allowing the user to visualise the exact path taken by a bead over the course of the acquisition. When viewing several beads within the same field of view, Brownian diffusion was confirmed when all beads show no preferred direction of motion. Examples of bead trajectories are seen in **Figure 39**. Within this figure, the blue bead moves with directed motion, whilst all the other beads appear to diffuse randomly. The magnet therefore cannot be aligned in this instance, since not all the beads diffuse randomly. By following this process, we were able to align the magnet to the objective, so any lateral forces experienced by the beads due to the magnetic field were negligible. If beads were seen to not displace significantly or with no preferred direction after 15 minutes of observation, the magnet was determined to be sufficiently aligned to the objective. This process involved observing 3-10 beads within a single field of view and tracing their movement using Mosaic.

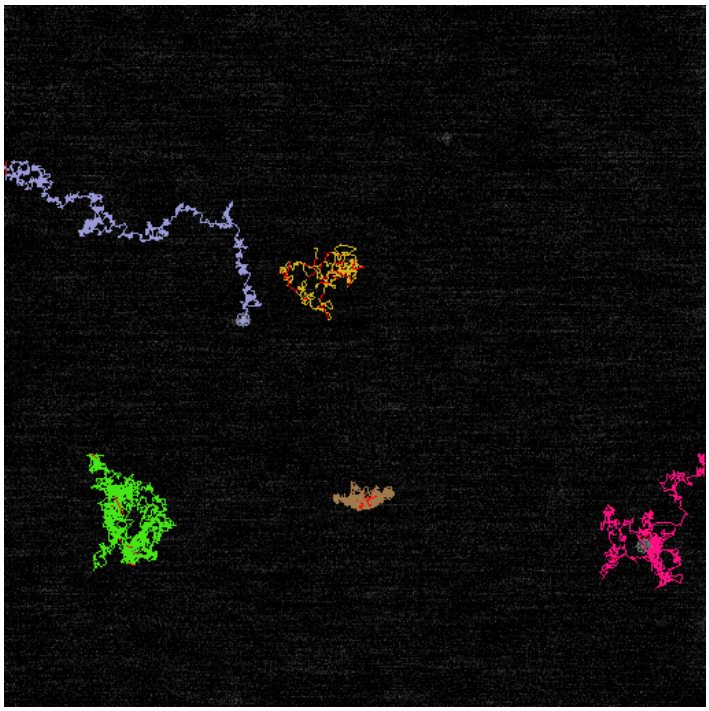

Figure 39. Displacement traces of magnetic beads. *Magnetic beads were introduced into a flow cell and imaged over a 15 min period at 1 fps, 100 ms exposure. The background was subtracted, and movies were analysed using the 2D single particle tracking software, Mosaic. Traces were interpreted by eye to determine if bead movement was directed or random. The blue bead trace shows a directed motion pattern whilst all the other beads are diffusing randomly. This example is therefore representative of a magnet which is not properly aligned, since not all beads diffuse randomly. A bead was determined to be randomly diffusing if its overall position shift was close to zero after 15 minutes observation and no preferred direction of diffusion was observed.*

Unison drifting of all beads was still present when the flow cell's attached tubing was disturbed. This was found when periodic blasts from the air conditioner onto the stage would cause all beads within the field of view to rush towards either the inlet or outlet (vertically on the screen). This sudden motion of the beads was most likely due to the changes in pressure within the sample solution caused by the flexing of the tubing. It was therefore very important that physical disturbance of any of the connecting tubing was kept to a minimum during any experiments involving the beads. This alignment procedure had to be revisited prior to each reconstitution attempt. Once the magnet was correctly aligned, *parS* beads appeared to diffuse with no preferred direction of travel and were not seen to stick in place on the DNA carpet. At this point, it was possible to add ParA2-GFP and ParB2 proteins to the flow cell and observe for interaction between the components of the partition system.

4.3.2 ParA depletion zones

ParA2-GFP (5 µM) was pre-incubated with ATP (1 mM) for 30 min at 25°C. *parS2* beads (2 mg/mL), measuring 1 µm in diameter, were incubated with ParB2 (40 µM) for 30 min. This pre-incubation step allowed the *parS2* sequences and ParB2 to associate and form partition sites on the surface of the beads. After incubation, the ParB2/*parS2* beads were combined with the ParA2-GFP and diluted 10x in buffer resulting in a final 1:8 concentration ratio of ParA2-GFP (500 nM) to ParB2 (4 µM). The sample was infused into a DNA-carpeted flow cell and imaged using TIRF microscopy. ParA2-GFP bound non-specifically to the DNA carpet upon infusion, observed as an increased intensity within the green emission channel. Upon stopping flow, the intensity of the DNA carpet within the green channel plateaued, signalling that a steady state of ParA2-GFP bound to the DNA carpet had been reached. Magnetic beads became visible within the red channel immediately upon stopping flow as they rose to the top of the sample chamber. Whilst most magnetic beads were fixed stationary to the slide surface, others wiggled on the spot. The stationary beads displayed a greater intensity within the green emission channel, evidencing a larger number of ParA2-GFP molecules co-localising with the beads. This was attributed to an insufficient number of correctly formed partition complexes on the beads. This was evident from the similar intensity of beads in the red channel, proving that difference in green intensity was not due to different heights of the beads. After 3-4 min, ParA2-GFP depletion zones formed around the perimeter of most of the beads (**Figure 40**). The depth of the depletion zones, measured as the intensity difference between the depletion zone and the surrounding DNA-carpet, was observed to be greater for beads which exhibited less green emission on their surface (**Figure 41**). A lower bead intensity within the green channel indicated less ParA2-GFP binding directly to the bead surface. This was likely due to enough partition complexes on the surface of these beads to prevent ParA2-GFP binding. The formation of ParA2-GFP depletion

zones was not followed by the directed motion of the beads as previously anticipated. Instead, the beads merely wiggled within their depletion zones, tethered to the spot.

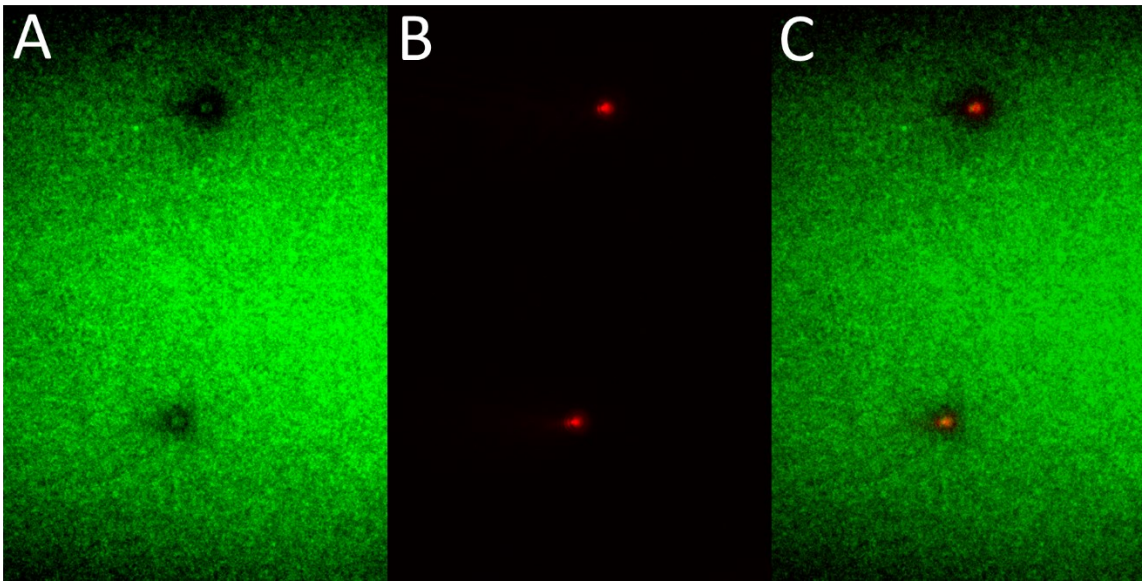

Figure 40. Visualising ParA2-GFP depletion zones on DNA carpet surrounding two ParB2/parS2 beads. *ParA2-GFP and ParB2/parS2 beads were flowed into a DNA carpeted flow cell and imaged using TIRF microscopy. ParA2:ParB2 concentration ratio of 1:8. ParA2-GFP was detected within the green channel (A) whilst parS2-Cy5 on the beads was detected in the red channel (B). A composite image of both green and red channels (C) shows that areas of DNA surrounding ParB2/parS2 beads became depleted of ParA2-GFP.*

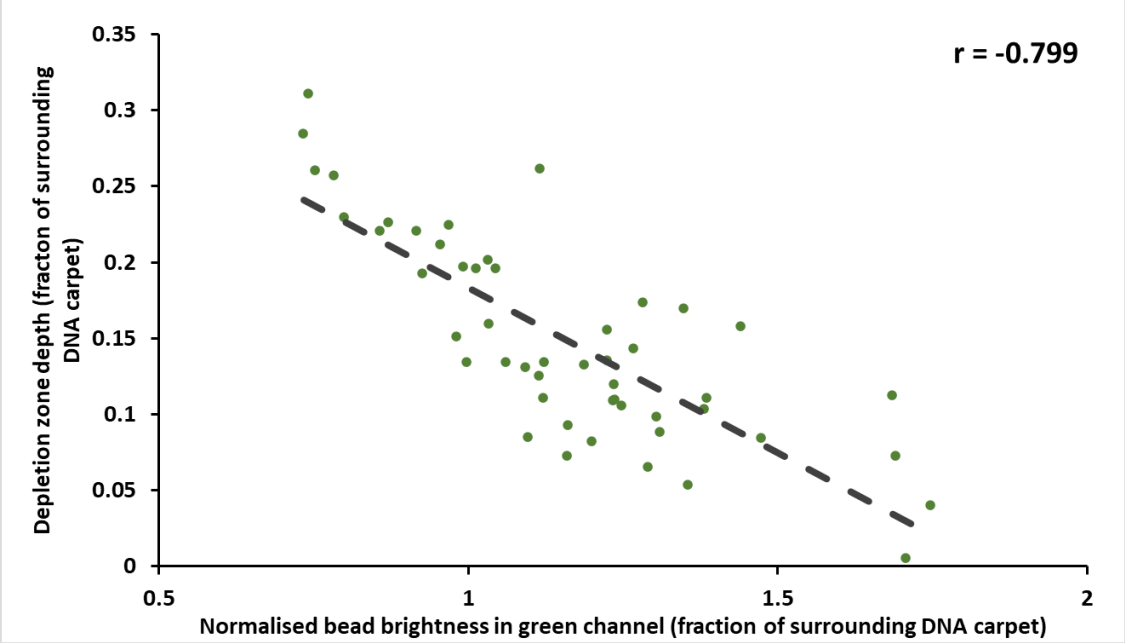

Figure 41. Depth of depletion zone surrounding beads related to the peak brightness of beads in green channel. *The strength of ParA2-GFP depletion zones varied with the intensity of the ParB2/parS2 bead within the green channel. The "depth" of the depletion zone was determined as the difference between the intensity of the DNA carpet adjacent to the bead to the surrounding carpet. A Pearson's correlation coefficient of -0.799 was calculated from a linear fit (dashed). Non-linear fits were also tested but did not accurately model the data with $R^2 > 0.7$. Both axes are measured relative the brightness of the DNA carpet. ParA2:ParB2 concentration ratio of 1:8.*

4.3.3 ParA:ParB concentration ratios

Several concentration ratios were used to test how this affected the formation of ParA depletion zones on the DNA carpet. 1:1, 1:2 and 1:4 ParA:ParB produced no visible ParA2-GFP depletion zones on the surrounding DNA carpet (**Figure 42**). Many of these beads however did move on the carpet, but this was due to diffusion, not to any interactions between ParA2 and ParB2/*parS2* on the beads. Significant colocalization of ParA2-GFP and *parS2*-DNA on the bead occurred for 1:1, 1:2 and 1:4 concentration ratios, indicating the inability of ParB2/*parS2* complexes to prevent ParA2-GFP from binding non-specifically to DNA on the bead. The only ParA:ParB concentration ratio for which the formation of depletion zones were observed was 1:8. Beads which formed depletion zones were all stationary on the DNA carpet. As mentioned in a previous section of this chapter, in the absence of ParA2-GFP and ParB2, *parS2* beads were observed to diffuse randomly in 2D on the DNA carpet.

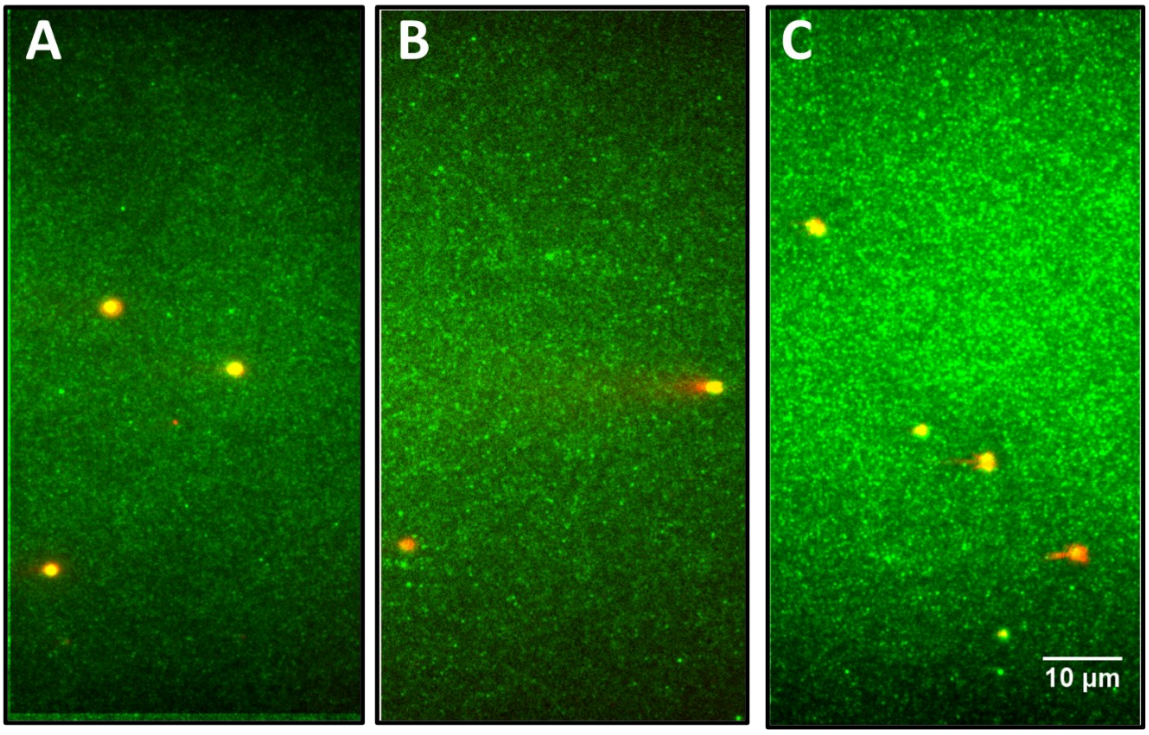

Figure 42. Visualising ParB2/parS2 beads on ParA2-GFP coated DNA carpet at different ParA2:ParB2 concentration ratios. *Varying concentrations of ParA and ParB were used to test the effect of ParA2:ParB2 concentration ratios on depletion zone formation. The ParA2:ParB2 concentration ratios used were (A) 1:1, 1 µM ParA2-GFP and 1 µM ParB2; (B) 1:2, 250 nM ParA2-GFP and 500 nM ParB2 (C) 1:4, 500 nM ParA2-GFP and 2 µM ParB2.*

4.3.4 Dependence of height of confining magnet

I tested whether the force of the confining magnet was responsible for holding the beads stationary to the surface by increasing the distance between the magnet and the sample. It was found that once adhered to the carpet, the beads remained in place regardless of the strength of the external magnetic field. Surprisingly, the beads remained fixed to the surface even after the magnet was completely removed, suggesting that the beads adhered to the surface of the DNA carpet through

molecular interactions. However, a further test in which the magnet was removed prior to flow in of the beads resulted in no beads visible at the TIRF imaging surface. This was most likely due to the mass of the beads causing them to sink and stay at the bottom of the flowcell, disallowing their interaction ParA2-GFP bound to the visible DNA carpet. Beads were seen to adhere to each other and form stacks/chains of 3-7 units in length. These stacks of beads were observed to hang from the DNA-carpet. These stacks comprised of a single bead adhered to the DNA carpet, attached to a chain of beads which extended into the volume of the flow chamber. These stacks could be pushed flat against DNA carpet by increasing the sample flowrate. The cause of this stacking was most likely due to the magnetic force between beads holding them together.

4.4 Discussion

The function of ParABS within the bacterial chromosome is to segregate newly formed copies of the chromosome's origin of replication. ParABS is also believed to fine tune the final positioning of the chromosome origin to the quarter cell positions. In this chapter, a cell-free reconstitution of the ParABS system from *V. cholerae* chromosome II was attempted. Purified components of the partition system were infused into a DNA carpeted flow cell and observed using TIRF microscopy. Reduced ParA2-GFP density was observed surrounding ParB2/*parS2* beads on the surface of a DNA-carpeted flow cell. These 'depletion zones' evidence the formation of chromosomal ParA protein gradients, similar to those exploited by plasmid DNA in previous *in vitro* reconstitutions to facilitate directed motion (Hwang et al. 2013; Vecchiarelli et al. 2013; Vecchiarelli, Neuman, et al. 2014). These results imply the existence of a diffusion ratchet model for the segregation of *V. cholerae* chromosome II, as opposed to a filament based model presented within previous studies (Fogel and Waldor 2006; Ptacin et al. 2010).

4.4.1 Confining magnetic beads within TIRF field

The microscope used a magnetic field perpendicular to the sample to confine magnetic beads at the imaging surface of the flow chamber. Before we could use magnetic beads to study directed movement due to the ParABS system, we needed to ensure the beads diffused randomly in the absence of any proteins. Although the magnet was aligned to prevent any lateral force influencing the beads movement, drifting still took place. This was due to the movement of solution through the flow cell when the connecting tubing was disturbed. It was therefore important that precautions were taken to prevent agitation of the flow cell during imaging. One such precaution could be to isolate the solution inside the flow cell after the beads had been infused by clamping the inlet and outlet tubing. We were unable to carry out this clamping method however due to the brittleness of the microfluidic tubing, causing it to rupture when clamped.

4.4.2 Chromosomal ParA depletion zone formation

Combining all the purified components of the chromosome II ParABS system within a DNA carpeted flow cell resulted in areas of ParA2-GFP depletion around some ParB2/*parS2* beads. I believe the cause of this depletion was the hydrolysis of DNA bound ParA2-GFP, triggered by interactions with ParB2/*parS2* complexes on the surface of the magnetic beads. This result signifies the first reconstitution of a chromosomal ParA depletion zone. The creation of depletion zones, stimulated by the presence of ParB/*parS*, indicates that self-organising ParA concentration gradients could potentially be the driving mechanism behind bacterial chromosome segregation. Due to the conservation of ParABS systems across a multitude of bacterial species, this result has further implications outside of *V. cholerae* and could be used to better understand the general mechanisms of chromosome segregation in prokaryotes. Another possible explanation for the formation of these depletion zones is that ParA2-GFP does not hydrolyse and simply binds and unbinds from the DNA carpet, but struggles to bind in locations where ParB/*parS* is present. This effect of ParB slowing down ParA2-GFP rebinding to the DNA substrate was observed within the FRAP experiments within chapter 3 of this thesis.

4.4.3 Depletion zone depth dependent on bead brightness

A ratio of 1:8 ParA2 to ParB2 was needed to form depletion zones. This required very high concentrations of ParB2 (40 µM) to be pre-incubated with the *parS2* beads. Once flowed in and visualised on the DNA carpet, different ParA2-GFP densities were observed on the surface of the beads, with brighter beads producing shallower depletion zones. A negative correlation ($r = -0.799$) was observed between the intensity of ParA2-GFP bound to the magnetic beads and the depth of the depletion zones. This result indicates that although the presence of ParB2/*parS2* on the beads was able to induce ParA2-GFP depletion, this interaction was not optimal for many of the observed beads, with ParA2-GFP able to bind directly to the *parS2*-DNA. This hints at varying levels of partition complex formation across the population of beads. A possible reason for this was a lack of *parS2* sites available to form an effective partitioning complex. Each DNA molecule attached to the surface of the bead contained a single *parS2* site. *V. cholerae* chromosome II contains 9 *parS2* sequences, 6 of which are clustered close to the origin of replication (Yamaichi, Fogel, McLeod, et al. 2007). For our reconstitutions, a single parS2 site was located on each DNA strand attached to the magnetic beads. Perhaps there were too few *parS2* sites for ParB2 to bind, limiting the maximum density of partitioning complexes that were able to form on the surface of the beads. ParB is known nucleate at the site of *parS* sequences and subsequently spread to adjacent non-specific DNA, bridging together DNA regions into a nucleoprotein complex *in vivo* (Murray et al. 2006; Breier and Grossman 2007; Broedersz et al. 2014; Graham et al. 2014; Sanchez et al. 2015; Taylor et al. 2015; Debaugny et

al. 2018). The mechanism by which the nucleoprotein complex optimises segregation is debated; whether it improves ParA to DNA contact or provides the correct DNA topology for segregation is still unknown. However, the formation of a nucleoprotein complex has been shown to be essential for partitioning, with ParB mutants incapable of spreading showing ineffective DNA partitioning activity (Rodionov et al. 1999; Autret et al. 2001; Breier and Grossman 2007; Kusiak et al. 2011; Graham et al. 2014). Therefore, perhaps within our reconstitution of the ParABS system of chromosome II, inefficient nucleoprotein complexes were formed on the surface of the beads. Recent *in vitro* work reconstituted ParB spreading by adding cytidine triphosphate (CTP) (Osorio Valeriano et al. 2019; Jalal et al. 2020). ParB bound to a CTP molecule has been shown to have an open configuration when in the presence of *parS*. The ParB dimer then closes into a loop around the *parS* site and loses its affinity for the sequence, causing it to spread onto adjacent DNA (Kawalek et al. 2020). Addition of CTP may therefore be required to form the nucleoprotein complexes required for the reconstitution of chromosome II segregation. The identification of ParB as a possible CTPase occurred at the same time of writing this thesis, and so an experiment involving CTP was not performed. If CTP were to be included however, it is possible that the DNA attached to the beads would need to be adapted. The *parS* DNA on the magnetic beads used in our reconstitution attempts was open at one end to allow tagging with Cy5. This would allow ParB spreading from the *parS* site to potentially slide off the DNA strand completely. To form a closed loop of *parS* DNA at the beads surface, both ends of the DNA strand should have an attached biotin, providing two points of connection with the neutravidin on the bead. Additionally, increasing the number of *parS* sites within the should also be tested, to see if this has an effect on the formation of protein gradients.

4.4.4 Next steps towards directed motion

The formation of ParA2 depletion zones surrounding ParB2/*parS2* beads lends significant support towards a diffusion ratchet model for chromosome segregation. Similar depletion zones were previously observed during the reconstitutions of the P1 and F plasmid ParABS systems (Hwang et al. 2013; Vecchiarelli et al. 2013). During these reconstitutions, directed motion of plasmid DNA was observed shortly after the formation of these depletion zones. However, although depletion zones were observed during our reconstitution attempts, no directed motion observed. This raises questions about whether the ParABS system of chromosome II is in fact a minimal system, or if additional components are required for directed motion to be produced.

As mentioned above, proper formation of nucleoprotein complexes is a requirement for DNA segregation to occur. Therefore, it is important that the addition CTP and an increase in the number of *parS2* sites on each *parS2*-DNA strand is tested to see if this has any effect on the formation of depletion zones or the movement of the magnetic beads. There was also evidence of unbound

ParB2 remaining in solution after preincubation with the *parS2* beads, perceivable as a reduced intensity of DNA bound ParA2-GFP. ParB2's ability to impede the binding of ParA2-GFP to DNA had already been evidenced by FRAP experiments, described in chapter 3. This may have increased the difficulty of forming depletion zones due ParB2 restricting ParA2-GFP binding to the DNA carpet. A potential improvement to the method used in the above experiments could be to involve a magnetic pull down of the beads after the preincubation step. This way, unbound ParB2 which failed to load onto *parS2*-coated beads could be removed before mixing with the ParA2-GFP and infusion onto the DNA carpet.

Within this chapter, the interactions which occur between components of the ParABS system were studied using a 2D geometry. Using this method, we have been able to observe the first chromosomal ParA depletion zones. However, partitioning complexes for both plasmids and chromosomes have been shown to be contained within the nucleoid volume for *B. subtilis* (Le Gall et al. 2016). This means that positioning of the partitioning complex *in vivo* occurs within a 3D space, not the 2D surface bound conditions within our flow cells. The lack of directed motion may therefore have been due to ParA2-ParB2 interactions occurring only on one side of the bead. It would be therefore useful to be able to conduct similar reconstitution experiments, whilst visualising interaction between proteins within smaller confines. If suitably small vessels could be created that allow the beads to contact multiple ParA surfaces, the force generation due to protein gradients may become sufficient to induce directed motion.

Chapter 5

Solution-based TIRF using sCMOS for high-throughput, single molecule detection

Expression and purification of all proteins was performed by Satpal Choda, Alexandra Parker and Sveta Sedeinikova. Cy5-DNA was constructed by Satpal Choda. I performed all other experiments within this chapter.

5.1 Introduction

ParA ATPase is only able to bind DNA after dimer formation; a process which requires the presence of a bound molecule of ATP (Vecchiarelli et al. 2010). When ATP is hydrolysed into ADP, the ATPase ParA undergoes a conformational change, causing it to lose its affinity for DNA. This way, the process of assembly and disassembly of ParA from the nucleoid surface is essentially regulated by the conformational switch of the protein molecule. These conformational changes in proteins often occur over small distances that are beyond the sensitivity of most light microscopes, including the TIRFM setup used throughout this project. Alternative methods must therefore be used to observe and measure these subtle changes as they occur. TIRF microscopes can be adapted to probe interactions which occur over 1–10 nm distances through improvement of the signal to noise ratio of imaged molecules, made possible by new detector technologies and brighter fluorophores. The use of single-molecule FRET also allows interactions to be observed over the sub-10 nm range. Faster framerates made available by sCMOS detectors have also made it possible to detect fast diffusing particles through small illumination volumes.

TIRF microscopy uses the limited penetration depth (100-300 nm) of illumination light to selectively excite fluorophores close to the coverslip surface. By limiting the emission of out of focus fluorophores in this way, molecules close to the microscope cover slip have improved signal to noise ratios, allowing them to be individually detected (Axelrod 1981). The requirement for molecules to be located so close to the coverslip however does restrict the use of TIRF microscopy to slow moving or stationary molecules if the desire is to monitor the same molecule over an extended time. This is achieved through surface immobilisation of labelled molecules to the coverslip, ensuring that the molecule remains within the TIRF excitation field for the duration of the experiment. Fast moving molecules on the other hand would exit the thin TIRF illumination field before multiple captures can occur. However, surface immobilisation can affect the function of some biomolecules, including proteins. Proteins can contain many chemical groups and form complex 3D structures. This 3D structure (conformation) can undergo significant change when the protein is in contact with a surface or when preparing a protein for surface immobilisation (Karlsson et al. 2005; Mateo et al. 2007; Felsovalyi et al. 2012). Since a protein's conformation is intrinsically linked to its function, these conformational changes introduced through surface immobilisation can limit insight into the role and functionality of a protein.

This chapter describes the optimisation of the TIRF microscope built in chapter 3 to allow for high-throughput, single-molecule detection. An sCMOS detector is used to increase the number of frames a single molecule is measured over and the brightness of fluorophores is optimised for high speed

detection. The pixel array of the sCMOS detector is utilised alongside a custom molecule detection program to enable high-throughput detections of individual, freely diffusing molecules. This idea arose from the multiplexing of fluorescence correlation spectroscopy (FCS) measurements through the use of an EMCCD pixel array (Kannan et al. 2006).

5.2 Materials and Methods

Note: Expression and purification of all proteins was performed by Satpal Choda, Alexandra Parker and Sveta Sedeinikova. Cy5-DNA was constructed by Satpal Choda.

5.2.1 Imaging Cy5-DNA

233 bp DNA strands tagged with a Cy5 molecule were created *via* a polymerase chain reaction (PCR). 300 pM Cy5-DNA was diluted in buffer containing glucose oxidase (100 nM) and catalase (1.5 µM), to remove molecular oxygen from the system, reducing the potential for oxidisation of dyes (Aitken et al. 2008) ; and Trolox (1.5 mM), to reduce oxidative stress on fluorophores and reduce the rate of permanent photobleaching of Cy5 (Cordes et al. 2009). DNA was introduced into an empty flow cell mounted to the TIRF microscope stage. Illumination was provided by a 633 nm pig-tailed laser (Cobolt). Cy5-DNA strands were detected within the red channel of the Dual View system (Photometrics) using a Prime 95B sCMOS detector (Photometrics).

5.2.1 Multiplexing detections using an sCMOS detector

5.2.1.1 Treating each pixel as its own detector

To multiplex the number of detections which can be made per captured frame, an algorithm was developed to treat each pixel as a separate detection entity. Tiny, parallel detection volumes were created by utilising the pixel array of an sCMOS camera (Prime95B, Photometrics). The dimensions of each pixel provided the x-y confines of the detection volumes. The depth of the detection volumes was provided by TIRF illumination, which formed a thin evanescent wave at the sample coverslip (**Figure 43**). By utilising the entire pixel array (1024x1024), parallel detection of molecules was automatically facilitated by multiple excitation volumes. The dimensions of these detection volumes could be multiplied four times through artificial pixel binning during acquisition. This is the process of summing the intensity of several adjacent pixels into a “super pixel” to provide a single intensity value. Although binning of pixels results in a reduced total number of detection volumes, it increases the retention time of molecules by effectively increasing the space they can explore before exiting the detection volume. For this reason, 2x2 binning was applied to all acquisitions.

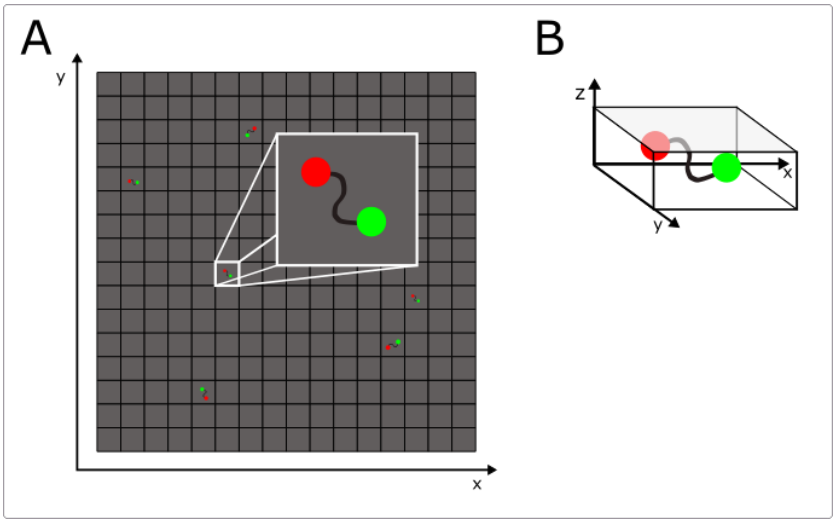

Figure 43. Pixels as individual detection volumes. *(A) Each pixel forms a 110 nm² illuminated area on the sample when viewed through a 100x magnification objective lens. (B) z-axis dimensions of the detection volumes are provided by the depth of the evanescent wave, typically around 100 nm.*

5.2.2 Identifying fluorescence bursts

A MATLAB based program was developed to identify fluorescent molecules as they passed through the detection volumes. Using a basic thresholding algorithm, the program identified every frame where the measured intensity of a pixel exceeded a pre-determined amount. Qualifying frames in which the threshold intensity level was exceeded were assigned to a matrix called “arrival times”, detailing the pixel number, frame number and the measured intensity. Multiple instances of arrival times which occurred within a short period of time were attributed to a single molecule diffusing through the detection area and termed a “burst”. This is similar to the molecule detection algorithms used by conventional solution-based smFRET (Eggeling et al. 1998). To be classified as a burst, a minimum number of arrival times (m) must occur within a set number of adjacent frames (T). For example, if T = 10 frames, and m = 5, then the intensity of at least 5 out of 10 frames must exceed the threshold intensity to confirm the presence of a burst. This is known as a sliding window burst search. The sliding window length in seconds is calculated *via* the value T. Within the program, T is measured in frames, so in order to convert T into a time measurement, T is multiplied by the frame rate at which the stack was recorded. For example, two stacks recorded at 1 fps and 2 fps would create a sliding window of 50 s and 100 s respectively for T = 50.

$$framerate\ (s) \times T = Sliding\ Window\ Length\ (s)$$

5.3 Results

5.3.1 Comparing detector technology: EMCCD vs sCMOS

The most popular detectors used for microscopic imaging are based on electron multiplying charge coupled device (EMCCD) and scientific complementary metal oxide semiconductor (sCMOS) sensor

technologies. As the most developed technology, EMCCD cameras are typically the primary choice for single molecule applications due to the large well depths and low read noise they offer. However, recent advances in sCMOS camera technology have made them more competitive, offering increased spatial resolution, higher maximum frame rates and larger fields of view. The performance of two detectors; a Photometrics Evolve 512 Delta (EMCCD) and a Photometrics Prime 95B (sCMOS) was compared to find out which camera technology would be most suitable for our setup (**Table 3**).

	Evolve 512 Delta	**Prime 95B**
Max frame rate (full array)	67.5 fps	41 fps (16-bit) / 82 fps (12-bit)
Full well capacity	185,000e-	80,000e- (16-bit) / 10,000e- (12-bit)
Array size	512 x 512 pixels	1200 x 1200 pixels
Pixel area	16 µm x16 µm	11 µm x11 µm
Peak Quantum efficiency	>90%	>95%
Read noise	<1e- (Using EM gain)	1.3e-

Table 3. Specifications of Evolve 512 Delta and Prime 95B. *Specifications were acquired from Photometrics datasheets for both the Evolve 512 Delta and Prime 95B.*

Both cameras were tested to determine which provided the highest signal to background (SBR) using fluorescent beads as a reference imaging sample. The sample was prepared by depositing a 10 µL droplet of 200 nm fluorescent beads (Invitrogen, dark red (Ex:660/Em:680)) onto a microscope slide, allowing them to settle onto the slide surface. Once the droplet was dry, the beads were resuspended in distilled water and enclosed with a glass coverslip. The beads were imaged using both the Prime 95B and the Evolve 512 Delta under TIRF illumination using an illumination wavelength of 633 nm and their brightness measured. The peak intensity of the bead and the low intensity area adjacent to the bead was recorded using the line profile tool within ImageJ. The signal to background ratio was calculated by the following equation:

$$SBR = \frac{Signal}{Background}$$

The Prime 95B showed a marked improvement in signal to background performance over the Evolve 512 Delta (**Figure 44**).

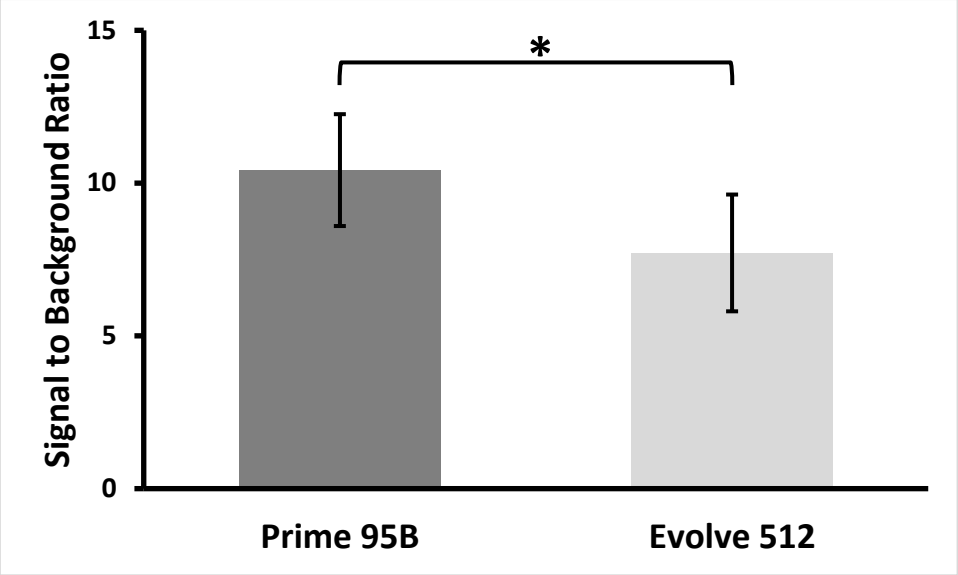

Figure 44. Signal to background performance comparison for sCMOS and EMCCD cameras. *Fluorescent beads were imaged using both Prime 95B (sCMOS) and Evolve 512 Delta (EMCCD) cameras. The peak intensity of the bead and the low intensity area adjacent to the bead was recorded using the line profile tool within ImageJ. Images were taken using a constant illumination power of 50 µW and an exposure time of 100 ms. The Prime 95B was operated in "Sensitivity" mode whilst an EM-gain of 200 was applied to the Evolve 512 Delta. Statistical significance determined via unpaired t-test comparing signal to background using each camera; asterisk indicates P < 0.05. Error bars are representative of standard error of the mean over 10 beads.*

The Prime 95B's outperformance of the Delta Evolve 512 was unexpected because EMCCD based detectors have traditionally offered higher signal to noise performance over sCMOS detectors. Since we were imaging bright fluorescent beads, it is possible that the EM gain of the Delta Evolve 512 was of no benefit at these light levels. At these brightness levels, the camera read noise of the Prime 95B was insignificant whilst the noise in the Delta Evolve 512 was seemingly amplified by its gain. Through direct comparison between the two cameras, we decided that the sCMOS, Prime 95B would be the better choice of detector for the setup as it provided high SBR at higher framerates.

5.3.2 Optimising frame rate of sCMOS for photon burst detection

To capture the same molecule multiple times as it diffused freely through a detection volume, very high framerates were required. Multiple detections of the same molecules over adjacent frames were also required to process data and identify photon bursts. These are detected within freely diffusing smFRET experiments. Here, when a molecule passes through an illumination laser spot, multiple photons are released as the fluorophores attached to the molecule fluoresce. The detection of these photons is typically performed with single photon avalanche diode (SPAD) detectors. These detectors are sensitive enough to record individual photons as they arrive at the detector. A sliding window burst search algorithm is then used to identify the presence of a fluorophore within the confocal detection volume (Fries et al. 1998). This algorithm features a time window *T* which is incrementally moved along. Time points are identified when a number of photons exceeding a

threshold (photon burst) are found within this window. Our system did not use a SPAD detector, instead opting for our sCMOS camera (Prime95B, Photometrics). This discrepancy presented a challenge when applying a similar burst search algorithm due to the predetermined frame rate of the sCMOS camera. Unlike single photon detectors, sCMOS detectors function by accumulating the charge of incident photons within their pixel arrays over a period of exposure. The accumulated charge on each pixel is then read out and digitised providing an intensity reading. A complete cycle of exposure and readout is termed a frame, with the number of completed frames per second (fps) termed the frame rate. To emulate the temporal sensitivity of SPAD detectors, the frame rate of the sCMOS needed to be maximised. This would ensure that molecules diffusing through a detection volume were captured over multiple frames, making it possible to apply a burst search style algorithm. The operating parameters of the Prime95B were therefore adjusted and tested with the aim of maximising the overall frame rate.

5.3.2.1 Reducing exposure time to increase frame rate

The frame rate of the sCMOS camera was increased significantly by reducing the exposure time of each frame. Exposure time is the period during a frame in which charge is accumulated on the pixels of the detector as photons are detected. The sum of this charge determines the intensity of the pixel for that frame, with longer exposures allowing for a greater number of photons to be collected, typically resulting in a greater signal to background. By reducing the period of exposure, the time taken to complete a frame was greatly reduced, achieving a maximum frame rate of 2700 fps for a 300x300 pixel array when the exposure time was set to 0.3 ms (**Figure 45**). The frame rate did not increase for exposure times below 0.3 ms, meaning that at this point the frame rate was limited by the rate at which the charge from each pixel row could be read out, termed a readout limited frame rate.

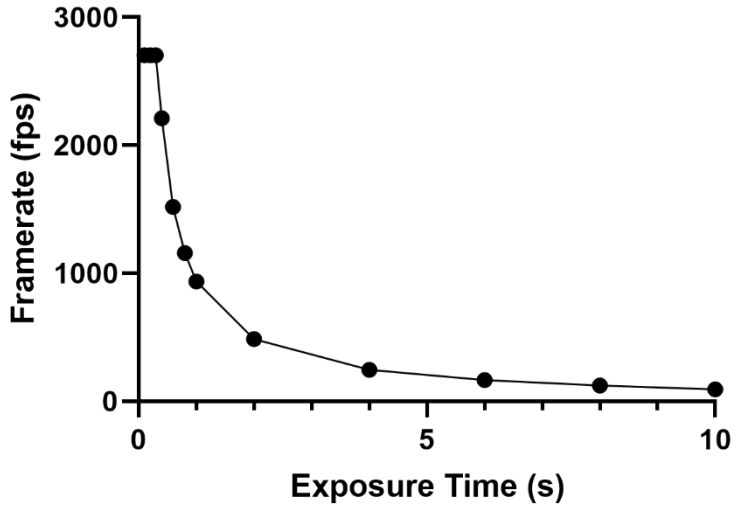

Figure 45. Exposure time dependence of frame rate for sCMOS camera. *The frame rate of a Prime95B camera was measured whilst using varying exposure times. The pixel array size was kept constant at 300x300 pixels. Single gain mode was used throughout. No errors present due to this being a single run. Framerate was determined using Micromanager inbuilt fps live output.*

5.3.2.2 Changing gain mode increases frame rate

Pixel based detectors, including sCMOS, use pre-set gain settings to determine the full-well capacity and sensitivity of the detector. The sCMOS camera had the option of two gain modes, combined gain (16-bit) and single gain (12-bit) output. Combined gain offered a larger full-well capacity and superior noise performance due to its lower read noise. However, there were advantages to using the single gain mode when imaging freely diffusing molecules within the same pixel over multiple frames. When operated in this mode, the camera reads the accumulated charge of two pixel rows simultaneously, effectively halving the time to read the entire pixel array. This meant that the single gain mode could achieve double the frame rate of the combined gain mode within readout limited conditions. For this reason, the single gain output was used exclusively throughout this part of the project.

5.3.2.3 Reducing number of pixel rows increases frame rate

The time taken to readout an entire pixel array is dependent on the total number of pixel rows. By reducing the total number of pixel rows, the overall frame rate was substantially increased (**Figure 46**). Reducing the number of active pixel rows posed the disadvantage of a reduced observation area but was the only way the highest frame rates could be accessed. Since readout time was the same per pixel row, regardless of the number of pixels in the row, all the pixel array columns were kept active. This resulted in a narrow detection area which was far wider than it was tall, like a horizontal letterbox.

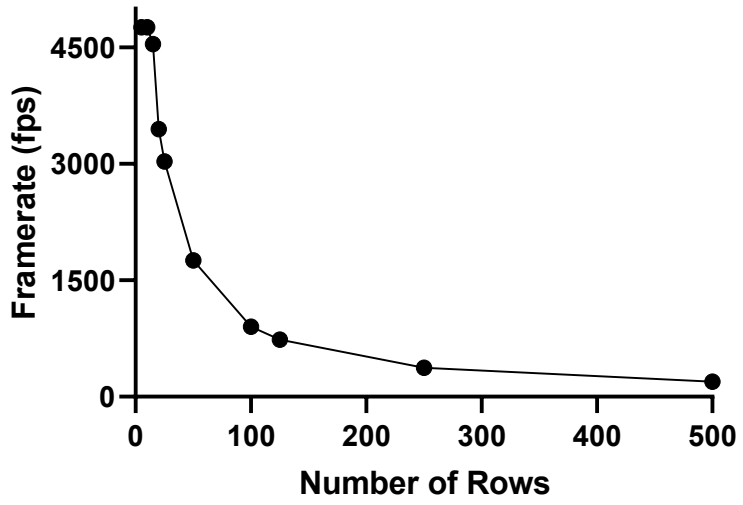

Figure 46. Active pixel row-dependence of Prime95B overall frame rate. *Higher frame rates were achieved by reducing the number of pixel rows which had to be read-out. Exposure time was set to 0.1 ms. No errors present due to this being a single run. Framerate was determined using Micromanager inbuilt fps live output.*

5.3.3 Detection of individual fluorescent beads

Fluorescent beads were diluted in deuterium-depleted water (DDW) to prevent overcrowding of the microscope field of view and prevent the occurrence of multiple beads inhabiting the same pixel over a single frame. The bead sample was flowed into an empty flow cell and imaged using TIRF microscopy. The fluorescent beads used had a diameter of 100 nm and emitted in green when excited with 488 nm laser light. The beads were visible when diffusing through the evanescent illumination field adjacent to the top surface of the flow cell. The aim of these tests was to establish whether (i) individual beads could be observed at very low exposure times, (ii) the beads diffused within the evanescent field over multiple frames.

Varying exposure times were used to acquire time lapse images of the diffusing beads in TIRFM. Within the burst detection program, bead videos were analysed to measure the average intensity of detected beads. A minimum intensity threshold of twice the maximum background level was used to identify signals originating from diffusing beads. The average intensity of detected photon bursts emitted by the beads dropped with a reduction in the exposure time of the sCMOS (**Figure 47**). This was due to a reduced number of photons collected by the detector during each individual frame, caused by fluorescence emission being split over several frames (**Figure 48**).

The second aim required that diffusing beads be captured over multiple frames. The program determined the first and last arrival time of each detected burst, allowing the burst duration in frames to be calculated. An optimal frame rate of 0.6 ms was observed to detect bursts over the largest number of frames (**Figure 49**). Lower exposure times did not yield enough burst detections

due to very low emission signals which did not exceed the intensity threshold. Higher frame rates all produced about the same burst duration (27 frames, 16.2 ms), eluding to the detection of the same stationary background elements instead of new molecules diffusing into focus.

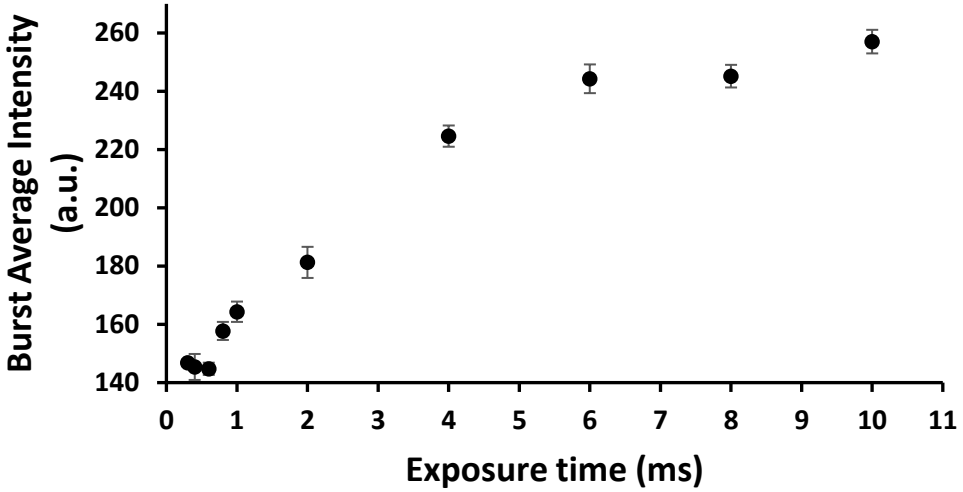

Figure 47. Average intensity of bursts is dependent on sCMOS exposure time. *Green fluorescent beads were imaged freely diffusing in a flow cell chamber using TIRFM with varying exposure times.*

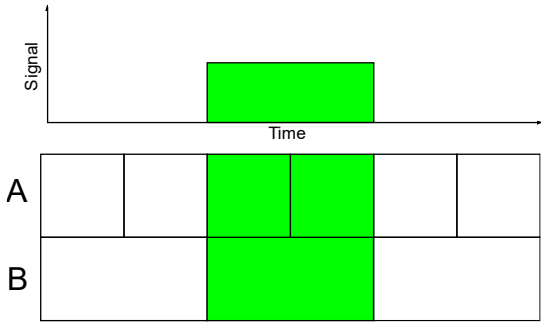

Figure 48. Splitting of intensity over adjacent frames. *The emission signal is divided over multiple frames when fluorescence is captured over multiple frames. This produces a less bright image (A) than if the entire emission is captured within an individual frame (B).*

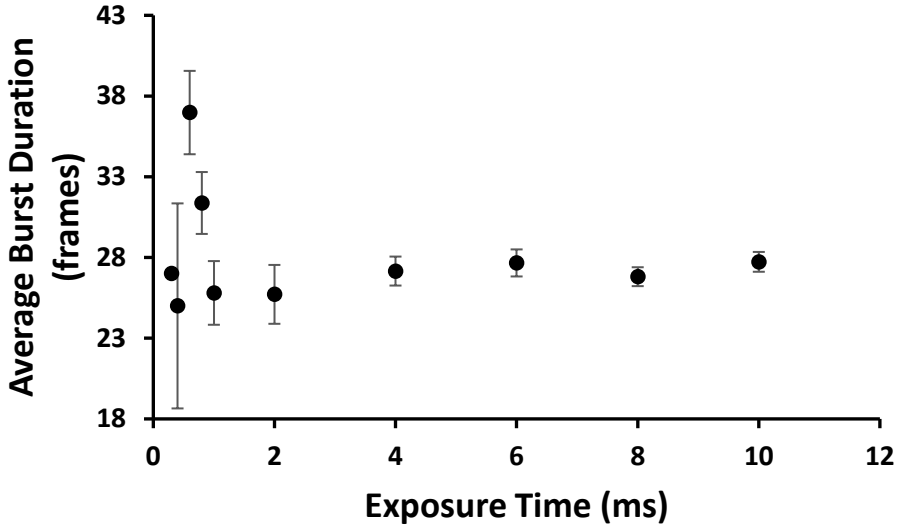

Figure 49. Average number of frames over which a burst is detected is dependent on exposure time of sCMOS. *Fluorescent beads were imaged under TIRFM using varying exposure times. The program calculated the average retention time of beads within the detection volume. All errors are standard error of the mean. Exposure times of 0.3 ms yielded a single burst, meaning that an error bar was not attainable. Greater exposure times increased the number of detected bursts, reducing the standard error, starting with 3 detections at 0.4 ms and ending with 409 detection at 10 ms exposure.*

5.3.4 Optimising Cy5-DNA detection

The TIRF setup had so far proved capable of detecting fluorescent beads freely diffusing within the evanescent field over multiple frames. It now needed to be tested for its ability to detect fluorescence originating from more biologically relevant molecules tagged with dyes commonly used in single molecule fluorescence microscopy. Short DNA fragments labelled with Cy5 dye were imaged, freely diffusing in solution. Cy5 emits in the far-red when excited with a 633 nm laser (**Figure 50**). The red channel of the microscope, which was originally specified to work with Alexa 647 dye, would allow Cy5 to be imaged without the need to change the filter setup. Testing the viability of imaging fluorophore dyes at higher frame rates was performed by direct excitation of the Cy5-labelled DNA strands using a 633 nm fibre-coupled laser. A notch filter was used to block the excitation laser line from the detector. A filter cube containing an emission filter (ET655LP, Chroma) and a dichroic mirror (ZT488/640rpc, Chroma) were used to block background light and aid detection of Cy5 emission signals.

Cy5 is one half of the commonly used Cy3-Cy5 donor-acceptor fluorophore pair, the emission spectrum of which is shown in **Figure 50**. During FRET experiments, Cy3 is commonly excited by a 532 nm laser line. This energy is transferred *via* FRET to Cy5, which then proceeds to emit in the far-red. Our setup did not feature a suitable laser line for the excitation of Cy3.

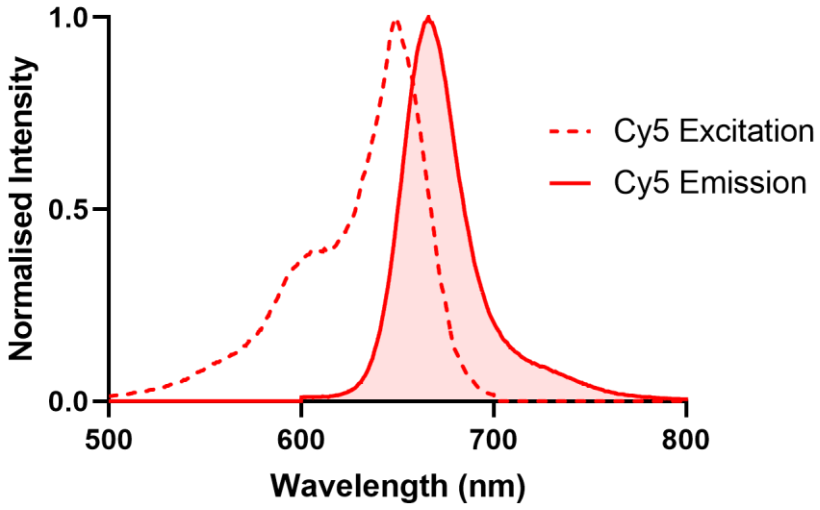

Figure 50. Excitation and emission spectra of Cy5. *Cy5 has an excitation peak (red dashed) at 651 nm, and an emission peak (red solid) at 655 nm.*

5.3.4.1 Improving signal intensity through increased retention time

300 pM Cy5 dye-labelled DNA fragments were flowed into a flow cell and imaged using TIRFM. Analysis of image stacks revealed that very few Cy5 molecules detections were being made, with few to no detections made at exposure times shorter than 10 ms. To increase the number of detections, changes to the system were made to maximise the potential retention time of molecules passing through the detection volume. This would maximise the emission signal detected within a single pixel, instead of splitting the signal over numerous detection volumes. DNA measuring 147 bp was replaced with longer 232 bp DNA. This was theorised to slow the molecules' diffusion within the evanescent field, since larger objects diffuse at reduced velocities. No difference in the average retention time was observed for the longer DNA compared to the shorter strands. In a further to decrease the velocity of the molecules, glycerol was added to the imaging buffer to increase the viscosity of the medium. The concentration of glycerol was ultimately limited to under 30%, since greater concentrations than this caused an increase in background noise of the sample. The increase in retention time was negligible within solutions containing up to and including 30% glycerol.

5.3.4.2 Improving signal intensity using oxygen scavengers and antifade

To increase the signal emitted by Cy5 molecules, laser power was increased up to its maximum of 48 mW. Higher laser powers increase the rate of photon emission from fluorophores, increasing the signal obtained by each frame. This was however unsuccessful due to the undesired side effect of accelerating the rate of fluorophore photobleaching. The fluorescence properties of the Cy5 fluorophores therefore had to be improved to withstand these higher laser powers. This would allow

access to the higher emission signals, whilst maximising their fluorescence lifespan before becoming permanently photobleached.

To improve the performance of Cy5 fluorophores whilst imaging at very high frame rates and increased laser power, oxygen scavengers and antifade components were added to the imaging buffer. 300 pM Cy5-DNA (232 bp) was diluted in buffer containing glucose oxidase (100 nM), catalase (1.5 µM) and Trolox (1.5 mM). Trolox, an antioxidant which reduces oxidative stress on fluorophores was used to reduce the rate of permanent photobleaching of Cy5 (Cordes et al. 2009). The addition of Trolox reduced the rate of Cy5 blinking. This was attributed to the ability of Trolox to suppress the occurrence of long-lived dark states which occur over millisecond time-scales by quenching fluorophore triplet-states (Rasnik et al. 2006). Reactions between fluorophores and molecular oxygen present within imaging buffer can damage fluorophores. Glucose oxidase and catalase (GODCAT) was added to the buffer to remove molecular oxygen from the system, reducing the potential for oxidisation of dyes (Aitken et al. 2008). It does this by oxidising glucose, removing molecular oxygen from the solution. The addition of these components allowed for the detection of individual Cy5 dyes as they diffused through the illumination volume. The effect of the GODCAT was an increased signal emitted by Cy5 at low exposures, making the fluorophores detectable at exposure times as low as 1 ms when illuminated using the maximum laser power of 48 mW (**Figure 51**). Sub-millisecond exposures produced negligible detections, meaning 1 ms was the lowest exposure which could be used when imaging the Cy5-DNA with the current setup. Observation of these stacks showed that Cy5-DNA molecules only occupied an illuminated pixel area for a maximum of 2 frames, even at exposures low as 1 ms. Unfortunately, this meant it would be impossible to detect molecules over more frames than this.

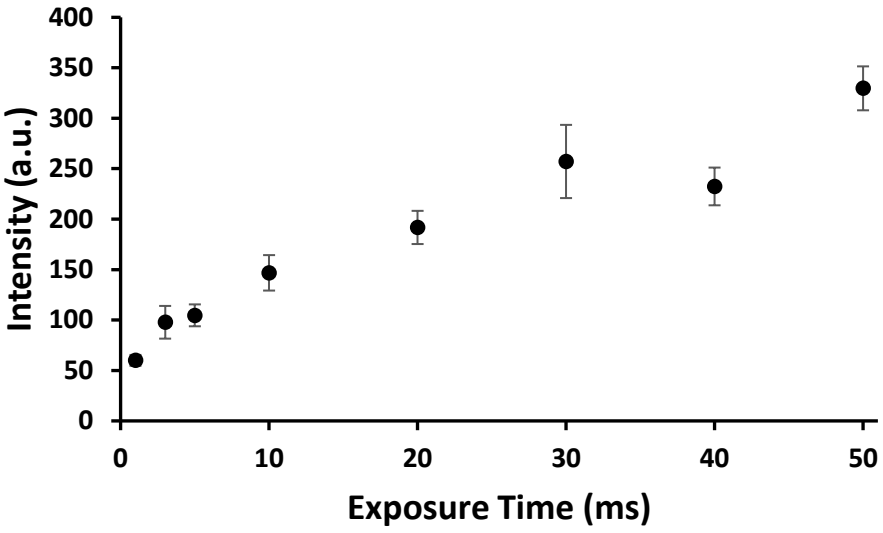

Figure 51. Mean intensity of detected Cy5 molecule is dependent on duration of exposure. *Short strands of DNA labelled with Cy5, freely diffusing in buffer containing Trolox and GODCAT, were imaged using different lengths of camera exposure. The mean intensities were calculated over the intensities of 10 Cy5 molecules near the centre of the microscope field of view to allow for even illumination. Intensities were measured in ImageJ using the line profile tool to identify the peak intensity of each DNA strand. The average background for each exposure (measured by averaging the intensity of a 20x20 pixel area containing no fluorophores) was subtracted from the DNA intensities. The background subtracted intensities were mean averaged. Laser power was kept constant at 48 mW throughout. Error bars represent standard error from the mean of 10 measured intensities.*

Using the burst detection program, a threshold was set to detect signals that exceeded a level of 1.5x the background. This threshold was specific to each image stack, to compensate for the lower peak intensities when imaging with shorter exposure times. A minimal sliding window length corresponding to a single frame was used due to the limited retention time of fluorophores within the detection volume. Reducing the exposure time from 50 ms to 10 ms resulted in fewer detected molecules (**Figure 52**). At exposure times below 10 ms, the relationship between number of detections and exposure time disappeared. This was due to the degraded signal-to-noise at these short exposures preventing the program from correctly identifying photon bursts. This was evident from the reduction in the measured intensity of detected molecules with decreasing exposure time (**Figure 53**).

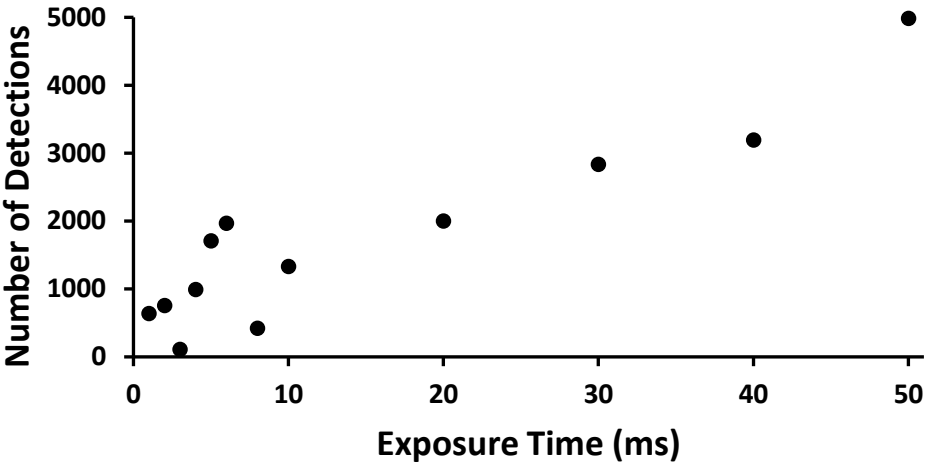

Figure 52. Number of detected Cy5 molecules by burst search program at different exposure times. *Short strands of DNA labelled with Cy5 in buffer containing Trolox and GODCAT were imaged using different lengths of camera exposure; laser power of 48 mW. Stacks consisting of 5000 frames measuring 30 x 300 pixels were analysed using the burst search program using a sliding window length of 2 frames and a minimum number of 2 detections. Intensity threshold was 1.5x the background level at each exposure (100 a.u.).*

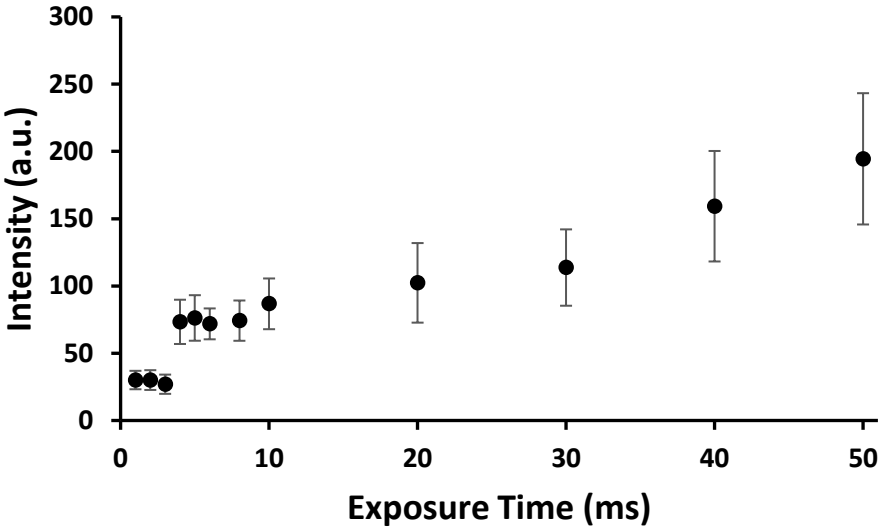

Figure 53. Average intensity of Cy5 molecules detected by burst search program at different exposure times. *Short strands of DNA labelled with Cy5 in buffer containing Trolox and GODCAT were imaged using different lengths of camera exposure; laser power of 48 mW. Stacks consisting of 5000 frames measuring 30 x 300 pixels were analysed using the burst search program using a sliding window length of 2 frames and a minimum number of 2 detections. Intensity threshold was 1.5x the background level at each exposure (100 a.u.). Mean intensities are plotted with background subtracted.*

5.4 Discussion

In this chapter, the process of optimising a prism-based TIRF microscope for high-throughput detection of in solution single molecules is described. I envisioned the removal of constraints imposed by surface tethering whilst maintaining the benefit of high-throughput measurements related to wide-field microscopy. Imaging of freely diffusing Cy5-DNA revealed that the TIRFM setup could detect individual molecules in solution, but this was largely limited by the number of photons

which could be collected during very short exposure times. An inability to retain molecules within the detection volume for long enough to perform accurate intensity measurements was also observed. Both factors are discussed below, as well as potential improvements which can be made to the system and other techniques which can be implemented into its design.

5.4.1 Using an sCMOS instead of EMCCD

The use of an sCMOS camera over the more traditional EMCCD is a departure from typical single molecule microscope builds. The signal to background performance of the Prime 95B (sCMOS) was shown to be superior to the Delta Evolve 512 (EMCCD) when imaging fluorescent beads (**Figure 44**). The Prime 95B also operated at considerably higher framerates (70 fps with all pixel rows active) than the Delta Evolve 512. Although we did not anticipate requiring such high framerates to study the reconstitution of the ParABS system, we recognised its potential to capture systems with much faster dynamics such as freely diffusing molecules.

5.4.2 Frame rate and signal to background: a balancing act

The principle for high-frame rate detection of diffusing molecules was initially tested on fluorescent beads. I was successful in imaging these diffusing beads at frame rates approaching 1,000 fps. Imaging at these frame rates allowed for a potential temporal resolution of around 1 ms. Individual beads were captured with burst lengths of around 35 frames using these high frame rates. However, this performance was not replicated when imaging a more biologically relevant sample of Cy5-labelled DNA fragments. Here, using similarly high frame rates came at a detriment to the emission signal received by the detector. The Cy5-DNA fragments were not as bright as the fluorescent beads and were considerably smaller, causing them to diffuse in and out of detection volumes at a faster rate. Use of low exposure times therefore further reduced the number of photons captured per frame. The imaging buffer conditions were changed to include a glucose oxidase/catalase system and Trolox to maximise the fluorescence properties of a the Cy5 tags. Under these conditions, the minimum exposure time was reduced from 10 to 1 ms, allowing freely diffusing Cy-tagged molecules to be detected at around 1,000 fps.

5.4.1 Increasing molecule retention time

Upon imaging diffusing strands of DNA tagged with Cy5 molecules, it became apparent that the emission signals from the fluorescent tags were not large enough to identify accurately within the burst search program. This was due in part to the fast movement of molecules, limiting their retention time within an individual detection volume. This either caused emitted photons to be divided among adjacent detection volumes, or the molecules to drop out from the thin illumination field entirely over the course of a frame. The burst search algorithm used by the analysis program

required individual molecules to be detected over multiple, sequential frames to ascertain whether a signal was due to a diffusing fluorophore or just a random background fluctuation. To slow the diffusion of molecules, glycerol was added to increase the viscosity of the imaging medium, but this had little effect on the molecule retention time. The amount of glycerol that could be added was also limited due to its negative effect on the signal to background performance of the system, with concentrations above 30% found to interfere with the evanescent field. Other approaches have been used to confine fluorescent molecules to the imaging depth of microscopes without surface-tethering by individual labs (Leslie et al. 2010; Tyagi et al. 2014; Ruggeri et al. 2017; Fontana et al. 2019). The difficulty of implementing these techniques however varies, with some requiring the use of custom nano-fluidic devices which are either pressure driven or involve a reversible process of collapsing a microfluidic channel to smaller dimensions.

It appears that the main factor which limited retention time within the TIRF setup was the size of the detection volumes (Prime 95B pixel size; 11 µm x 11 µm = 121 μm^2). The detection volume of a standard solution-based smFRET setup consists of a diffraction limited laser spot with a volume of roughly 1 fL. This volume is sufficiently small to ensure that only a single molecule inhabits the detection volume at any given time. The detection volume for our setup was determined by the dimensions of the individual pixels of the sCMOS and the imaging lenses of the microscope. Each square pixel measured 11 μm^2. The magnification of the objective lens (100x) resulted in a 2D detection area of 110 nm^2 per pixel. The illumination depth of the evanescent wave was estimated at 100 nm, making the total detection volume attributed to each pixel equal to 11,000 nm^3 (1.21×10^{-3} fL). The detection volume of a single pixel was therefore significantly smaller than that of a conventional confocal setup. The sCMOS could use artificial pixel binning to multiply this volume by 4 times, but even this does not create a comparable volume to a confocal spot. Due to thin illumination of the evanescent wave (estimated at 100 nm), a 29x29 pixel array would be required to create a detection volume of roughly equal volume to a 1 fL diffraction limited confocal spot (**Figure 54**).

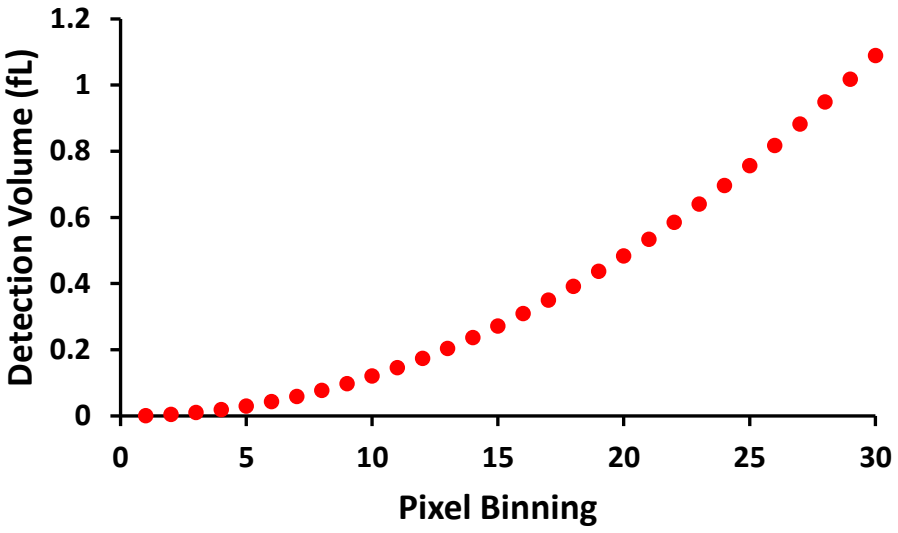

Figure 54. Total volume of detection volume using different pixel binning quantities. *The detection volume is increased by binning pixels in square arrays. The graph assumes a constant evanescent wave depth of 100 nm. Each pixel measures 11 µm² and accounts for an area of 110 nm² through the microscope's 100x objective lens.*

5.4.2 Parallel detection of diffusing molecules using sCMOS

Inspired by the use of an EMCCD pixel array to multiplex fluorescence correlation spectroscopy (FCS) measurements (Kannan et al. 2006), an algorithm was created which treated each pixel on a sCMOS detector (Prime95B) as a separate detection volume. Molecule detections were made as particles diffused across the pixel area and within the TIRF illumination volume. Single-molecule FRET (smFRET) setups have used multiple detection volumes in a similar way to maximise the rate at which measurements are carried out. The main bottleneck present in confocal solution-based smFRET setups is the single diffraction-limited illumination volume which limits intensity measurements to one at a time. This method suffers from a very low throughput since many individual measurements must be made in series before a statistically significant population of molecules has been gathered. Setups have been developed which use custom SPAD arrays and specialised optics to simply multiply the number of confocal illumination volumes generated within the imaging medium (Ingargiola et al. 2012; Ingargiola et al. 2018). These methods are still only adopted by labs which specialise in the development of new imaging techniques. A new technique however called solution wide-field imaging (SWiFi) has been shown to produce high-throughput FRET measurements of freely diffusing molecules by adapting an existing objective-TIRF microscope (Gilboa et al. 2019). This technique utilises highly inclined thin illumination to produces an excitation volume within the imaging medium. This illumination scheme provides a middle ground between the high signal-to-noise of TIRF and the large penetration depth of epi-illumination. Perhaps the most important outcome of this system is the increased accessibility to single-molecule FRET. Groups can

retrofit their current imaging systems and relieves the need for highly sensitive, photon counting detectors and high numerical aperture objectives.

5.4.3 Next steps towards smFRET

Just as an objective-TIRF microscope can be adapted into a system capable of in solution smFRET (Gilboa et al. 2019), I believe the prism-TIRF system I have described throughout this chapter could also be modified to perform smFRET experiments. There are, however, several challenges which must be overcome before this can happen. Firstly, due to the limited variety of excitation lasers within our TIRF setup, excitation of Cy3 (donor) dyes was not possible. Instead, Cy5 (acceptor) was excited directly using a 633 nm laser line. For a functioning FRET system to be built, Cy3 would need to be included along with a laser for its excitation (**Figure 55**). An emission splitter would then separate the emission signals collected from Cy3 and Cy5 onto two distinct channels. The pixels from each emission channel would then need to be paired together, providing two intensity readings for each detection volume. Coincidental burst detections within the same frame and pixel pair could then be used to verify the presence of a diffusing molecule. The program could then calculate the ratio between the measured donor and acceptor intensities to determine the FRET efficiency of molecules diffusing through the detection volume.

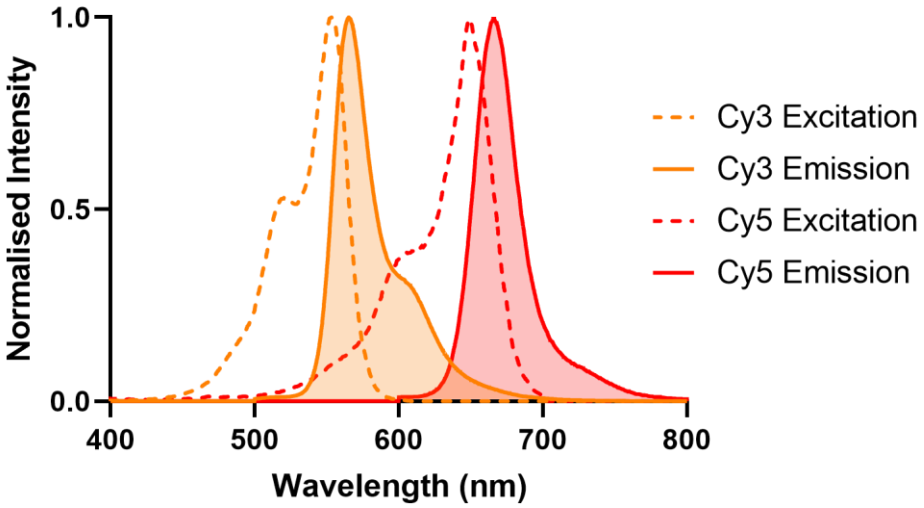

Figure 55. Excitation and emission spectra of Cy3-Cy5 FRET pair. *Cy3 has an excitation peak (orange dashed) at 532 nm, and an emission peak (orange solid) at 568 nm. The long emission tail of Cy3 optimally excites Cy5 (red dashed), which emits in the far-red end of the spectrum with an emission peak at 655 nm (red solid).*

Typical solution-based smFRET setups use single photon detectors that are sensitive enough to record and timestamp individual emitted photons. These timestamped photons are analysed using a sliding window burst search method that detects clusters of photons arriving within a short time to determine when a molecule has diffused through the illumination volume. Our program relied on a

similar burst search algorithm and attempted to recreate the temporal resolution of a single photon detector by maximising the frame rate of a sCMOS detector. For this program to accurately the intensities of Cy3 and Cy5 molecules over multiple frames, the retention time of molecules must be increased, and the brightness of tagged fluorophores maximised.

Chapter 6

General discussion and future directions

6.1 Imaging biological mechanisms outside of the cell

In chapter 2, I setup up a custom total internal reflection fluorescence microscope to visualise the partition protein interactions of *V. cholerae* chromosome II, to better understand bacterial chromosome segregation. The microscope was developed with a specification similar to systems used in the successful reconstitutions of F and P1 plasmid partitioning (Hwang et al. 2013; Vecchiarelli et al. 2013; Vecchiarelli, Neuman, et al. 2014). The microscope featured multi-colour imaging, single molecule sensitivity, magnetic trapping, and compatibility with microfluidics; all of which were used to directly image the interactions which occurred between components of the chromosomal partitioning system.

Microfluidic flowcells were created and used extensively throughout the imaging experiments carried out within this project. These were necessary to allow the conditions of samples to be altered during the imaging process whilst using a prism TIRF geometry. The interior surfaces of these flowcells were coated in a uniform layer of DNA by immobilising DNA molecules to the glass surface through biotin-neutravidin interactions on a lipid-bilayer. The DNA binding activity of fluorescent molecules, such as the ParA2-GFP used in this study, could then be monitored through TIRF microscopy. The thin illumination volume of the evanescent wave exclusively excited molecules which had bound to the DNA carpet, allowing the bound proportion of molecules to be quantified. The same DNA carpet method was later used to mimic the nucleoid surface for the reconstitution of the ParABS system of *V. cholerae* chromosome II.

6.2 The role of ParA–DNA binding in chromosome segregation

ParA2 is the ATPase component of the ParABS system of *V. cholerae* chromosome II. The ATPase has the role of providing the energy for translocation of the chromosome origin. A diffusion-ratchet based mechanism for the directed motion of *V. cholerae* chromosome II partition complexes ascertains that ParA2 must bind to DNA through non-specific interactions. These interactions allow the partition complex to attach itself to the nucleoid and use it as a surface on which to move through the cell. In chapter 3, I have characterised ParA2's affinity for non-specific DNA binding.

Direct observation of ATPase-DNA binding was carried out using a fluorescent homolog, ParA2-GFP, and visualising its interaction with a uniform layer of DNA within a microfluidic flowcell. ParA2-GFP was observed to bind to DNA only in the presence of ATP, agreeing with previous *in vitro* assays which studied DNA affinity in relation to nucleotide binding (Hui et al. 2010). ParA2-GFP had to be preincubated with ATP prior to flow to maximise the overall binding intensity, suggesting that transition to the correct DNA binding conformation is not instantaneous. A non-hydrolysable ATP

homolog, ATPγS was also shown to activate the DNA binding activity of ParA2-GFP with a binding rate comparable to ATP associated ParA2-GFP. Previous studies on other plasmid ParA homologs have shown that ATPγS has varying effects on the DNA binding activity of the ParA ATPase component, with some not supporting binding at all and some producing moderate binding dependent on environmental factors (Vecchiarelli et al. 2010; Hwang et al. 2013; Vecchiarelli et al. 2013). The impact of ParB on ParA-ATPγS binding was not measured during this project, so it is unknown whether the presence of the adapter protein alters the rate at which the ATPase binds DNA. Strikingly, our results showed that ParA2 does not bind DNA in the presence of ADP or with no nucleotide. This contrasts previous results from EM studies where ParA2 was shown bind to DNA with ATP, ADP and on its own (Hui et al. 2010).

FRAP was used to study the rebinding dynamics of ATP associated ParA2-GFP to a DNA carpet. ATPase was observed to rebind the DNA carpet with two distinct time constants. ParB was shown to increase the time taken for ParA2-GFP to repopulate the bleached area. This hints at ParB's stabilisation effect on ParA-DNA binding. Further evidence for ParB stabilisation was found when ParA was observed to dissociate from the DNA carpet at a slower initial rate when the adapter protein was added to wash buffer. The additional stabilisation provided by ParB could help explain how the partition complex of chromosome II intermittently anchors itself to the nucleoid surface. Assuming movement through a diffusion ratchet mechanism, this would allow the partition complex to form a sufficiently steep concentration gradients of ParA to facilitate directed motion. Previous studies have shown that ParA2 polymerises to form higher order structures, but these were not observed throughout the course of our experiments (Hui et al. 2010). These results together suggest that ParA2 drives chromosome segregation through a diffusion ratchet-based mechanism.

6.3 *V. cholerae* chromosome segregation is based on diffusion-ratchet mechanism

In chapter 4, I visualised through TIRFM interactions which occur between ParA2, ParB2 and *parS2* on a DNA carpet. Although these experiments are the first to demonstrate that chromosomal ParA is removed from DNA in the presence of a partition complex to form depletion zones, no directed motion was observed during these experiments. There are various reasons that our experimental setup did not exhibit directed motion, a few of which are discussed within this section.

6.3.1 Factors involved in formation of partition complexes

In vivo, ParB binds specifically to the *parS* centromere-like site within DNA. Additional binds around this site and spreads over adjacent DNA. The higher-order structure assembled at this location is known as a partition complex, and is thought to be essential to the process of DNA segregation (Baxter and Funnell 2014), The reconstitution relied on the formation of partition complexes on the

surface of *parS* coated magnetic beads. This was performed by preincubating beads coated in DNA containing a *parS* site with ParB for 15 min prior to infusion into a flowcell. The presence of *parS* DNA on the surface of the beads was verified by a Cy5 tag associated with the end of each *parS* DNA strand. The heterogeneity of depletion zone depths surrounding different ParB2/*parS2* beads and the varying levels of ParA2-GFP colocalising with the beads suggested that different densities of partition complexes formed on the surface of the beads. Since ParA depletion zones were only observed when beads were preincubated with a high concentration of ParB (40 µm), there may have been issues with partitioning complex formation even if beads were sufficiently coated in *parS* DNA. A functioning fluorescent variant of ParB variant would therefore be an invaluable tool for quantifying the concentration of ParB proteins on the beads. In addition, a fluorescent ParB variant would free up the Cy5-tagged end of the *parS* DNA strand used within these experiments, allowing for it to be attached to the bead with a second biotin molecule. The result would be DNA loops along the surface of the bead which may accumulate ParB dimers differently to the single end attached strands. This hypothesis is based on the recent finding that ParB is a CTPase, which closes in a loop around the *parS* site, and subsequently spreads onto adjacent DNA (Jalal et al. 2020).

Although ParA2-GFP depletion zones were observed to surround ParB2 coated beads, the cause of these depletion zones remains unclear. Did the presence of ParB2/*parS* complexes on the beads trigger hydrolysis of ParA2-GFP causing its dissociation or was ParA2-GFP merely blocked from rebinding. An interesting experiment to test this would be to construct a ParA2-GFP mutant which was unable to hydrolyse ATP. If depletion zones still formed when using this mutant, we could safely say that ParB2's ability to trigger hydrolysis is not the primary cause of ParA2-GFP depletion from the DNA substrate.

6.3.2 The role of DNA elasticity as a scaffold for chromosome segregation

Within the diffusion-ratchet model, the partition complex at the chromosome origin intermittently binds and dissociates with the nucleoid as it moves from its initial position of replication to its fully segregated position. For this reason, the nucleoid has been described as a scaffold over which segregation occurs (Vecchiarelli et al. 2012). Perhaps the reason for the lack of directed movement lies with the composition of the DNA-carpet. Computational modelling of chromosome segregation in *C. crescentus* has shown that directed movement of the partition complex is only achieved when the elastic movement of the nucleoid structure is present (Lim et al. 2014; Surovtsev, Campos, et al. 2016). The DNA-relay model which arose out of these simulations is based on previous diffusion-ratchet models, but with the addition of DNA movement within the nucleoid scaffold. In this model, the partition complex is passed between regions of ParA bound to the nucleoid. The constant movement of the underlying nucleoid structure causes the partition complex to move with direction

through the cell. The DNA carpet used for the reconstitution attempts in this work comprised of small fragments of DNA roughly 1 kb in length. To test the effects of underlying nucleoid structure on the movement of chromosomal partition complexes, different lengths of DNA could be used to form the DNA carpet used within the reconstitution experiments.

6.3.3 Replicating the interior conditions of the cell

To reconstitute the dynamics of chromosome segregation, we required a method to recreate the environment within which partition complexes move through inside the cell. The DNA carpet setup used within our experiments was chosen due to its successful implementation in the reconstitution of plasmid ParABS systems. Within these studies, the DNA carpet mimicked the nucleoid surface which was hypothesized as the platform over which plasmid segregation occurred. The nucleoid within a bacterium is largely comprised of the chromosome. If we apply the same theory that chromosomes use the nucleoid as a surface over which to facilitate their segregation, we are implying that the chromosome pull itself along its own structure. This contrasts the plasmid model, where two separate DNA bodies interact. A more realistic representation of the environment in which chromosome segregation occurs therefore would be a non-static DNA surface which is receptive to the movement of the partition complex. This of course is far more technically challenging to achieve.

As the field of chromosome segregation has progressed, observations of partition complex segregation occurring within the nucleoid structure have been made (Le Gall et al. 2016). This means that our current 2D setup with partition complexes interacting with a flat plane of DNA may not be recreating the environment conductive to directed motion. Instead, it could be useful to recreate the nucleoid by producing a 3-dimensional DNA structure within a flowcell, and image partition complexes within the volume of the DNA. A setup which mimics the nucleoid could not be imaged with TIRFM and would require a different method of microscopy that allows for observation deeper into the sample medium, such as light sheet microscopy (Keller et al. 2008).

A more obvious next step to ensure the correct conditions would be to conduct live cell experiments. Experiments using the same ParA2-GFP proteins within live-cells could provide a better indication of how Par proteins interact. More interesting insights could be found by placing chromosomal *parS* sites on plasmids and see if chromosomal ParA is able to segregate these smaller DNA molecules successfully. This would help determine whether Par systems from chromosomes can be used to segregate other DNA molecules. Future work should involve live cell experiments so comparisons can be made between the dynamics seen *in vivo* and *in vitro*, helping to build a fuller picture of the mechanisms which drive chromosome segregation.

6.4 Improving single-molecule detection of freely diffusing molecules using TIRFM

In chapter 5, I developed a new in solution single molecule fluorescence detect technique with multiplexing capabilities, based on TIRF microscopy. Using an sCMOS camera and TIRF microscope, I identified and measured the intensity of fluorescent beads and small DNA strands tagged with Cy5 as they diffused through detection volumes defined by the dimensions of individual pixels. The basis for this optimisation was to circumvent the problems presented by surface immobilisation of proteins.

A program was created to analyse image stacks of diffusing fluorophores. The program recognised molecules which diffused into the detection volume as a series of frames where the measured intensity was above a set threshold. This “burst search” style analysis is derivative of the method used to identify molecules in confocal smFRET (Eggeling et al. 1998). For this method to work, the diffusing molecules needed to be retained within a single pixel volume for multiple frames. To increase molecule retention time, glycerol was included in the imaging medium to increase viscosity and therefore decrease the velocity of diffusing fluorophores. This was shown to be ineffective since altering the conditions of the imaging medium increased the detected background noise.

One area of spectroscopy which I predict could benefit from this work is smFRET. With only a single diffraction limited detection volume, typical in solution smFRET experiments must acquire measurements over a long time before a statistically relevant number of observations are made. Parallel detection of multiple molecules is already performed using TIRF microscopy, but this is limited to surface immobilised molecules. By using a pixel array detector coupled with the thin illumination of TIRF microscopy, multiple detection volumes can be created, allowing for parallel detection of freely diffusing molecules. Provided further development, I predict that a TIRF microscope setup capable of performing in solution smFRET would be of great use to the imaging community. The behaviour of many biological molecules is altered when they are immobilised to a surface. This setup would relieve the need for surface immobilisation whilst maintaining a higher throughput compared to confocal solution-based smFRET. Additionally, due to the use of pixel-based detectors within the technique, expensive SPAD detectors would not be needed.

6.5 Does the diffusion ratchet model apply to other Partition systems?

This project furthers the understanding of bacterial DNA segregation by exploring the ParABS system of *V. cholerae* chromosome II. The imaging and *in vitro* reconstitution techniques used within this work could be applied to study the mechanisms of other known ParABS systems, including those from chromosomes of other bacterial species. A logical step would be the study of the larger,

chromosome of *V. cholerae* which displays a very different segregation choreography to that of chromosome II. Chromosome I undergoes asymmetric segregation, with one origin remaining fixed in place at the old pole of the cell, whilst the other origin copy makes its way to the opposite pole. This would allow for direct comparisons between the ParABS systems of the two chromosomes of *V. cholerae*, which could lead to greater understanding of the reasons behind their differing mechanisms of segregation. I foresee that the method of reconstitution outlined within this project could be used to study the segregation of cellular cargos beyond DNA. Recent work has shown that a similar diffusion-ratchet mechanism is involved in the distribution of carbon-fixing organelles within cyanobacteria (Maccready et al. 2018). Dedicated partition machinery has also been identified to mediate the segregation of chromosomes in archaea (Kalliomaa-Sanford et al. 2012). These segregation systems feature a ParA motor protein which contains a Walker motif, just like the ATPase encoded for by bacterial ParABS systems (Schumacher et al. 2015). The ParB component encoded for in these systems is unique to archaea, but shows structural similarity to Centromere protein A (CENP-A), a component that is required for correct segregation of chromosomes in eukaryotes (Quénet and Dalal 2012). It is therefore apparent that the partition systems present on archaeal chromosomes are a hybrid of those found in bacteria and eukaryotes (Barillà 2016). Further research into chromosome segregation in archaea may provide a unifying picture of DNA partitioning across the three-domains of life.

References

Abeles AL, Friedman SA, Austin SJ. 1985. Partition of unit-copy miniplasmids to daughter cells. III. The DNA sequence and functional organization of the P1 partition region. J Mol Biol. 185(2):261–72. doi:10.1016/0022-2836(85)90402-4.

Abrahamsson S, Chen J, Hajj B, Stallinga S, Katsov AY, Wisniewski J, Mizuguchi G, Soule P, Mueller F, Darzacq CD, et al. 2013. Fast multicolor 3D imaging using aberration-corrected multifocus microscopy. Nat Methods. 10(1):60–63. doi:10.1038/NMETH.2277.

Adachi S, Hori K, Hiraga S. 2006. Subcellular positioning of F plasmid mediated by dynamic localization of SopA and SopB. J Mol Biol. 356(4):850–863. doi:10.1016/j.jmb.2005.11.088.

Ai HW, Henderson JN, Remington SJ, Campbell RE. 2006. Directed evolution of a monomeric, bright and photostable version of Clavularia cyan fluorescent protein: Structural characterization and applications in fluorescence imaging. Biochem J. 400(3):531–540. doi:10.1042/BJ20060874.

Aitken CE, Marshall RA, Puglisi JD. 2008. An oxygen scavenging system for improvement of dye stability in single-molecule fluorescence experiments. Biophys J. 94(5):1826–1835. doi:10.1529/biophysj.107.117689.

Akhtar P, Anand SP, Watkins SC, Khan SA. 2009. The tubulin-like RepX protein encoded by the pXO1 plasmid forms polymers in vivo in bacillus anthracis. J Bacteriol. 191(8):2493–2500. doi:10.1128/JB.00027-09.

Ali M, Nelson AR, Lopez AL, Sack DA. 2015. Updated global burden of cholera in endemic countries. PLoS Negl Trop Dis. 9(6). doi:10.1371/journal.pntd.0003832.

Allen PB, Milne G, Doepker BR, Chiu DT. 2010. Pressure-driven laminar flow switching for rapid exchange of solution environment around surface adhered biological particles. Lab Chip. 10(6):727–733. doi:10.1039/b919639k.

Anand SP, Akhtar P, Tinsley E, Watkins SC, Khan SA. 2008. GTP-dependent polymerization of the tubulin-like RepX replication protein encoded by the pXO1 plasmid of Bacillus anthracis. Mol Microbiol. 67(4):881–890. doi:10.1111/j.1365-2958.2007.06100.x.

Austin SJ, Abeles AL. 1983a. Partition of unit-copy miniplasmids to daughter cells. II. The partition region of miniplasmid P1 encodes an essential protein and a centromere-like site at which it acts. J Mol Biol. 169(2):373–87. doi:10.1016/S0022-2836(83)80056-4.

Austin SJ, Abeles AL. 1983b. Partition of unit-copy miniplasmids to daughter cells. I. P1 and F miniplasmids contain discrete, interchangeable sequences sufficient to promote equipartition. J Mol Biol. 169(2):353–72. doi:10.1016/S0022-2836(83)80055-2.

Austin SJ, Mural RJ, Chattoraj DK, Abeles AL. 1985. Trans- and Cis-acting elements for the replication of P1 miniplasmids. J Mol Biol. 183(2):195–202. doi:10.1016/0022-2836(85)90212-8.

Autret S, Nair R, Errington J. 2001. Genetic analysis of the chromosome segregation protein SPoOj of Bacillus subtilis: Evidence for separate domains involved in DNA binding and interactions with SOj protein. Mol Microbiol. 41(3):743–55. doi:10.1046/j.1365-2958.2001.02551.x.

Axelrod D. 1981. Cell-substrate contacts illuminated by total internal reflection fluorescence. J Cell Biol. 89(1):141–145. doi:10.1083/jcb.89.1.141.

Axelrod D, Koppel DE, Schlessinger J, Elson E, Webb WW. 1976. Mobility measurement by analysis of fluorescence photobleaching recovery kinetics. Biophys J. 16(9):1055–1069. doi:10.1016/S0006-3495(76)85755-4.

Aylett CHS, Löwe J. 2012. Superstructure of the centromeric complex of TubZRC plasmid partitioning systems. Proc Natl Acad Sci U S A. 109(41):16522–16527. doi:10.1073/pnas.1210899109.

Aylett CHS, Wang Q, Michie KA, Amos LA, Löwe J. 2010. Filament structure of bacterial tubulin homologue TubZ. Proc Natl Acad Sci USA. 107(46):19766–71. doi:10.1073/pnas.1010176107. http://www.pubmedcentral.nih.gov/articlerender.fcgi?artid=2993389&tool=pmcentrez&rendertype=abstract.

Barillà D. 2016. Driving Apart and Segregating Genomes in Archaea. Trends Microbiol. 24(12):957–967. doi:10.1016/j.tim.2016.07.001.

Barillà D, Rosenberg MF, Nobbmann U, Hayes F. 2005. Bacterial DNA segregation dynamics mediated by the polymerizing protein ParF. EMBO J. 24(7):1453–64. doi:10.1038/sj.emboj.7600619. http://www.pubmedcentral.nih.gov/articlerender.fcgi?artid=1142544&tool=pmcentrez&rendertype=abstract.

Bartosik AA, Lasocki K, Mierzejewska J, Thomas CM, Jagura-Burdzy G. 2004. ParB of Pseudomonas aeruginosa: Interactions with its partner ParA and its target parS and specific effects on bacterial growth. J Bacteriol. 186(20):6983–6998. doi:10.1128/JB.186.20.6983-6998.2004.

Batt SM, Bingle LEH, Dafforn TR, Thomas CM. 2009. Bacterial Genome Partitioning: N-Terminal Domain of IncC Protein Encoded by Broad-Host-Range Plasmid RK2 Modulates Oligomerisation and DNA Binding. J Mol Biol. 385(5):1361–1374. doi:10.1016/j.jmb.2008.12.016.

Baxter JC, Funnell BE. 2014. Plasmid Partition Mechanisms. Microbiol Spectr. 2(6):1–20. doi:10.1128/microbiolspec.PLAS-0023-2014. http://www.ncbi.nlm.nih.gov/pubmed/26104442.

Bernard R, Marquis KA, Rudner DZ. 2010. Nucleoid occlusion prevents cell division during replication fork arrest in Bacillus subtilis. Mol Microbiol. 78(4):866–882. doi:10.1111/j.1365-2958.2010.07369.x.

Bouet J-Y, Ah-Seng Y, Benmeradi N, Lane D. 2007. Polymerization of SopA partition ATPase: Regulation by DNA binding and SopB. Mol Microbiol. 63(2):468–81. doi:10.1111/j.1365-2958.2006.05537.x.

Bouet J-Y, Funnell BE. 1999. P1 ParA interacts with the P1 partition complex at parS and an ATP-ADP switch controls ParA activities. EMBO J. 18(5):1415–24. doi:10.1093/emboj/18.5.1415. http://www.pubmedcentral.nih.gov/articlerender.fcgi?artid=1171231&tool=pmcentrez&rendertype=abstract.

Bowman GR, Comolli LR, Zhu J, Eckart M, Koenig M, Downing KH, Moerner WE, Earnest T, Shapiro L. 2008. A Polymeric Protein Anchors the Chromosomal Origin/ParB Complex at a Bacterial Cell Pole. Cell. 134(6):945–955. doi:10.1016/j.cell.2008.07.015.

Breier AM, Grossman AD. 2007. Whole-genome analysis of the chromosome partitioning and sporulation protein Spo0J (ParB) reveals spreading and origin-distal sites on the Bacillus subtilis chromosome. Mol Microbiol. 64(3):703–718. doi:10.1111/j.1365-2958.2007.05690.x.

Britton RA, Lin DCH, Grossman AD. 1998. Characterization of a prokaryotic SMC protein involved in chromosome partitioning. Genes Dev. 12(9):1254–1259. doi:10.1101/gad.12.9.1254.

Broedersz CP, Wang X, Meir Y, Loparo JJ, Rudner DZ, Wingreen NS. 2014. Condensation and localization of the partitioning protein ParB on the bacterial chromosome. Proc Natl Acad Sci USA. 111(24):8809–8814. doi:10.1073/pnas.1402529111.

Brooks AC, Hwang LC. 2017. Reconstitutions of plasmid partition systems and their mechanisms. Plasmid. 91:37–41. doi:10.1016/j.plasmid.2017.03.004.

Cambridge J, Blinkova A, Magnan D, Bates D, Walker JR. 2014. A Replication-inhibited unsegregated

nucleoid at mid-cell blocks Z-ring formation and cell division independently of SOS and the SlmA nucleoid occlusion protein in Escherichia coli. J Bacteriol. 196(1):36–49. doi:10.1128/JB.01230-12.

Campbell RE, Tour O, Palmer AE, Steinbach PA, Baird GS, Zacharias DA, Tsien RY. 2002. A monomeric red fluorescent protein. Proc Natl Acad Sci USA. 99(12):7877–7882. doi:10.1073/pnas.082243699.

Chalfie M, Tu Y, Euskirchen G, Ward WW, Prasher DC. 1994. Green fluorescent protein as a marker for gene expression. Science (80-). 263(5148):802–805. doi:10.1126/science.8303295.

Chen Y, Erickson HP. 2008. In vitro assembly studies of FtsZ/tubulin-like proteins (TubZ) from Bacillus plasmids: Evidence for a capping mechanism. J Biol Chem. 283(13):8102–8109. doi:10.1074/jbc.M709163200.

Cordes T, Vogelsang J, Tinnefeld P. 2009. On the mechanism of trolox as antiblinking and antibleaching reagent. J Am Chem Soc. 131(14):5018–5019. doi:10.1021/ja809117z.

Cormack BP, Valdivia RH, Falkow S. 1996. FACS-optimized mutants of the green fluorescent protein (GFP). In: Gene. p. 33–38.

Davey MJ, Funnell BE. 1994. The P1 plasmid partition protein ParA. A role for ATP in site-specific DNA binding. J Biol Chem. 269(47):29908–29913.

Davis MA, Martin KA, Austin SJ. 1992. Biochemical activities of the ParA partition protein of the P1 plasmid. Mol Microbiol. 6(9):1141–1147. doi:10.1111/j.1365-2958.1992.tb01552.x.

Debaugny RE, Sanchez A, Rech J, Labourdette D, Dorignac J, Geniet F, Palmeri J, Parmeggiani A, Boudsocq F, Anton Leberre V, et al. 2018. A conserved mechanism drives partition complex assembly on bacterial chromosomes and plasmids. Mol Syst Biol. 14(11):e8516. doi:10.15252/msb.20188516.

Deniz AA, Dahan M, Grunwell JR, Ha T, Faulhaber AE, Chemla DS, Weiss S, Schultz PG. 1999. Single-pair fluorescence resonance energy transfer on freely diffusing molecules: observation of Förster distance dependence and subpopulations. Proc Natl Acad Sci USA. 96(7):3670–5. doi:10.1073/pnas.96.7.3670. http://www.pubmedcentral.nih.gov/articlerender.fcgi?artid=22352&tool=pmcentrez&rendertype=abstract.

Dubarry N, Pasta F, Lane D. 2006. ParABS systems of the four replicons of Burkholderia cenocepacia: New chromosome centromeres confer partition specificity. J Bacteriol. 188(4):1489–1496. doi:10.1128/JB.188.4.1489-1496.2006.

Dunham TD, Xu W, Funnell BE, Schumacher MA. 2009. Structural basis for ADP-mediated transcriptional regulation by P1 and P7 ParA. EMBO J. 28(12):1792–1802. doi:10.1038/emboj.2009.120.

Ebersbach G, Briegel A, Jensen GJ, Jacobs-Wagner C. 2008. A Self-Associating Protein Critical for Chromosome Attachment, Division, and Polar Organization in Caulobacter. Cell. 134(6):956–968. doi:10.1016/j.cell.2008.07.016.

Ebersbach G, Gerdes K. 2001. The double par locus of virulence factor pB171: DNA segregation is correlated with oscillation of ParA. Proc Natl Acad Sci USA. 98(26):15078–15083. doi:10.1073/pnas.261569598.

Ebersbach G, Gerdes K. 2004. Bacterial mitosis: Partitioning protein ParA oscillates in spiral-shaped structures and positions plasmids at mid-cell. Mol Microbiol. 52(2):385–398. doi:10.1111/j.1365-2958.2004.04002.x.

Ebersbach G, Gerdes K. 2005. Plasmid Segregation Mechanisms. Annu Rev Genet. 39(1):453–479. doi:10.1146/annurev.genet.38.072902.091252.

http://www.annualreviews.org/doi/abs/10.1146/annurev.genet.38.072902.091252.

Ebersbach G, Ringgaard S, Møller-Jensen J, Wang Q, Sherratt DJ, Gerdes K. 2006. Regular cellular distribution of plasmids by oscillating and filament-forming para ATPase of plasmid pB171. Mol Microbiol. 61(6):1428–1442. doi:10.1111/j.1365-2958.2006.05322.x.

Echazarreta MA, Klose KE. 2019. Vibrio flagellar synthesis. Front Cell Infect Microbiol. 9(131). doi:10.3389/fcimb.2019.00131.

Edelstein AD, Amodaj N, Hoover K, Vale R, Stuurman N. 2010. Computer control of microscopes using μManager. Curr Protoc Mol Biol.:14.20.1–14.20.17. doi:10.1002/0471142727.mb1420s92.

Edelstein AD, Tsuchida MA, Amodaj N, Pinkard H, Vale RD, Stuurman N. 2014. Advanced methods of microscope control using μManager software. J Biol Methods. 1(2):e10. doi:10.14440/jbm.2014.36.

Eggeling C, Fries JR, Brand L, Günther R, Seidel CAM. 1998. Monitoring conformational dynamics of a single molecule by selective fluorescence spectroscopy. Proc Natl Acad Sci USA. 95(4):1556–1561. doi:10.1073/pnas.95.4.1556.

Van den Ent F, Møller-Jensen J, Amos LA, Gerdes K, Löwe J. 2002. F-actin-like filaments formed by plasmid segregation protein ParM. EMBO J. 21(24):6935–6943. doi:10.1093/emboj/cdf672.

Erdmann N, Petroff T, Funnell BE. 1999. Intracellular localization of P1 ParB protein depends on ParA and parS. Proc Natl Acad Sci USA. 96(26):14905–14910. doi:10.1073/pnas.96.26.14905.

Errington J, Murray H, Ling JW. 2005. Diversity and redundancy in bacterial chromosome segregation mechanisms. Philos Trans R Soc B Biol Sci. 360(1455):497–505. doi:10.1098/rstb.2004.1605.

Felsovalyi F, Patel T, Mangiagalli P, Kumar SK, Banta S. 2012. Effect of thermal stability on protein adsorption to silica using homologous aldo-keto reductases. Protein Sci. 21:1113–1125. doi:10.1002/pro.2099.

Fiebig A, Keren K, Theriot JA. 2006. Fine-scale time-lapse analysis of the biphasic, dynamic behaviour of the two Vibrio cholerae chromosomes. Mol Microbiol. 60(5):1164–1178. doi:10.1111/j.1365-2958.2006.05175.x.

Fink G, Löwe J. 2015. Reconstitution of a prokaryotic minus end-tracking system using TubRC centromeric complexes and tubulin-like protein TubZ filaments. Proc Natl Acad Sci USA. 112(15):E1845-50. doi:10.1073/pnas.1423746112. http://www.pubmedcentral.nih.gov/articlerender.fcgi?artid=4403160&tool=pmcentrez&rendertype=abstract.

Fisher GLM, Pastrana CL, Higman VA, Koh A, Taylor JA, Butterer A, Craggs T, Sobott F, Murray H, Crump MP, et al. 2017. The structural basis for dynamic DNA binding and bridging interactions which condense the bacterial centromere. Elife. doi:10.7554/eLife.28086.

Fogel MA, Waldor MK. 2005. Distinct segregation dynamics of the two Vibrio cholerae chromosomes. Mol Microbiol. 55(1):125–136. doi:10.1111/j.1365-2958.2004.04379.x.

Fogel MA, Waldor MK. 2006. A dynamic, mitotic-like mechanism for bacterial chromosome segregation. Genes Dev. 20(23):3269–3282. doi:10.1101/gad.1496506.

Fontana M, Fijen C, Lemay SG, Mathwig K, Hohlbein J. 2019. High-throughput, non-equilibrium studies of single biomolecules using glass-made nanofluidic devices. Lab Chip. 19(1):79–86. doi:10.1039/c8lc01175c.

Förster T. 1960. Transfer Mechanisms of Electronic Excitation Energy. Radiat Res Suppl. 2:326–339. doi:10.2307/3583604.

Fries JR, Brand L, Eggeling C, Köllner M, Seidel CAM. 1998. Quantitative identification of different single molecules by selective time-resolved confocal fluorescence spectroscopy. J Phys Chem A. 102(33):6601–6613. doi:10.1021/jp980965t.

Funnell BE. 2016. ParB partition proteins: Complex formation and spreading at bacterial and plasmid centromeres. Front Mol Biosci. 3:44. doi:10.3389/fmolb.2016.00044.

Le Gall A, Cattoni DI, Guilhas B, Mathieu-Demazière C, Oudjedi L, Fiche J-B, Rech J, Abrahamsson S, Murray H, Bouet J, et al. 2016. Bacterial partition complexes segregate within the volume of the nucleoid. Nat Commun. in press(May):1–10. doi:10.1038/ncomms12107.

Garner EC, Campbell CS, Mullins RD. 2004. Dynamic instability in a DNA-segregating prokaryotic actin homolog. Science. 306(5698):1021–5. doi:10.1126/science.1101313. http://science.sciencemag.org/content/306/5698/1021.abstract.

Garner EC, Campbell CS, Weibel DB, Mullins RD. 2007. Reconstitution of DNA segregation driven by assembly of a prokaryotic actin homolog. Science. 315(5816):1270–4. http://www.ncbi.nlm.nih.gov/pubmed/17332412%5Cnhttp://www.pubmedcentral.nih.gov/articlerender.fcgi?artid=PMC2851738.

Gayathri P, Fujii T, Møller-Jensen J, Van den Ent F, Namba K, Löwe J. 2012. A bipolar spindle of antiparallel ParM filaments drives bacterial plasmid segregation. Science (80-). 338(6112):1334–1337. doi:10.1126/science.1229091.

Gerdes K, Moller-Jensen J, Jensen RB. 2000. Plasmid and chromosome partitioning: Surprises from phylogeny. Mol Microbiol. 37(3):455–466. doi:10.1046/j.1365-2958.2000.01975.x.

Gilboa B, Jing B, Cui TJ, Sow M, Plochowietz A, Mazumder A, Kapanidis AN. 2019. Confinement-Free Wide-Field Ratiometric Tracking of Single Fluorescent Molecules. Biophys J. 117(11):2141–2153. doi:10.1016/j.bpj.2019.10.033.

Gitai Z, Thanbichler M, Shapiro L. 2005. The choreographed dynamics of bacterial chromosomes. Trends Microbiol. 13(5):221–228. doi:10.1016/j.tim.2005.03.006.

Glaser P, Sharpe ME, Raether B, Perego M, Ohlsen K, Errington J. 1997. Dynamic, mitotic-like behavior of a bacterial protein required for accurate chromosome partitioning. Genes Dev. 11(9):1160–1168. doi:10.1101/gad.11.9.1160.

Godfrin-Estevenon AM, Pasta F, Lane D. 2002. The parAB gene products of Pseudomonas putida exhibit partition activity in both P. putida and Escherichia coli. Mol Microbiol. 43(1):39–49. doi:10.1046/j.1365-2958.2002.02735.x.

Gordon S, Rech J, Lane D, Wright A. 2004. Kinetics of plasmid segregation in Escherichia coli. Mol Microbiol. 51(2):461–469. doi:10.1046/j.1365-2958.2003.03837.x.

Gordon S, Sitnikov D, Webb CD, Teleman AA, Straight A, Losick R, Murray AW, Wright A. 1997. Chromosome and low copy plasmid segregation in E. coli: Visual evidence for distinct mechanisms. Cell. 90(6):1113–1121. doi:10.1016/S0092-8674(00)80377-3.

Graceffa P, Dominguez R. 2003. Crystal structure of monomeric actin in the ATP state: Structural basis of nucleotide-dependent actin dynamics. J Biol Chem. 278(36):34172–80. doi:10.1074/jbc.M303689200.

Graham TGW, Wang X, Song D, Etson CM, van Oijen AM, Rudner DZ, Loparo JJ. 2014. ParB spreading requires DNA bridging. Genes Dev. 28(11):1228–1238. doi:10.1101/gad.242206.114.

Graumann PL, Losick R, Strunnikov A V. 1998. Subcellular localization of Bacillus subtilis SMC, a protein involved in chromosome condensation and segregation. J Bacteriol. 180(21):5749–5755.

doi:10.1128/jb.180.21.5749-5755.1998.

Han Y-W, Mizuuchi K. 2010. Phage Mu Transposition Immunity: Protein Pattern Formation along DNA by a Diffusion-Ratchet Mechanism. Mol Cell. doi:10.1016/j.molcel.2010.06.013.

Harms A, Treuner-Lange A, Schumacher D, Søgaard-Andersen L. 2013. Tracking of Chromosome and Replisome Dynamics in Myxococcus xanthus Reveals a Novel Chromosome Arrangement. PLoS Genet. 9(9):e1003802. doi:10.1371/journal.pgen.1003802.

Hatano T, Yamaichi Y, Niki H. 2007. Oscillating focus of SopA associated with filamentous structure guides partitioning of F plasmid. Mol Microbiol. 64(5):1198–1213. doi:10.1111/j.1365-2958.2007.05728.x.

Heidelberg JF, Elsen JA, Nelson WC, Clayton RA, Gwinn ML, Dodson RJ, Haft DH, Hickey EK, Peterson JD, Umayam L, et al. 2000. DNA sequence of both chromosomes of the cholera pathogen Vibrio cholerae. Nature. 406(6795):477–483. doi:10.1038/35020000.

Hirano T. 1999. SMC-mediated chromosome mechanics: A conserved scheme from bacteria to vertebrates? Genes Dev. 13(1):11–19. doi:10.1101/gad.13.1.11.

Holmes VF, Cozzarelli NR. 2000. Closing the ring: Links between SMC proteins and chromosome partitioning, condensation, and supercoiling. Proc Natl Acad Sci USA. 97(4):1322–1324. doi:10.1073/pnas.040576797.

Hoshino S, Hayashi I. 2012. Filament formation of the FtsZ/tubulin-like protein TubZ from the Bacillus cereus pXO1 plasmid. J Biol Chem. 287(38):32103–32112. doi:10.1074/jbc.M112.373803.

Hu L, Vecchiarelli AG, Mizuuchi K, Neuman KC, Liu J. 2015. Directed and persistent movement arises from mechanochemistry of the ParA/ParB system. Proc Natl Acad Sci USA. 112(51):E7055–E7064. doi:10.1073/pnas.1505147112. http://www.pnas.org/content/112/51/E7055%5Cnhttp://www.ncbi.nlm.nih.gov/pubmed/26647183%5Cnhttp://www.pnas.org/content/112/51/E7055.full.

Hu L, Vecchiarelli AG, Mizuuchi K, Neuman KC, Liu J. 2017. Brownian Ratchet Mechanism for Faithful Segregation of Low-Copy-Number Plasmids. Biophys J. 112(7):1489–1502. doi:10.1016/j.bpj.2017.02.039.

Hui MP, Galkin VE, Yu X, Stasiak AZ, Stasiak A, Waldor MK, Egelman EH. 2010. ParA2, a Vibrio cholerae chromosome partitioning protein, forms left-handed helical filaments on DNA. Proc Natl Acad Sci USA. 107(10):4590–5. doi:10.1073/pnas.0913060107. http://www.pnas.org/content/107/10/4590.abstract.

Hwang LC, Vecchiarelli AG, Han Y-W, Mizuuchi M, Harada Y, Funnell BE, Mizuuchi K. 2013. ParA-mediated plasmid partition driven by protein pattern self-organization. EMBO J. 32(9):1238–1249. doi:10.1038/emboj.2013.34. http://www.ncbi.nlm.nih.gov/pubmed/23443047%5Cnhttp://emboj.embopress.org/cgi/doi/10.1038/emboj.2013.34.

Icha J, Weber M, Waters JC, Norden C. 2017. Phototoxicity in live fluorescence microscopy, and how to avoid it. BioEssays. 39(8). doi:10.1002/bies.201700003.

Ingargiola A, Colyer RA, Kim D, Panzeri F, Lin R, Gulinatti A, Rech I, Ghioni M, Weiss S, Michalet X. 2012. Parallel multispot smFRET analysis using an 8-pixel SPAD array. Proc SPIE Int Soc Opt.:8228. doi:10.1117/12.909470.

Ingargiola A, Segal M, Gulinatti A, Rech I, Labanca I, Maccagnani P, Ghioni M, Weiss S, Michalet X. 2018. 48-spot single-molecule FRET setup with periodic acceptor excitation. J Chem Phys. 148(12).

doi:10.1063/1.5000742.

Iniesta AA. 2014. ParABS system in chromosome partitioning in the bacterium Myxococcus xanthus. PLoS One. 9(1):e86897. doi:10.1371/journal.pone.0086897.

Inouye S, Tsuji FI. 1994. Aequorea green fluorescent protein. Expression of the gene and fluorescence characteristics of the recombinant protein. FEBS Lett. 341(2–3):277–280. doi:10.1016/0014-5793(94)80472-9.

Ireton K, Gunther NW, Grossman AD. 1994. spo0J is required for normal chromosome segregation as well as the initiation of sporulation in Bacillus subtilis. J Bacteriol. 176(17):5320–5329. doi:10.1128/jb.176.17.5320-5329.1994.

Jabłoński A. 1933. Efficiency of anti-stokes fluorescence in dyes. Nature. 131:839–840. doi:10.1038/131839b0.

Jacob F, Brenner S, Cuzin F. 1963. On the Regulation of DNA Replication in Bacteria. Cold Spring Harb Symp Quant Biol. 28:329–348. doi:10.1101/sqb.1963.028.01.048.

Jakimowicz D, Brzostek A, Rumijowska-Galewicz A, Zydek P, Dołzbłasz A, Smulczyk-Krawczyszyn A, Zimniak T, Wojtasz Ł, Zawilak-Pawlik A, Kois A, et al. 2007. Characterization of the mycobacterial chromosome segregation protein ParB and identification of its target in Mycobacterium smegmatis. Microbiology. 153:4050–4060. doi:10.1099/mic.0.2007/011619-0.

Jakimowicz D, Zydek P, Kois A, Zakrzewska-Czerwińska J, Chater KF. 2007. Alignment of multiple chromosomes along helical para scaffolding in sporulating Streptomyces hyphae. Mol Microbiol. 65(3):625–41. doi:10.1111/j.1365-2958.2007.05815.x.

Jalal ASB, Tran NT, Le TBK. 2020. ParB spreading on DNA requires cytidine triphosphate in vitro. Elife. 9:53515. doi:10.1101/2019.12.11.865972.

Jeppsson K, Kanno T, Shirahige K, Sjögren C. 2014. The maintenance of chromosome structure: Positioning and functioning of SMC complexes. Nat Rev Mol Cell Biol. 15(9):601–614. doi:10.1038/nrm3857.

Jun S, Wright A. 2010. Entropy as the driver of chromosome segregation. Nat Rev Microbiol. 8(8):600–607. doi:10.1038/nrmicro2391.

Kadoya R, Baek JH, Sarker A, Chattoraj DK. 2011. Participation of chromosome segregation protein ParAI of Vibrio cholerae in chromosome replication. J Bacteriol. 193(7):1504–1514. doi:10.1128/JB.01067-10.

Kalliomaa-Sanford AK, Rodriguez-Castañeda FA, McLeod BN, Latorre-Roselló V, Smith JH, Reimann J, Albers S V., Barillà D. 2012. Chromosome segregation in Archaea mediated by a hybrid DNA partition machine. Proc Natl Acad Sci USA. 109(10):3754–3759. doi:10.1073/pnas.1113384109.

Kannan B, Har JY, Liu P, Maruyama I, Ding JL, Wohland T. 2006. Electron multiplying charge-coupled device camera based fluorescence correlation spectroscopy. Anal Chem. 78(10):3444–3451. doi:10.1021/ac0600959.

Karlsson M, Ekeroth J, Elwing H, Carlsson U. 2005. Reduction of irreversible protein adsorption on solid surfaces by protein engineering for increased stability. J Biol Chem. 280:25558–25564. doi:10.1074/jbc.M503665200.

Kawalek A, Wawrzyniak P, Bartosik AA, Jagura-Burdzy G. 2020. Rules and exceptions: The role of chromosomal ParB in DNA segregation and other cellular processes. Microorganisms. 8(1). doi:10.3390/microorganisms8010105.

Kawano Y, Abe C, Kaneda T, Aono Y, Abe K, Tamura K, Terakawa S. 2000. High-numerical-aperture objective lenses and optical system improved objective type total internal reflection fluorescence microscopy. Opt Devices Diagnostics Mater Sci. 4098:142–151. doi:10.1117/12.401623.

Keller PJ, Schmidt AD, Wittbrodt J, Stelzer EHK. 2008. Reconstruction of zebrafish early embryonic development by scanned light sheet microscopy. Science (80-). 322(5904):1065–9. doi:10.1126/science.1162493.

Kemter FS, Messerschmidt SJ, Schallopp N, Sobetzko P, Lang E, Bunk B, Spröer C, Teschler JK, Yildiz FH, Overmann J, et al. 2018. Synchronous termination of replication of the two chromosomes is an evolutionary selected feature in Vibrionaceae. PLoS Genet. 14(3):e1007251. doi:10.1371/journal.pgen.1007251.

Kilgard R, Heim AB, Tsien RY. 1995. Improved green fluorescence. Nature. 373(6516):663–664. doi:10.1038/373663b0.

Kim E, Kerssemakers J, Shaltiel IA, Haering CH, Dekker C. 2020. DNA-loop extruding condensin complexes can traverse one another. Nature. 579:438–442. doi:10.1038/s41586-020-2067-5.

Kim HJ, Calcutt MJ, Schmidt FJ, Chater KF. 2000. Partitioning of the linear chromosome during sporulation of Streptomyces coelicolor A3(2) involves an oriC-linked parAB locus. J Bacteriol. 182(5):1313–1320. doi:10.1128/JB.182.5.1313-1320.2000.

Kimura K, Rybenkov V V., Crisona NJ, Hirano T, Cozzarelli NR. 1999. 13S condensin actively reconfigures DNA by introducing global positive writhe: Implications for chromosome condensation. Cell. 98(2):239–248. doi:10.1016/S0092-8674(00)81018-1.

Kirkup BC, Chang L, Chang S, Gevers D, Polz MF. 2010. Vibrio chromosomes share common history. BMC Microbiol. 10(137). doi:10.1186/1471-2180-10-137.

Kusiak M, Gapczyńska A, Płochocka D, Thomas CM, Jagura-Burdzy G. 2011. Binding and spreading of ParB on DNA determine its biological function in Pseudomonas aeruginosa. J Bacteriol. 193(13):3342–55. doi:10.1128/JB.00328-11.

Larsen RA, Cusumano C, Fujioka A, Lim-Fong G, Patterson P, Pogliano J. 2007. Treadmilling of a prokaryotic tubulin-like protein, TubZ, required for plasmid stability in Bacillus thuringiensis. Genes Dev. 21(11):1340–1352. doi:10.1101/gad.1546107.

Lau IF, Filipe SR, Søballe B, Økstad OA, Barre FX, Sherratt DJ. 2003. Spatial and temporal organization of replicating Escherichia coli chromosomes. Mol Microbiol. 49(3):731–743. doi:10.1046/j.1365-2958.2003.03640.x.

Leake MC, Chandler JH, Wadhams GH, Bai F, Berry RM, Armitage JP. 2006. Stoichiometry and turnover in single, functioning membrane protein complexes. Nature. 443:355–358. doi:10.1038/nature05135.

Lee MJ, Liu CH, Wang SY, Huang C Ter, Huang H. 2006. Characterization of the Soj/Spo0J chromosome segregation proteins and identification of putative parS sequences in Helicobacter pylori. Biochem Biophys Res Commun. 342(3):744–750. doi:10.1016/j.bbrc.2006.01.173.

Lee PS, Lin DCH, Moriya S, Grossman AD. 2003. Effects of the chromosome partitioning protein Spo0J (ParB) on oriC positioning and replication initiation in Bacillus subtilis. J Bacteriol. 185(4):1326–37. doi:10.1128/JB.185.4.1326-1337.2003.

Leonard AC, Helmstetter CE. 1988. Replication patterns of multiple plasmids coexisting in Escherichia coli. J Bacteriol. 170(3):1380–1383. doi:10.1128/jb.170.3.1380-1383.1988.

Leonard TA, Butler PJ, Löwe J. 2005. Bacterial chromosome segregation: Structure and DNA binding

of the Soj dimer - A conserved biological switch. EMBO J. 24(2):270–282. doi:10.1038/sj.emboj.7600530.

Leonard TA, Butler PJG, Löwe J. 2004. Structural analysis of the chromosome segragation protein Spo0J from Thermus thermophilus. Mol Microbiol. 53(2):419–432. doi:10.1111/j.1365-2958.2004.04133.x.

Leslie SR, Fields AP, Cohen AE. 2010. Convex lens-induced confinement for imaging single molecules. Anal Chem. 82(14):6224–6229. doi:10.1021/ac101041s.

Lesterlin C, Gigant E, Boccard F, Espéli O. 2012. Sister chromatid interactions in bacteria revealed by a site-specific recombination assay. EMBO J. 31(16):3468–79. doi:10.1038/emboj.2012.194.

Lewis RA, Bignell CR, Zeng W, Jones AC, Thomas CM. 2002. Chromosome loss from par mutants of Pseudomonas putida depends on growth medium and phase of growth. Microbiology. 148(2):537–548. doi:10.1099/00221287-148-2-537.

Li Y, Austin SJ. 2002. The P1 plasmid in action: Time-lapse photomicroscopy reveals some unexpected aspects of plasmid partition. Plasmid. 48(3):174–178. doi:10.1016/S0147-619X(02)00104-X.

Li Y, Sergueev K, Austin SJ. 2002. The segregation of the Escherichia coli origin and terminus of replication. Mol Microbiol. 46(4):985–996. doi:10.1046/j.1365-2958.2002.03234.x.

Lim GE, Derman AI, Pogliano J. 2005. Bacterial DNA segregation by dynamic SopA polymers. Proc Natl Acad Sci USA. 102(49):17658–63. doi:10.1073/pnas.0507222102. http://www.ncbi.nlm.nih.gov/pubmed/16306264%5Cnhttp://www.pubmedcentral.nih.gov/articlerender.fcgi?artid=PMC1308903.

Lim HC, Surovtsev I V., Beltran BG, Huang F, Bewersdorf J, Jacobs-Wagner C. 2014. Evidence for a DNA-relay mechanism in ParABS-mediated chromosome segregation. Elife. 2014(3):1–32. doi:10.7554/eLife.02758.

Lin DCH, Grossman AD. 1998. Identification and characterization of a bacterial chromosome partitioning site. Cell. 92(5):675–685. doi:10.1016/S0092-8674(00)81135-6.

Lin L, Osorio Valeriano M, Harms A, Søgaard-Andersen L, Thanbichler M. 2017. Bactofilin-mediated organization of the ParABS chromosome segregation system in Myxococcus xanthus. Nat Commun. 8(1):1817. doi:10.1038/s41467-017-02015-z.

Liu AP, Fletcher DA. 2009. Biology under construction: In vitro reconstitution of cellular function. Nat Rev Mol Cell Biol. 10(9):644–650. doi:10.1038/nrm2746.

Livny J, Yamaichi Y, Waldor MK. 2007. Distribution of centromere-like parS sites in bacteria: Insights from comparative genomics. J Bacteriol. 189(23):8693–8703. doi:10.1128/JB.01239-07.

Maccready JS, Hakim P, Young EJ, Hu L, Liu J, Osteryoung KW, Vecchiarelli AG, Ducat DC. 2018. Protein gradients on the nucleoid position the carbon-fixing organelles of cyanobacteria. Elife. 7:e39723. doi:10.7554/eLife.39723.

Manley S, Gillette JM, Patterson GH, Shroff H, Hess HF, Betzig E, Lippincott-Schwartz J. 2008. High-density mapping of single-molecule trajectories with photoactivated localization microscopy. Nat Methods. 5(2):155–157. doi:10.1038/nmeth.1176.

Marbouty M, Le Gall A, Cattoni DI, Cournac A, Koh A, Fiche J-B, Mozziconacci J, Murray H, Koszul R, Nollmann M. 2015. Condensin- and Replication-Mediated Bacterial Chromosome Folding and Origin Condensation Revealed by Hi-C and Super-resolution Imaging. Mol Cell. 59(4):588–602. doi:10.1016/j.molcel.2015.07.020.

Marston AL, Errington J. 1999. Dynamic movement of the ParA-like Soj protein of B. subtilis and its dual role in nucleoid organization and developmental regulation. Mol Cell. 4(5):673–682. doi:10.1016/S1097-2765(00)80378-0.

Mateo C, Palomo JM, Fernandez-Lorente G, Guisan JM, Fernandez-Lafuente R. 2007. Improvement of enzyme activity, stability and selectivity via immobilization techniques. Enzyme Microb Technol. 40:1451–1463. doi:10.1016/j.enzmictec.2007.01.018.

Mattheyses AL, Simon SM, Rappoport JZ. 2010. Imaging with total internal reflection fluorescence microscopy for the cell biologist. J Cell Sci. 123(21):3621–3628. doi:10.1242/jcs.056218.

McLeod BN, Allison-Gamble GE, Barge MT, Tonthat NK, Schumacher MA, Hayes F, Barillà D. 2017. A three-dimensional ParF meshwork assembles through the nucleoid to mediate plasmid segregation. Nucleic Acids Res. 45(6):3158–3171. doi:10.1093/nar/gkw1302.

Mitchell JS, Glowacki J, Grandchamp AE, Manning RS, Maddocks JH. 2017. Sequence-Dependent Persistence Lengths of DNA. J Chem Theory Comput. 13(4):1539–1555. doi:10.1021/acs.jctc.6b00904.

Mohl DA, Easter J, Gober JW. 2001. The chromosome partitioning protein, ParB, is required for cytokinesis in Caulobacter crescentus. Mol Microbiol. 42(3):741–755. doi:10.1046/j.1365-2958.2001.02643.x.

Mohl DA, Gober JW. 1997. Cell cycle-dependent polar localization of chromosome partitioning proteins in Caulobacter crescentus. Cell. 88(5):675–684. doi:10.1016/S0092-8674(00)91910-X.

Møller-Jensen J, Borch J, Dam M, Jensen RB, Roepstorff P, Gerdes K. 2003. Bacterial Mitosis: ParM of Plasmid R1 Moves Plasmid DNA by an Actin-like Insertional Polymerization Mechanism. Mol Cell. 12(6):1477–1487. doi:10.1016/S1097-2765(03)00451-9.

Møller-Jensen J, Jensen RB, Löwe J, Gerdes K. 2002. Prokaryotic DNA segregation by an actin-like filament. EMBO J. 21(12):3119–3127. doi:10.1093/emboj/cdf320.

Montabana EA, Agard DA. 2014. Bacterial tubulin TubZ-Bt transitions between a two-stranded intermediate and a four-stranded filament upon GTP hydrolysis. Proc Natl Acad Sci USA. 111(9):3407–12. doi:10.1073/pnas.1318339111. http://www.pubmedcentral.nih.gov/articlerender.fcgi?artid=3948286&tool=pmcentrez&rendertype=abstract.

Mori H, Kondo A, Ohshima A, Ogura T, Hiraga S. 1986. Structure and function of the F plasmid genes essential for partitioning. J Mol Biol. 192(1):1–15. doi:10.1016/0022-2836(86)90459-6.

Murray H, Ferreira H, Errington J. 2006. The bacterial chromosome segregation protein Spo0J spreads along DNA from parS nucleation sites. Mol Microbiol. 61(5):1352–1361. doi:10.1111/j.1365-2958.2006.05316.x.

Neuman KC, Nagy A. 2008. Single-molecule force spectroscopy: Optical tweezers, magnetic tweezers and atomic force microscopy. Nat Methods. 5(6):491–505. doi:10.1038/nmeth.1218.

Ni L, Xu W, Kumaraswami M, Schumacher MA. 2010. Plasmid protein TubR uses a distinct mode of HTH-DNA binding and recruits the prokaryotic tubulin homolog TubZ to effect DNA partition. Proc Natl Acad Sci USA. 107(26):11763–11768. doi:10.1073/pnas.1003817107.

Nielsen HJ, Li Y, Youngren B, Hansen FG, Austin SJ. 2006. Progressive segregation of the Escherichia coli chromosome. Mol Microbiol. 61(2):383–393. doi:10.1111/j.1365-2958.2006.05245.x.

Osorio Valeriano M, Altegoer F, Steinchen W, Urban S, Liu Y, Bange G, Thanbichler M. 2019. ParB-type DNA Segregation Proteins Are CTP-Dependent Molecular Switches. Cell. 179(7):1512–1524.

doi:10.1016/j.cell.2019.11.015.

Passot FM, Calderon V, Fichant G, Lane D, Pasta F. 2012. Centromere binding and evolution of chromosomal partition systems in the Burkholderiales. J Bacteriol. 194(13):3426–3436. doi:10.1128/JB.00041-12.

Prasher DC, Eckenrode VK, Ward WW, Prendergast FG, Cormier MJ. 1992. Primary structure of the Aequorea victoria green-fluorescent protein. Gene. 111(2):229–233. doi:10.1016/0378-1119(92)90691-H.

Pratto F, Cicek A, Weihofen WA, Lurz R, Saenger W, Alonso JC. 2008. Streptococcus pyogenes pSM19035 requires dynamic assembly of ATP-bound ParA and ParB on parS DNA during plasmid segregation. Nucleic Acids Res. 36(11):3676–3689. doi:10.1093/nar/gkn170.

Ptacin JL, Lee SF, Garner EC, Toro E, Eckart M, Comolli LR, Moerner WE, Shapiro L. 2010. A spindle-like apparatus guides bacterial chromosome segregation. Nat Cell Biol. 12(8):791–8. doi:10.1038/ncb2083. http://www.pubmedcentral.nih.gov/articlerender.fcgi?artid=3205914&tool=pmcentrez&rendertype=abstract.

Quénet D, Dalal Y. 2012. The CENP-A nucleosome: A dynamic structure and role at the centromere. Chromosom Res. 20(5):465–479. doi:10.1007/s10577-012-9301-4.

Rasmussen T, Jensen RB, Skovgaard O. 2007. The two chromosomes of Vibrio cholerae are initiated at different time points in the cell cycle. EMBO J. 26(13):3124–3131. doi:10.1038/sj.emboj.7601747.

Rasnik I, McKinney SA, Ha T. 2006. Nonblinking and long-lasting single-molecule fluorescence imaging. Nat Methods. 3(11):891–893. doi:10.1038/nmeth934.

Ringgaard S, van Zon J, Howard M, Gerdes K. 2009. Movement and equipositioning of plasmids by ParA filament disassembly. Proc Natl Acad Sci USA. 106(46):19369–74. doi:10.1073/pnas.0908347106. http://www.pubmedcentral.nih.gov/articlerender.fcgi?artid=2775997&tool=pmcentrez&rendertype=abstract.

Rodionov O, Łobocka M, Yarmolinsky M. 1999. Silencing of genes flanking the P1 plasmid centromere. Science (80-). 283(5401):546–549. doi:10.1126/science.283.5401.546.

Rodionov O, Yarmolinsky M. 2004. Plasmid partitioning and the spreading of P1 partition protein ParB. Mol Microbiol. 52(4):1215–1223. doi:10.1111/j.1365-2958.2004.04055.x.

Romantsov T, Fishov I, Krichevsky O. 2007. Internal structure and dynamics of isolated Escherichia coli nucleoids assessed by fluorescence correlation spectroscopy. Biophys J. 92(8):2875–84. doi:10.1529/biophysj.106.095729.

Ruggeri F, Zosel F, Mutter N, Rozycka M, Wojtas M, Ozyhar A, Schuler B, Krishnan M. 2017. Single-molecule electrometry. Nat Nanotechnol. 12(5):488–495. doi:10.1038/nnano.2017.26.

Saint-Dic D, Frushour BP, Kehrl JH, Kahng LS. 2006. A parA homolog selectively influences positioning of the large chromosome origin in Vibrio cholerae. J Bacteriol. 188(15):5626–5631. doi:10.1128/JB.00250-06.

Sanchez A, Cattoni DI, Walter JC, Rech J, Parmeggiani A, Nollmann M, Bouet JY. 2015. Stochastic Self-Assembly of ParB Proteins Builds the Bacterial DNA Segregation Apparatus. Cell Syst. 1(2):163–173. doi:10.1016/j.cels.2015.07.013.

Sbalzarini IF, Koumoutsakos P. 2005. Feature point tracking and trajectory analysis for video imaging in cell biology. J Struct Biol. 151(2):182–95. doi:10.1016/j.jsb.2005.06.002.

Schumacher MA, Tonthat NK, Lee J, Rodriguez-Castañeda FA, Chinnam NB, Kalliomaa-Sanford AK, Ng IW, Barge MT, Shaw PLR, Barillà D. 2015. Structures of archaeal DNA segregation machinery reveal bacterial and eukaryotic linkages. Science (80-). 349(6252):1120–1124. doi:10.1126/science.aaa9046.

Sengupta M, Nielsen HJ, Youngren B, Austin SJ. 2010. P1 plasmid segregation: Accurate redistribution by dynamic plasmid pairing and separation. J Bacteriol. 192(5):1175–1183. doi:10.1128/JB.01245-09.

Shaner NC, Lambert GG, Chammas A, Ni Y, Cranfill PJ, Baird MA, Sell BR, Allen JR, Day RN, Israelsson M, et al. 2013. A bright monomeric green fluorescent protein derived from Branchiostoma lanceolatum. Nat Methods. 10(5):407–409. doi:10.1038/nmeth.2413.

Shebelut CW, Guberman JM, van Teeffelen S, Yakhnina AA, Gitai Z. 2010. Caulobacter chromosome segregation is an ordered multistep process. Proc Natl Acad Sci U S A. 107(32):14194–14198. doi:10.1073/pnas.1005274107.

Shimomura O, Johnson FH, Saiga Y. 1962. Extraction, Purification and Properties of Aequorin, a Bioluminescent Protein from the Luminous Hydromedusan,Aequorea. J Cell Comp Physiol. 59(3):223–239. doi:10.1002/jcp.1030590302.

Silva AJ, Benitez JA. 2016. Vibrio cholerae Biofilms and Cholera Pathogenesis. PLoS Negl Trop Dis. 10(2):e0004330. doi:10.1371/journal.pntd.0004330.

Soh YM, Davidson IF, Zamuner S, Basquin J, Bock FP, Taschner M, Veening JW, de Los Rios P, Peters JM, Gruber S. 2019. Self-organization of parS centromeres by the ParB CTP hydrolase. Science (80-). 366(6469):1129–1133. doi:10.1126/science.aay3965.

Srivastava P, Chattoraj DK. 2007. Selective chromosome amplification in Vibrio cholerae. Mol Microbiol. 66(4):1016–1028. doi:10.1111/j.1365-2958.2007.05973.x.

Stout AL, Axelrod D. 1989. Evanescent field excitation of fluorescence by epi-illumination microscopy. Appl Opt. 28(24):5237–42. doi:10.1364/ao.28.005237.

Stracy M, Lesterlin C, De Leon FG, Uphoff S, Zawadzki P, Kapanidis AN, Ha T. 2015. Live-cell superresolution microscopy reveals the organization of RNA polymerase in the bacterial nucleoid. Proc Natl Acad Sci USA. 112(32):E4390-9. doi:10.1073/pnas.1507592112.

Strunnikov A V., Jessberger R. 1999. Structural maintenance of chromosomes (SMC) proteins: Conserved molecular properties for multiple biological functions. Eur J Biochem. 263(1):6–13. doi:10.1046/j.1432-1327.1999.00509.x.

Sullivan NL, Marquis KA, Rudner DZ. 2009. Recruitment of SMC by ParB-parS Organizes the Origin Region and Promotes Efficient Chromosome Segregation. Cell. 137(4):696–707. doi:10.1016/j.cell.2009.04.044.

Surovtsev I V., Campos M, Jacobs-Wagner C. 2016. DNA-relay mechanism is sufficient to explain ParA-dependent intracellular transport and patterning of single and multiple cargos. Proc Natl Acad Sci USA. 113(46):E7268–E7276. doi:10.1073/pnas.1616118113.

Surovtsev I V., Lim HC, Jacobs-Wagner C. 2016. The Slow Mobility of the ParA Partitioning Protein Underlies Its Steady-State Patterning in Caulobacter. Biophys J. 110(12):2790–2799. doi:10.1016/j.bpj.2016.05.014.

Tan X, Mizuuchi M, Mizuuchi K. 2007. DNA transposition target immunity and the determinants of the MuB distribution patterns on DNA. Proc Natl Acad Sci USA. 104(35):13925–13929. doi:10.1073/pnas.0706564104.

http://eutils.ncbi.nlm.nih.gov/entrez/eutils/elink.fcgi?dbfrom=pubmed&id=17709741&retmode=ref&cmd=prlinks%5Cnpapers2://publication/doi/10.1073/pnas.0706564104.

Tang M, Bideshi DK, Park HW, Federici BA. 2006. Minireplicon from pBtoxis of Bacillus thuringiensis subsp. israelensis. Appl Environ Microbiol. 72(11):6948–6954. doi:10.1128/AEM.00976-06.

Taylor JA, Pastrana CL, Butterer A, Pernstich C, Gwynn EJ, Sobott F, Moreno-Herrero F, Dillingham MS. 2015. Specific and non-specific interactions of ParB with DNA: Implications for chromosome segregation. Nucleic Acids Res. 43(2):719–731. doi:10.1093/nar/gku1295.

Teleman AA, Graumann PL, Lin DCH, Grossman AD, Losick R. 1998. Chromosome arrangement within a bacterium. Curr Biol. 8(20):1102–1109. doi:10.1016/S0960-9822(98)70464-6.

Trucksis M, Michalski J, Deng YK, Kaper JB. 1998. The Vibrio cholerae genome contains two unique circular chromosomes. Proc Natl Acad Sci USA. 95(2):1464–1469. doi:10.1073/pnas.95.24.14464.

Trun NJ, Marko JF. 1998. Architecture of a bacterial chromosome. Am Soc Microsbiolgy News.

Tyagi S, Vandelinder V, Banterle N, Fuertes G, Milles S, Agez M, Lemke EA. 2014. Continuous throughput and long-term observation of single-molecule FRET without immobilization. Nat Methods. 11(3):297–300. doi:10.1038/nmeth.2809.

Val ME, Marbouty M, De Lemos Martins F, Kennedy SP, Kemble H, Bland MJ, Possoz C, Koszul R, Skovgaard O, Mazel D. 2016. A checkpoint control orchestrates the replication of the two chromosomes of Vibrio cholerae. Sci Adv. 2(4):e1501914. doi:10.1126/sciadv.1501914.

Val ME, Soler-Bistué A, Bland MJ, Mazel D. 2014. Management of multipartite genomes: The Vibrio cholerae model. Curr Opin Microbiol. 22:120–126. doi:10.1016/j.mib.2014.10.003.

Vecchiarelli AG, Han Y-W, Tan X, Mizuuchi M, Ghirlando R, Biertümpfel C, Funnell BE, Mizuuchi K. 2010. ATP control of dynamic P1 ParA-DNA interactions: A key role for the nucleoid in plasmid partition. Mol Microbiol. 78(1):78–91. doi:10.1111/j.1365-2958.2010.07314.x.

Vecchiarelli AG, Hwang LC, Mizuuchi K. 2013. Cell-free study of F plasmid partition provides evidence for cargo transport by a diffusion-ratchet mechanism. Proc Natl Acad Sci USA. 110(15):E1390-7. doi:10.1073/pnas.1302745110. http://www.ncbi.nlm.nih.gov/pubmed/23479605.

Vecchiarelli AG, Mizuuchi K, Funnell BE. 2012. Surfing biological surfaces: Exploiting the nucleoid for partition and transport in bacteria. Mol Microbiol. 86(3):513–523. doi:10.1111/mmi.12017.

Vecchiarelli AG, Neuman KC, Mizuuchi K. 2014. A propagating ATPase gradient drives transport of surface-confined cellular cargo. Proc Natl Acad Sci USA. 111(13):4880–5. doi:10.1073/pnas.1401025111. http://www.ncbi.nlm.nih.gov/pubmed/24567408%5Cnhttp://www.pubmedcentral.nih.gov/articlerender.fcgi?artid=PMC3977271.

Vecchiarelli AG, Seol Y, Neuman KC, Mizuuchi K. 2014. A moving ParA gradient on the nucleoid directs subcellular cargo transport via a chemophoresis force. Bioarchitecture. 4(4–5):154–159. doi:10.4161/19490992.2014.987581.

Viollier PH, Thanbichler M, McGrath PT, West L, Meewan M, McAdams HH, Shapiro L. 2004. Rapid and sequential movement of individual chromosomal loci to specific subcellular locations during bacterial DNA replication. Proc Natl Acad Sci U S A. 101(25):9257–9262. doi:10.1073/pnas.0402606101.

Wang Y. 2017. Spatial distribution of high copy number plasmids in bacteria. Plasmid. 91:2–8. doi:10.1016/j.plasmid.2017.02.005.

Watanabe E, Wachi M, Yamasaki M, Nagai K. 1992. ATPase activity of SopA, a protein essential for active partitioning of F plasmid. MGG Mol Gen Genet. 234(3):346–352. doi:10.1007/BF00538693.

Webb CD, Graumann PL, Kahana JA, Teleman AA, Silver PA, Losick R. 1998. Use of time-lapse microscopy to visualize rapid movement of the replication origin region of the chromosome during the cell cycle in Bacillus subtilis. Mol Microbiol. 28(5):883–892. doi:10.1046/j.1365-2958.1998.00808.x.

Webb CD, Teleman AA, Gordon S, Straight A, Belmont A, Lin DCH, Grossman AD, Wright A, Losick R. 1997. Bipolar localization of the replication origin regions of chromosomes in vegetative and sporulating cells of B. subtilis. Cell. 88(5):667–674. doi:10.1016/S0092-8674(00)81909-1.

Weiss M. 2004. Challenges and artifacts in quantitative photobleaching experiments. Traffic. 5(6):662–71. doi:10.1111/j.1600-0854.2004.00215.x.

Weiss S. 1999. Fluorescence spectroscopy of single biomolecules. Science (80-). 283(5408):1676–1683. doi:10.1126/science.283.5408.1676.

Yamaichi Y, Bruckner R, Ringgaard S, Möll A, Ewen Cameron D, Briegel A, Jensen GJ, Davis BM, Waldor MK. 2012. A multidomain hub anchors the chromosome segregation and chemotactic machinery to the bacterial pole. Genes Dev. 26(20):2348–2360. doi:10.1101/gad.199869.112.

Yamaichi Y, Fogel MA, McLeod SM, Hui MP, Waldor MK. 2007. Distinct centromere-like parS sites on the two chromosomes of Vibrio spp. J Bacteriol. 189(14):5314–5324. doi:10.1128/JB.00416-07.

Yamaichi Y, Fogel MA, Waldor MK. 2007. par genes and the pathology of chromosome loss in Vibrio cholerae. Proc Natl Acad Sci USA. 140(2):630–635. doi:10.1073/pnas.0608341104.

Yamaichi Y, Niki H. 2000. Active segregation by the Bacillus subtilis partitioning system in Escherichia coli. Proc Natl Acad Sci U S A. 97(26):14656–14661. doi:10.1073/pnas.97.26.14656.

Yamazoe M, Onogi T, Sunako Y, Niki H, Yamanaka K, Ichimura T, Hiraga S. 1999. Complex formation of MukB, MukE and MukF proteins involved in chromosome partitioning in Escherichia coli. EMBO J. 18(21):5873–5884. doi:10.1093/emboj/18.21.5873.

Yang X, Lyu Z, Miguel A, McQuillen R, Huang KC, Xiao J. 2017. GTPase activity-coupled treadmilling of the bacterial tubulin FtsZ organizes septal cell wall synthesis. Science (80-). 355(6326):744–747. doi:10.1126/science.aak9995.

Zacharias DA, Violin JD, Newton AC, Tsien RY. 2002. Partitioning of lipid-modified monomeric GFPs into membrane microdomains of live cells. Science (80-). 296(5569):913–916. doi:10.1126/science.1068539.

Zhang H, Schumacher MA. 2017. Structures of partition protein ParA with nonspecific DNA and ParB effector reveal molecular insights into principles governing Walker-box DNA segregation. Genes Dev. 31(5):481–492. doi:10.1101/gad.296319.117.

Appendix

1.1 Buffers and stock solutions

Buffer	Component	Concentration
TN1000		
	Tris pH 8.0 (Sigma)	100 mM
	NaCl (Sigma)	1 M
TN100		
	Tris pH 8.0 (Sigma)	10 mM
	NaCl (Sigma)	100 mM
TN100 + $MgCl_2$		
	Tris pH 8.0 (Sigma)	10 mM
	NaCl (Sigma)	100 mM
	$MgCl_2$ (Sigma)	10 mM
TE buffer		
	Tris-HCl pH 8.0 (Sigma)	10 mM
	EDTA (Sigma)	0.1 mM
Par buffer		
	Tris pH 7.5 (Sigma)	50 mM
	NaCl (Sigma)	100 mM
	$MgCl_2$ (Sigma)	5 mM
	Glycerol (Fisher)	10% (v/v)
Par buffer + DTT + BSA		
	Tris pH 7.5 (Sigma)	50 mM
	NaCl (Sigma)	100 mM
	$MgCl_2$ (Sigma)	5 mM
	Glycerol (Fisher)	10% (v/v)
	BSA (Sigma)	0.1 mg/mL
	DTT (Fluorochem)	1 mM
ParA2-GFP storage buffer		
	Tris pH 7.5 (Sigma)	30 mM
	NaCl (Sigma)	500 mM
	Glycerol (Fisher)	10% (v/v)
	EDTA (Sigma)	0.1 mM
	DTT (Fluorochem)	2 mM
ParB2 binding buffer		
	Tris-HCl pH 7.4 (Sigma)	50 mM
	NaCl (Sigma)	500 mM
	Glycerol (Fisher)	10% (v/v)
	BME (Gibco)	2 mM
ParB2 storage buffer		
	Tris pH 7.5 (Sigma)	20 mM
	NaCl (Sigma)	500 mM
	Glycerol (Fisher)	10% (v/v)
	EDTA (Sigma)	0.1 mM
	DTT (Fluorochem)	2 mM
Cy5-DNA imaging buffer		
	Hepes (Fisher)	20 mM
	BSA (Sigma)	0.1 mg/mL

	Glucose oxidase (Sigma)	100 nM
	Catalase (*Aspergillus niger*) (Sigma)	1.5 µM
	Glucose (Sigma)	56 mM
	Trolox (Sigma)	1.5 mM
parS Bead wash buffer		
	Tris-HCl pH 8.2 (Sigma)	10 mM
	NaCl (Sigma)	1 M
	EDTA (Sigma)	1 mM

Note: I would like to thank Satpal Choda, Alexandra Parker and Sveta Sedeinikova for the expression and purification of all proteins used within this project. Below are the protocols which they collectively performed.

1.2 BL21 Transformation

BL21 competent *E. coli* cells were thawed on ice for 10 min. 0.5 µL (60-80 ng) of plasmid DNA was added to the thawed cells, mixed gently, and incubated on ice for 30 min. Cells were heat shocked using a water bath at 42 °C for 10 s and then placed on ice for a further 5 min. 950 µL SOC medium was added to the cell mixture and incubated for 60 min at 37 °C, shaking at 250 rpm. Cells were then diluted 10-fold several times in SOC medium. 50-100 µL of each dilution was spread onto a preheated, 37 °C selection plate. Selection plates were incubated overnight at 37 °C.

1.3 ParA2-GFP-His expression

Transformed BL21 E. coli colony was picked and used to inoculate 5 mL of LB broth and antibiotic (5 µL kanamycin) for 4-5 hr incubation on a shaker at 37 °C. 4 x 100 mL LB broth with antibiotic were inoculated with 830 µL of culture and incubated at 37 °C for 2 hr on a shaker. Sample was then centrifuged at 4,000 rpm for 10 min at 4 °C and the supernatant discarded. 4 x 500 mL LB broth with antibiotic was then inoculated by resuspending the cell pellet within the media and incubated at 37 °C until OD600. Sample was then cooled and induced with 500 µL IPTG and incubated at 16 °C overnight on a shaker. Cultures were pelleted by centrifugation at 4,000 rpm for 10 min. Supernatant was subsequently removed, and cell pellets resuspended in 30-50 mL LB media in 50 mL falcon tubes. Samples were once again centrifuged at 4,000 rpm at 4 °C for 10 min and then frozen using liquid nitrogen and stored at -80 °C.

1.4 ParA2-GFP-His purification

Cells obtained from 1l culture was defrosted and suspended in 15-30 mL of buffer A (0.5 M NaCl, 50mM tris pH 8.0) and supplemented with 1 tablet of protease inhibitor. Cells were disrupted by sonication at full power on ice using a medium probe on a Soniprep 150 machine. This was

performed over three cycles, each with a duration of 20 s followed by a pause for cooling between the treatments. Cell debris was removed by centrifugation at 72000g for 10 min using JA-25-50 rotor at 24500 rpm. Supernatant fraction (cell free extract, CFE) was separated and used for purification. A total of about 170 mg of protein in CFE (estimated by method of Bradford using Bio-Rad assay with BSA as a standard) was extracted from 1 litre of cell culture.

Chromatography was performed on an AKTA purifier machine at flow rate of 5 mL/min. Protein sample was applied on a 5 mL His-Trap HP column (GE Healthcare). Unbound material was collected, and bound protein was eluted by a 50 mL gradient of imidazole from 0 to 0.5 M in buffer A. 3 mL fractions were collected. There were three protein peaks on a chromatogram eluted. 2 of the peak fractions were combined to yield 6 mL of sample, consisting of 18 mg of ParA-GFP-His. The obtained sample was diluted with water to about 30 mL to reduce salt concentration. The protein was then ran on a 6 mL ResourceQ column (GE Healthcare) at a rate of 4 mL/min, with a gradient of NaCl concentration from 0.1 to 1 M NaCl in 50 mM Tris pH 8.0. 2 mL fractions were collected. Two fractions were combined into a volume of 4 mL, yielding 10 mg of protein. The volume of the sample was reduced to 1 mL using a Viva Spin device with 30000 MWCO. Sample was applied on a 1.6x600HiLoad Superdex200 column equilibrated in buffer A. Gel filtration was performed at 1.5 mL/min flow rate. 2 mL fractions were collected. 2 peak fractions were combined and concentrated using Viva Spin to 4.1 mg/mL (4.3 mg). Spectrum was taken to estimate protein concentration at 63 µM.

1.5 ParA2-GFP His-tag cleavage

500 µL of ParA2-GFP-His (2.25 mg) was combined with 20.5 µL TEV protease and suspended in buffer (150 mM NaCl, 50 mM Tris pH 8.0) and incubated overnight at 16 °C. The protein was ran on a His-trap column to bind and remove the cleaved His-tags using His-trap buffer A (20 mM Tris pH 7.5, 20 mM Imidazole pH 7.4, 10% Glycerol, 500 mM NaCl, 2 mM BME). This was followed with a second run through the His-trap column using a His-trap buffer B (20 mM Tris pH 7.5, 1 M Imidazole pH 7.4, 10% Glycerol, 500 mM NaCl, 2 mM BME). The protein was then ran through a Superdex 10/300 in ParA buffer (50 mM Tris pH 8.0, 0.1 mM EDTA, 10% Glycerol, 500 mM NaCl, 2mM DTT) to resolve the protein precisely. Protein was stored in 40 µL aliquots at -80 °C.

1.6 ParB2-His expression

Transformed BL21 *E. coli* colony was picked and used to inoculate 5 mL of LB broth and antibiotic (2.5 µL ampicillin) and incubated overnight at 37 °C, shaking at 200 rpm. 6 x 100 mL LB broth with antibiotic were inoculated with 830 µL of culture and incubated at 37 °C for 2 hr, shaking at 200 rpm. Sample was then centrifuged at 4000 rpm for 10 min at 4 °C and the supernatant

discarded. 6 x 500 mL LB broth with antibiotic was then inoculated by resuspending the cell pellet within the media and incubated at 37 °C until OD600 (typically 2 to 3 hr). Sample was then cooled to 25 °C, induced with 500 µL IPTG and incubated at 25 °C for 4 hr, shaking at 200 rpm. 6 x 500 mL culture was centrifuged at 4000 rpm for 10 min at 4 °C. Supernatant was subsequently removed, and cell pellets resuspended in 50 mL ParB binding buffer (Tris-HCl pH 7.4, 500 mM NaCl, 10% Glycerol, 2 mM BME) in 50 mL falcon tubes. Samples were once again centrifuged at 4000 rpm at 4 °C for 10 min and then frozen using liquid nitrogen and stored at -80 °C.

1.7 ParB2-His purification

Cells obtained from 1 L culture was defrosted and suspended in 15-30 mL of buffer A (0.5 M NaCl, 50 mM tris pH 8.0). Cells were disrupted by sonication at full power on ice using a medium probe on a Soniprep 150 machine. This was performed over three cycles, each for a duration of 20 s followed by a pause for cooling between the treatments. Cell debris was removed by centrifugation at 72000 g for 10 min using JA-25-50 rotor at 24500 rpm. Supernatant fraction (cell free extract, CFE) was separated and used for purification. Total of about 30 mg of protein in CFE (estimated by method of Bradford using Bio-Rad assay with BSA as a standard) from 1 litre of cell culture. Chromatography was performed on an AKTA purifier machine at flow rate of 1.5 mL/min. Protein sample was applied on a 1 mL His-Trap HP column (GE Healthcare). Unbound material was collected and bound protein was eluted by a 15 mL gradient of imidazole from 0 to 0.35 M in buffer A. 0.5 mL fractions were collected. One main protein peak (1.4 mg) and 4 side peaks (4 mg total) were collected. Gel filtration was carried out on the main protein peak (1.4 mg) using a Superdex200 Increase column in buffer A at a flowrate of 0.5 mL/min. Fractions of 0.5 mL were collected. Estimated protein concentration of 145 µM was obtained. The combined side peaks from the His trap column were diluted in buffer (0.1 M NaCl, 50 mM MES pH 5.9) and applied on a 1 mL Resource S column at a flow rate of 2 mL/min over a 15 mL 0.1-0.7 M NaCl gradient. 0.5 mL fractions were collected. Fractions were combined and NaCl was added to 1 M and concentrated using Viva Spin.

1.8 ParB2 His-tag cleavage

Removal of His-tag was performed the same as for ParA2-GFP (see above).

1.9 smFRET code

1.9.1 Matlab burst search code

```
%Import image stack
FileTif = '20180614_1_MMStack_Pos0.ome.tif';

%Specify the degree of pixel binning
Binning = 1;

%Convert image stack to
[data,mImage,nImage,FinalImage] = ImageReader(FileTif,Binning);

%Choose 'Max' or 'Avg' for type of brightness measurement
BrightStyle = 'Avg';

%Create empty matrix and gather information on total number of pixels
lag = 100;
threshold = 4;
influence = 0;
Arrival_Threshold = 2;
BurstSummary = [];
total_pixels = mImage*nImage;

%Burst search parameters
%Number of arrival times required within sliding window
m = 5;
%Minimum intensity to be considered a signal
Intensity_Threshold = 150;
%Sliding Window Length given in frames
T = 3;

%%%%%%%%%%%%%%%%%%%%%%%%%%%%%%%%%%%%%%%%%%%%%%%%%%%%%%%%%%%%%%%%%%%%%%%%%%%%

%Create arrival times column
Measurement.Arrival_Time = data(:,1); %Removed from for-loop

%Index over each pixel in image
for Pixel_numb = 1:total_pixels

    Measurement.IntensityRaw = data(:,Pixel_numb + 1);

%Intensity Threshold check
Arrival_Times = Measurement.Arrival_Time(Measurement.IntensityRaw >=
Intensity_Threshold) + 1;

%Check if any arrival times are detected
if isempty(Arrival_Times)
    continue;
end

%Conduct burst search on arrival times
bursts = burstsearch(Arrival_Times,m,T);

%Check if any viable bursts are detected
if isempty(bursts)
    continue;
end
```

```
%Record Start and End Frames of each burst
start_times = bursts(bursts(:,1) ~= 0);
stop_times = bursts((bursts(:,2) ~= 0),2);

%Calculate total number of bursts
Tot_Pixel_Bursts = size(start_times,1);

y = Measurement.IntensityRaw;

%Create matrix which holds all bursts for current pixel
Burst_Mat = zeros(Tot_Pixel_Bursts,5);

% Enter statistics for each burst below
for Current_Burst = 1:Tot_Pixel_Bursts

        %Start and End Frames for burst
        Start = start_times(Current_Burst);
        End = stop_times(Current_Burst);

        %Calculate the average intensity of current burst
        B =
Measurement.IntensityRaw(start_times(Current_Burst):stop_times(Current_Burs
t));
        Avg_Intensity = mean(B);

        %Determine maximum intensity of current burst
        dvalues = sort(B,'descend');
        Max_Intensity = dvalues(1);

        %Determine duration of current burst
        Len = stop_times(Current_Burst) ...
            - start_times(Current_Burst);

        %Assign statistics to burst matrix
        Burst_Mat(Current_Burst, 1) = Pixel_numb;
        Burst_Mat(Current_Burst, 2) = Start;
        Burst_Mat(Current_Burst, 3) = End;
        Burst_Mat(Current_Burst, 4) = Len;
        Burst_Mat(Current_Burst, 5) = Max_Intensity;
        Burst_Mat(Current_Burst, 6) = Avg_Intensity;
        %Burst_Mat(Current_Burst, 7) = Avg_Brightness;
        %Burst_Mat(Current_Burst, 8) = diffusion;

end
        %Summarise all bursts over pixel
        BurstSummary = [BurstSummary;Burst_Mat];
End
```

1.9.2 Burst Search Algorithm

```
%Search arrival times for any bursts
function bursts = burstsearch(Arrival_Times,m,T)
 Arrival_Times = [Arrival_Times;0];
 in_burst = 0;
```

```
array = [];

    for i = 1:(length(Arrival_Times) - m + 1)
        if abs(Arrival_Times(i + m - 1) - Arrival_Times(i)) <= T
            if in_burst == 0
                in_burst = 1;
                istart = i;
            end
        elseif in_burst == 1
        in_burst = 0;
        array(i,:) =[Arrival_Times(istart) Arrival_Times(i+m-2)];
        end
    end
bursts = array;
end
```

1.10 FRET Background

1.10.1 Fluorescence resonance energy transfer (FRET)

The resolution limit in light microscopy prevents the observation of molecular interactions which typically occur on the nanometre scale. A commonly adopted technique which works around this restriction is fluorescence resonance energy transfer (FRET). FRET occurs between a compatible pair of molecules which are within 1 – 10 nm of each other. Energy is transferred from the donor fluorophore to a nearby acceptor, without emitting a photon (**Figure 56**). The efficiency of this energy transfer is dependent on the distance between the pair. The acceptor molecules itself is not required to be fluorescent, however, in most applications both the donor and acceptor are fluorophores. This makes it simple to confirm the presence of FRET by monitoring the quenching of fluorescence of the donor molecule accompanied by the increase in acceptor emission intensity. By monitoring the ratio of the emission intensities of the donor and acceptor molecules, FRET can be used to determine the distance between the pair, giving the technique its reputation as an inter-molecular ruler.

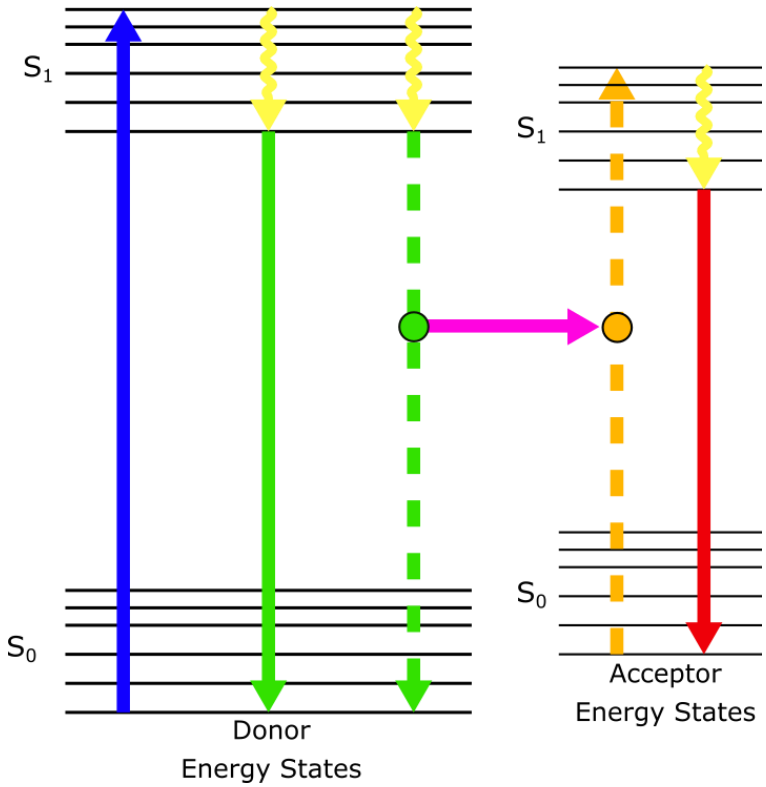

Figure 56. Jablonski Diagram of resonant energy transfer between FRET donor and acceptor molecule. *A donor molecule transitions from its ground state to a higher energy state (blue) after absorption of a photon. The molecule undergoes rapid non-radiative decay to a relaxed energy state at the bottom of the higher energy band (yellow). The molecule will then either emit a photon as it transitions back to its ground state (green solid) or transfer that energy (green dashed) to a suitable acceptor (pink). Transfer of energy from the donor to acceptor excites the acceptor molecule to a higher energy state (orange dashed). The molecule then decays to the bottom of its higher energy level, and then transitions back to its ground state (red) with the emission of a photon.*

Resonance energy transfer was originally developed by Theodore Förster, whom the theory of Förster energy transfer is named after (Förster 1960). The theory states that the efficiency of energy transfer changes with the inverse sixth power of the intermolecular distance between the FRET pair.

$$E = \frac{1}{1 + \left(\frac{r}{R_0}\right)^6}$$

Where E is the FRET efficiency, r is distance between the donor and acceptor molecules and R_0 is the Förster radius (the intermolecular distance at which energy transfer is 50%). This inverse sixth power relationship is graphically illustrated in **Figure 57**.

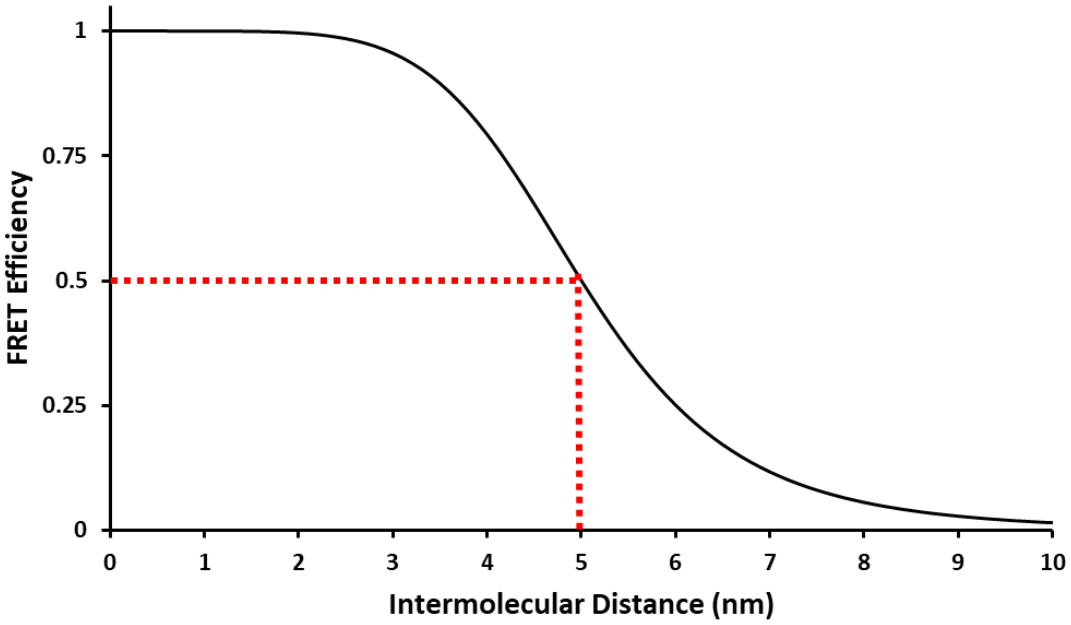

Figure 57. Efficiency of resonance energy transfer with distance between donor and acceptor fluorophores. Resonant energy transfer occurs when the distance between compatible molecule is only a few nanometres. The inverse sixth power relationship causes the FRET efficiency to rapidly drop. *The Förster radius (red) is where the intermolecular distance where the resonant energy transfer is exactly 50%.*

FRET is regularly applied in fluorescence microscopy to measure conformation changes of proteins and to monitor protein folding (Weiss 1999). Methods used to make FRET measurements are varied, but they typically follow a similar procedure. First, the sample is illuminated at a wavelength corresponding to the excitation peak of the donor fluorophore. The fluorescence intensity of both donor and acceptor molecules is then monitored to determine the proximity of the FRET pair. The closer the FRET pair, the greater the FRET efficiency, translating to a high emission signal with the acceptor detection channel.

1.10.2 FRET efficiency calculation

The FRET efficiency allows the conformation of a detected molecule to be estimated. To calculate the FRET efficiency, the intensity of two emission wavelengths from each molecule, one from the donor and one from the acceptor, need to be measured. The two emission channels can be displayed on the same pixel array using the emission splitter (Dual-View, Photometrics) of the TIRF microscope. Pixels from the donor emission channel needed to be mapped to their counterpart pixels within the acceptor emission channel. With a measured intensity from both channels, the FRET efficiency of a diffusing molecule can be estimated through the intensities of the donor and acceptor molecules.

$$E \approx \frac{I_A}{I_A + I_D}$$

Where E is the FRET efficiency, I_A is the acceptor intensity and I_D is the donor intensity.

1.10.3 Single-molecule FRET microscopy (smFRET)

Measuring the average FRET efficiency over the bulk of a sample is known as ensemble FRET. Using this technique, the distance between a FRET pair on an individual molecule is impossible to determine given a heterogeneous population of molecules (**Figure 58**). This is where the use of single-molecule FRET (smFRET) is necessary (Deniz et al. 1999). Here, the FRET efficiency of individual molecules is measured and recorded. By interrogating the FRET efficiency of individual molecules, multiple conformation states within a single sample can be detected. This includes long lived conformations as well as temporary, intermediate states that are too short lived to be detected using ensemble FRET.

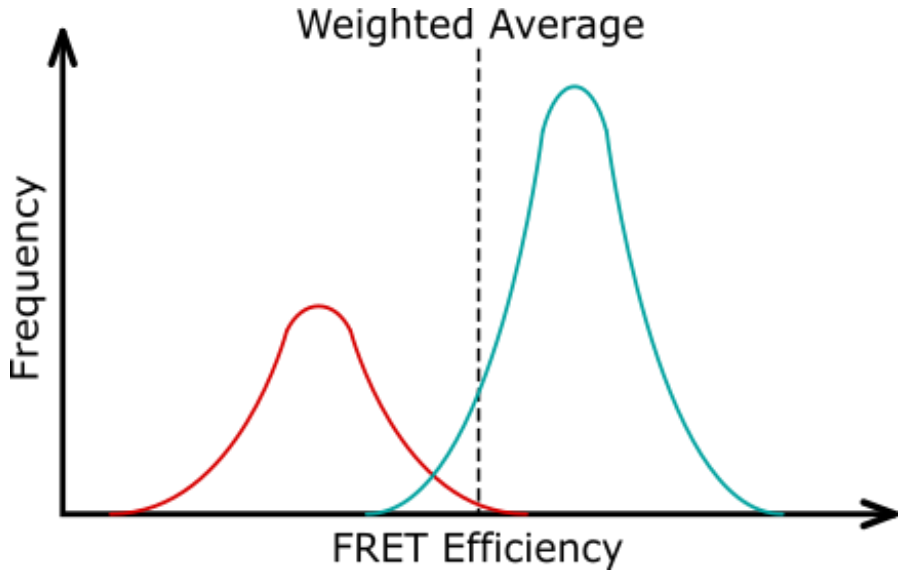

Figure 58. Weighted average of heterogenous population of molecules using ensemble FRET. *A hypothetical sample consisting of molecules within two distinct conformations. Illustrated is how the weighted average of such a sample does not properly describe the heterogeneity present.*

1.10.3.1 Surface-immobilised smFRET

smFRET can be performed using a TIRF microscope setup by immobilising fluorescently labelled molecules to the coverslip surface. By confining molecules within the TIRF illumination volume, many molecules can be monitored in parallel. This reduces the observation time needed to gain a statistically significant population of FRET measurements. A sufficiently high temporal resolution also allows individual conformational changes to be observed in real-time. This has been used to elucidate the pathways which molecules take to change their conformations. The primary disadvantages of this technique stem from the manipulation of biomolecules to facilitate surface immobilisation. This can include incorrect molecular function due to hinderance of the molecule at the coverslip or complete loss of molecular function due to the presence of the immobilising factor.

1.10.3.2 Solution-based smFRET

FRET-labelled molecules can also be detected when freely diffusing within solution using a confocal setup. A small illumination volume is created within the sample by focussing an excitation laser to a diffraction-limited volume. This increases the likelihood that only a single molecule is detected at any given time. When a molecule enters the illumination volume, it releases multiple photons as it fluoresces which is termed a photon burst. These bursts are detected using single-photon avalanche diode (SPAD) detectors. SPAD detectors produce a pulse every time a photon is detected and so are not limited by frame rates like CCD and CMOS detectors. By measuring the FRET efficiency of molecules within solution, the behaviour of biomolecules is uninhibited. However, this does come at the cost of a lower throughput of FRET measurements. This means that for a statistically significant number of FRET measurements to be taken, longer acquisitions are required. The short-lived retention time of molecules within the confocal detection volume also disallows for real-time monitoring of a single molecule's conformation.